Quantum Metrology with a Scanning Probe Atom Interferometer

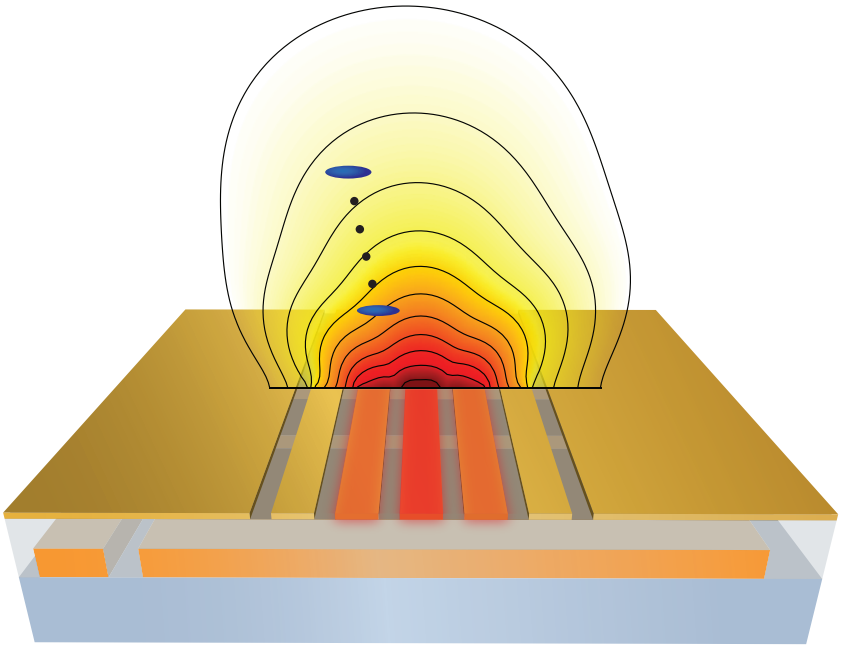

Caspar Ockeloen

Quantum Metrology with a Scanning Probe Atom Interferometer

Inauguraldissertation

zur
Erlangung der Würde eines Doktors der Philosophie
vorgelegt der
Philosophisch-Naturwissenschaftlichen Fakultät
der Universität Basel

von

Caspar Ockeloen
aus den Niederlanden

Basel, 2014

Genehmigt von der Philosophisch-Naturwissenschaftlichen Fakultät
auf Antrag von
Prof. Dr. P. Treutlein
Prof. Dr. M. Oberthaler

Basel, den 20. Mai 2014

Prof. Dr. Jörg Schibler
Dekan

Abstract

Atom interferometers provide record precision in measurements of a broad range of physical quantities. Extending atom interferometry to micrometer spatial resolution would enable new applications in electromagnetic field sensing, surface science, and the search for fundamental short-range interactions. I present experiments where we use a small Bose-Einstein condensate on an atom chip as an interferometric scanning probe to map out a microwave field at distances down to 16 micrometer from the chip surface with a few micrometers spatial resolution. By creating entanglement between the atoms, our interferometer overcomes the standard quantum limit of interferometry by 4 dB in variance and maintains enhanced performance for interrogation times up to 10 ms. This corresponds to a microwave magnetic field sensitivity of $77\,\mathrm{pT}/\sqrt{\mathrm{Hz}}$ in a probe volume of $20\,\mu\mathrm{m}^3$. High-resolution measurements of microwave near-fields, as demonstrated here, are important for the development of integrated microwave circuits for quantum information processing and applications in communication technology.

Quantum metrology with entangled atoms is particularly useful in measurements with high spatial resolution, since the atom number in the probe volume is limited by collisional losses. I analyze the effect of such density-dependent losses in high-resolution atom interferometry, and show that there is a strict upper limit on the useful number of atoms. Our experimental results indicate that even tighter limits on the particle number and interrogation time may arise from density-dependent dephasing, and provide a starting point for future studies towards the fundamental limits of coherence in Bose-Einstein condensates. Our experimental setup is ideally suited to experimentally address these questions, and provides a promising platform for further studies on quantum metrology and entanglement in many-particle atomic systems.

Contents

1

Introduction

Interferometry is the cornerstone of most modern precision measurements. In interferometry, interference patterns that occur when superimposing waves are used to infer information about the path traveled by the waves. Atom interferometers make use of the wave-like nature of matter, which was first predicted by deBroglie [1]. Interferometers operating with large atomic ensembles allow for ultraprecise measurements of gravitation, inertial forces, fundamental constants, electromagnetic fields [2, 3], and in atomic clocks provide the definition of the second [4]. Atom interferometers typically operate with large atomic ensembles containing up to millions of atoms. However, using a small atomic cloud as a scanning-probe interferometer with high spatial resolution would enable new applications in electromagnetic field sensing, surface science, and the search for fundamental short-range interactions [2].

In an atom interferometer, the external (motional) or internal (spin) state of atoms is coherently split and allowed to follow two different pathways. During an interrogation time T_R, a phase difference between the paths is accumulated, which depends on the quantity to be measured. When the paths are recombined, the wave-character of the atoms gives rise to an interference pattern, from which the phase can be determined. To measure this interference, the number of atoms in each output state is counted. Here the particle-character of the atoms is revealed, as the measurement process randomly projects the wave function of each atom into a definite state. When operating with an ensemble of N uncorrelated (non-entangled) particles, the binomial counting statistics limit the phase uncertainty of the interferometer to $1/\sqrt{N}$, the standard quantum limit (SQL) of interferometric measurement [5].

It is possible to overcome the SQL by making use of entanglement between the atoms [6]. Using such quantum correlations, the measurement outcome of each atom can depend on that of the other atoms. If used in a clever way, the phase uncertainty of an interferometer can be reduced below the SQL, in principle down to the ultimate Heisenberg limit of $1/N$ [7]. The field of quantum metrology studies the use of entanglement for enhanced measurement precision [6]. In recent years, suitable quantum states for entanglement-enhanced interferometry with

atoms have been experimentally demonstrated [8–19]. Several demonstrations of complete interferometer sequences and entanglement-enhanced measurements have been reported [20–24], reaching an improved sensitivity by 4 dB in variance compared to the SQL and an interrogation time of $T_R = 600$ µs in reference [22].

In principle, quantum metrology can improve the precision of any interferometer, but creating and exploiting the required entanglement is often challenging in practice. Entanglement-enhanced interferometry is particularly useful in situations where N is limited by a physical process, such that the SQL cannot be improved by simply increasing N. One such scenario is when high spatial resolution is desired. The number of atoms in a small probe volume is fundamentally limited by density-dependent losses. The collision rate increases with density, and eventually any additional atoms are simply lost from the trap before the interferometer sequence has completed. This sets a tight limit on both the atom number and the maximum interrogation time. Additional fundamental limits to both N and T_R arise from dephasing effects.

Atom chips provide a good platform for atom interferometry with high spatial resolution. An atom chip is a micro-fabricated device with current-carrying wires or other structures that allow magnetic trapping and precise manipulation of neutral atoms close to the chip surface [25–27]. Atom chip traps are particularly suitable for small ensembles of ultra-cold atoms, either in a thermal state or condensed to a Bose-Einstein condensate (BEC). The trapping potential can be accurately manipulated by adjusting wire currents, external magnetic fields and other tools such as integrated microwave near-field potentials. This allows precise positioning of the atomic cloud close to the chip surface, ideal for realizing a scanning probe. So far, both non-interferometric scanning-probe measurements [28–33] and interferometric measurements with a static cloud [34–36] have been reported on atom chips, but up to now neither an interferometric scanning probe nor a measurement beyond the SQL has been demonstrated.

This thesis

In this thesis I present a scanning-probe atom interferometer with high spatial resolution that overcomes the SQL using entanglement. Our interferometer probe is a Bose-Einstein condensate (BEC) on an atom chip. We use it to measure a microwave near-field generated with an on-chip microwave guide. By measuring at several points in space we realize a scanning-probe interferometer.

We use $N = 1400$ Rubidium-87 atoms, trapped in a cloud of $1.1 \times 1.1 \times 4.0$ µm radius, 16 to 40 µm from the chip surface. Two internal states of the atoms are used as interferometric pathways, and the pathways are split and recombined using two-photon microwave and radio frequency pulses. At the end of the interferometer sequence, we count the atoms in each output state with sensitive absorption imaging, with a precision of about 5 atoms.

We create entanglement between the atoms by using a nonlinear interaction

naturally arising in our system due to collisions between the atoms [12]. When two atoms collide, both atoms obtain a phase shift depending on the state of the other atom, thus creating quantum correlations between the two. A key feature of our experiment is that we can turn on the nonlinear interaction by spatially separating the two states. After the desired entanglement is created we recombine the two states, effectively turning off the nonlinearity during the interrogation time of the interferometer.

With this interaction, we create spin-squeezed states and realize an entanglement-enhanced interferometer with a sensitivity of 4 dB in variance below to SQL, and sub-SQL sensitivity is maintained for a interrogation times up to $T_R = 10$ ms at a distance of 40 µm from the chip surface. Our scanning-probe interferometer operates on average 2.2 dB below the SQL down to 16 µm from the surface. This also shows that the entanglement between the atoms survives while they are transported close to the chip surface, which takes 20 ms of transport time. This is the first demonstration of entanglement-enhanced atom interferometry with a high spatial resolution scanning probe, and promises further high-resolution sensing and measurement applications. The results of this work have also been published in reference [37].

Outline

Chapter 2 gives a general introduction to ultracold atoms, and discusses their interaction with static and oscillating magnetic fields. These are our main tools for manipulating the internal and external state of the atoms. Chapter 3 discusses interferometry, the standard quantum limit and quantum metrology in general. In chapter 4, these concepts are applied to our experimental situation and I discuss how density-dependent losses limit the useful number of atoms in our small interferometric probe.

Chapter 5 discusses the experimental setup in detail, and in chapter 6 the results for our scanning-probe atom interferometer are presented. Finally, chapter 7 concludes the thesis, and gives an outlook on on-going work in our experiment.

2

Ultracold atoms and electromagnetic fields

In this chapter, I give an overview of some concepts that are used in the remainder of this thesis. I start by introducing ultracold atoms and Bose-Einstein condensation. With a focus on ^{87}Rb, which is the atomic species used in this thesis, I describe the interaction of a ground-state atom with static and oscillating magnetic fields in section 2.3. We use this interaction to manipulate both the motion and internal state of the atom. The internal state can be effectively described as a collective spin, defined in section 2.4. Finally, I introduce atom chips and basic trapping potentials in section 2.5.

2.1 Ultracold atoms

Spectroscopy on atomic gases has played an important role in understanding physics at the atomic and molecular scale, and is the basis for many precision measurements [3]. One of the most influential applications of atomic spectroscopy is the atomic clock. Invented in the 1950s, atomic clocks enabled a precise redefinition of the second based on interferometric spectroscopy of a hyperfine transition in Caesium [38].

The advent of laser cooling and trapping enabled a large improvement in atomic precision measurements [39,40]. Using the momentum of light to slow, cool and trap atoms reduced the atomic sample temperature from room temperature or far above to the μK regime; optical and magnetic trapping potentials allowed to study the cold samples for longer time. Further reduction of temperature has been achieved by advanced laser cooling techniques and using forced evaporative cooling [41]. The combination of laser cooling, magnetic trapping and evaporative cooling of atoms has led to the first realizations of Bose-Einstein condensation, a new quantum state of matter [42–44].

Alkali atoms, having only a single valence electron, exhibit a relatively simple internal level structure and are therefore popular choices for laser cooling as well as spectroscopy and atomic clocks. Rubidium-87, used in this thesis, has optical

transitions in the near infrared for which suitable laser sources have already long been widely available[1], and which has been used in many ultracold-atom experiments.

2.2 Bose-Einstein condensation

Bose-Einstein condensation (BEC) is a peculiar state of matter first predicted by Bose and Einstein in 1925 [45]. BEC is a purely quantum-statistical phenomenon, characterized by macroscopic population of the ground state when Bosonic particles are cooled to very low temperature [46]. At such temperatures, the number of energetically available quantum states is comparable to the number of particles, and the details of the quantum statistics become significant. Given suitable dimensionality and geometry of the system, below a transition temperature T_c the (phase) transition to BEC occurs and most particles *condense* into the ground state, forming a Bose-Einstein condensate (a BEC).

Since the first experimental demonstrations of BEC in 1995 [42–44], their properties have been studied extensively in both theory and experiments. In this thesis, the phenomenon of BEC is not itself studied in detail, but rather used as a tool for quantum technology. Since in a BEC most atoms occupy the exact same quantum state, it is an extremely "clean" starting point for further manipulation of the quantum state of the system, and as such a promising platform for quantum metrology and other quantum technologies[2].

For detailed theoretical discussion of the phenomena many good references are available, e.g. [47, 48]. Here, I only mention a few key results that are of use later in this thesis and give an intuitive description of BEC following reference [48].

Intuitively, BEC can be understood from the statistical problem of distributing N bosons over p quantum states. For example, consider the case $N = p$. If the particles are *distinguishable*, as would be the case for classical particles, there are $N!$ different configurations with exactly one particle in each state, but only p configurations where all particles are in the same state. Even for small N, it is extremely unlikely to find large occupation of any state. However, for *indistinguishable* particles, such as identical Bosons in quantum mechanics, there is only 1 configuration with one particle per state, and still p configurations where all particles are in the same state. Thus, it becomes more likely to find a significant number of particles occupying the same quantum state.

It is important to note that this effect of distinguishability only plays a significant role if the number of states p is limited. For large $p \gg N$, the majority of states is unoccupied in any case, and the statistics are not affected by whether

[1] In particular, the original compact disc used diode lasers at 780 nm, corresponding to the D_2 line in ^{87}Rb, which led to mass production of lasers at this wavelength.

[2] Note that BEC is by no means necessary for quantum metrology with atoms. Many of the techniques described in this thesis may well apply to thermal trapped atoms, and quantum metrology is even possible with room-temperature atomic vapor [23].

or not the particles are distinguishable. The quantum effects become significant when $p \lesssim N$, in which case the gas is called *degenerate*. In practice this condition is reached by lowering the temperature T, which limits the accessible number of states. Whether or not a BEC can form at finite temperature depends strongly on the density of states, or how the states are distributed in energy. This is, in turn, determined by the dimensionality of the system and the trapping potential. In particular, for a three-dimensional non-interacting gas in a harmonic trap with large N, a BEC is formed below the transition temperature T_c defined by [48]

$$k_B T_c = 0.94\, \hbar\overline{\omega_t}\, N^{1/3}, \tag{2.1}$$

where $\overline{\omega_t}$ is the geometric mean of the trap frequencies and large N is assumed. For $T < T_c$, the ground state is macroscopically occupied by N_c atoms, given by

$$\frac{N_c}{N} = 1 - \left(\frac{T}{T_c}\right)^3. \tag{2.2}$$

For smaller N, small corrections to these equations can be made [46].

Although BEC can be formed by non-interacting atoms, in general interactions (elastic collisions) between the particles play an important role in defining the properties of the condensate. Weakly repulsive interactions, as we have for our ^{87}Rb atoms, actually tend to reinforce the effect of statistics in forming BEC [48]. Typically, the interactions can be well described by only considering spherically symmetric s-wave collisions[3], characterized by the s-wave scattering length a.

2.2.1 Mean-field description

The collective dynamics of a BEC are well described by the Gross-Pitaevskii (GP) or mean-field approximation, which is obtained by assuming that the many-body wave function is a product of single-particle wave functions and neglecting any excitations (T=0). For a single-component BEC, the time-dependent GP equation reads [48]

$$i\hbar\frac{\partial\Psi}{\partial t} = -\frac{\hbar^2}{2m}\nabla^2\Psi + V\Psi + g|\Psi|^2\Psi. \tag{2.3}$$

Here, $\Psi(\vec{r},t) = \sqrt{N}\psi(\vec{r},t)$ is the condensate order parameter with ψ the single-particle wave function. The terms on the right-hand side of equation (2.3) correspond to the kinetic energy, the trapping potential V, and interactions characterized by the effective interaction constant $g = 4\pi\hbar^2 a/m$, where m is the atomic mass. The complex problem of pairwise interactions is greatly simplified in the GP equation: for any particle, the effect of all other particles takes the form of

[3] For alkali atoms, the temperatures relevant to BEC are typically much smaller than the energy scale associated with the interatomic (van der Waals) potentials. This makes higher partial wave scattering processes energetically unlikely [48].

an extra potential energy that scales with the local density $|\Psi|^2$. This is often called the *mean-field* interaction.

The ground-state density profile can be found from the time-independent version of the GP equation, where the time derivative $i\hbar\partial/\partial t$ is replaced by the chemical potential μ. For large condensates, the kinetic energy can usually be neglected compared to the interactions, leading to a density profile that mimics the trapping potential. This is the famous Thomas-Fermi limit. In a harmonic trap, the Thomas-Fermi profile is an inverted parabola with radius $R_{\mathrm{TF},i} = \sqrt{2\mu/(m\omega_i^2)}$, with ω_i the trap frequency in direction $i \in \{x, y, z\}$ [47]. For small and/or strongly elongated BECs the kinetic energy becomes relevant. We use the approximations in reference [49] to find a modified R_{TF} describing the size of our cloud.

When the particles are allowed to occupy two internal states, equation (2.3) can be extended to a set of two coupled equations. The two-component GP equations read [48, 50]

$$i\hbar\frac{\partial\Psi_i}{\partial t} = -\frac{\hbar^2}{2m}\nabla^2\Psi_i + V_i\Psi_i + g_{ii}|\Psi_i|^2\Psi_i + g_{ij}|\Psi_j|^2\Psi_i, \tag{2.4}$$

for $i, j \in \{1, 2\}$, $j \neq i$, and where Ψ_i represents the order parameter of component i and $g_{ij} = 4\pi\hbar^2 a_{ij}/m$ characterizes the s-wave scattering interactions between components i and j. Interactions changing the internal state are excluded. In general, the intra-state interaction parameters a_{11}, a_{22} are different from each other and from the inter-state interactions $a_{12} = a_{21}$.

2.3 Atom-field interaction

The techniques used in this thesis rely on manipulating and interrogating neutral ^{87}Rb atoms with various electromagnetic fields, and a basic understanding of the corresponding atom-field interaction is required. Fortunately, this interaction has been studied in great detail, and it suffices here to briefly mention a few results that are needed later in this work.

For laser cooling, optical pumping and atom detection, we use near-infrared lasers to excite the electric dipole transition between the $5S_{1/2}$ ground state and $5P_{3/2}$ excited state (the D_2 line). A detailed treatment of these techniques can be found in reference [39].

Within the $5S_{1/2}$ hyperfine manifold, we use microwave and radio frequency fields to couple various levels. These transitions are only sensitive to the magnetic component of the field, and thus we consider only the magnetic microwave field in this thesis[4]. For a thorough analysis of this interaction in the context of our experiment the reader is referred to [51].

[4] The effect of the electric microwave field is common to all $|F, m_F\rangle$ states and in addition typically small compared to that of the magnetic field [51].

2.3.1 Hyperfine structure and static magnetic fields

An atom in a static magnetic field $\vec{B}$ is described by the Breit-Rabi Hamiltonian

$$H_{\mathrm{BR}} = A_{\mathrm{hfs}}\hat{I}\cdot\hat{J} + \mu_B(g_I\hat{I} + g_J\hat{J})\cdot\vec{B}. \tag{2.5}$$

Here A_{hfs} is the magnetic dipole constant of the manifold, $\hat{I}$ and $\hat{J}$ are the nuclear and electronic spin of the atom, respectively, and g_I and g_J the corresponding g-factors.

For $B = 0$, the eigenstates of H_{BR} are the eigenstates $|F, m_F\rangle$ of $\hat{F}^2$ and $\hat{F}_z$, where $\hat{F} = \hat{I} + \hat{J}$ is the total spin of the atom. For the ^{87}Rb ground state, $I = 3/2$ and $J = 1/2$, and there are two manifolds $|1, m_1\rangle$ and $|2, m_2\rangle$ separated in energy by $\Delta E_{\mathrm{hfs}} = 2A_{\mathrm{hfs}} = h \times 6.834682611$ GHz [52] and consisting of 3 and 5 degenerate m_F states, respectively.

For $J = 1/2$, the Breit-Rabi Hamiltonian can be diagonalized analytically for arbitrary magnetic field [52, 53]. In the $|F, m_F\rangle$ basis[5] for $I = 3/2$,

$$E_{|F,m_F\rangle} = -\frac{A_{\mathrm{hfs}}}{4} + g_I\mu_B m_F B \pm A_{\mathrm{hfs}}\sqrt{1 + m_F x + x^2}, \tag{2.6}$$

where $x = 2(g_J - g_I)\mu_B B/A_{\mathrm{hfs}}$ and the $+$ and $-$ signs refer to $F = 2$ and $F = 1$, respectively. For ^{87}Rb $g_J \approx 2$ and $g_I \approx -1 \times 10^{-3}$ [52], and in the following we neglect the coupling to the nuclear spin.

From equation (2.6), two magnetic-field regimes can be identified with a crossover around $B = A_{\mathrm{hfs}}/2(g_J - g_I)\mu_B = 610$ G. In low fields, the Breit-Rabi energy simplifies to the linear Zeeman effect, which gives a linear energy shift within each F-manifold,

$$E_Z \approx g_F m_F \mu_B B \tag{2.7}$$

where the total-angular-momentum g-factor $g_F \approx \pm\frac{1}{2}$, with the same sign convention as equation (2.6). This corresponds to a linear Zeeman shift of 0.70 MHz/G between adjacent m_F levels. Figure 2.1 shows the level diagram in this regime. There are three states that have increasing energy with increasing magnetic field, $|2, 2\rangle$, $|2, 1\rangle$ and $|1, -1\rangle$, which makes it possible to trap these states in a minimum of the magnetic field. The latter two states are particularly interesting for interferometry, as they have the same linear Zeeman shift. These two states will serve as the *interferometer states*, and I define the short-hand notation

$$\begin{aligned} |1\rangle &\equiv |F = 1, m_F = -1\rangle, \\ |2\rangle &\equiv |F = 2, m_F = 1\rangle. \end{aligned} \tag{2.8}$$

For most of our purposes, the linear Zeeman shift gives sufficiently accurate predictions. One important exception is the differential energy ΔE between $|1\rangle$

[5] It should be noted that for high fields the states $|F, m_F\rangle$ are not the eigenstates of $\hat{F}^2$ and $\hat{F}_z$. In this work we operate at low fields, where the distinction is negligible.

and $|2\rangle$, to which an interferometric measurement is sensitive and for which the quadratic Zeeman effect cannot be neglected. A useful property of this pair of states is that there is a "magic field" value $B_0 \approx 3.23$ G, around which the differential energy shift of the states $|1\rangle$ and $|2\rangle$ scales only quadratically with B,

$$\Delta E/\hbar = \omega_0 + \beta(B - B_0)^2, \tag{2.9}$$

with a curvature $\beta = 2\pi \times 431$ Hz/G^2 and offset $\omega_0 = 2\pi \times 6.834678114$ GHz [54]. Operating close to the magic field makes a superposition between $|1\rangle$ and $|2\rangle$ very robust to magnetic field noise, and coherence times up to seconds [34] and even one minute [55] have been measured.

2.3.2 Microwave and radio frequency fields

As seen in the previous section, there are two relevant energy scales within the ground state hyperfine manifold of ^{87}Rb. At low magnetic fields of a few Gauss, the states are grouped in the $F = 1$ and the $F = 2$ manifolds, separated by $E_{\text{hfs}} \approx h \times 6.8$ GHz. Within each F-manifold, adjacent m_F levels are separated by a few MHz in frequency. Magnetic dipole transitions can be driven both between $F = 1$ and $F = 2$ (with the selection rule $\Delta m_F = 0, \pm 1$) and between adjacent m_F levels. For clarity, in this thesis we refer to ≈ 6.8 GHz-fields as *microwave frequency* (MW) and reserve the term *radio frequency* (RF) for fields oscillating at MHz frequencies[6].

2.3.3 Microwave potentials

A complete description of the atom in a radiation field can be given in the dressed-state picture by considering the atom (with Hamiltonian H_{BR} given in (2.5)) coupled to the quantized radiation field, which is discussed in detail for ^{87}Rb in reference [51]. For strong microwave fields, however, the situation can be greatly simplified and reference to the quantized field can be dropped altogether from the problem. Here, I present some results following section 5.1 of reference [51].

In the dressed-state picture, the atom-field system has eigenstates characterized by the atomic state $|F, m_F\rangle$ and the field state $|n\rangle$ occupied by n photons in a single field mode at frequency ω. By considering only one field mode, the driving field is approximated as monochromatic radiation. In small static field B, such that $\mu_B B \ll E_{\text{hfs}}$, and at the same time small microwave detuning $\Delta_0 = \omega - \omega_0 \ll \omega_0$, the atom-field states form a "ladder" of well-separated groups, where each step in the ladder consists of the 8 closely-spaced states $|1, m_F\rangle|n+1\rangle$ and $|2, m_F\rangle|n\rangle$ and the separation between steps is $\hbar\omega$. If furthermore the microwave field strength $\mu_B B_{\text{mw}}$ is small compared to the hyperfine splitting, couplings only occur within each group. We can make the rotating

[6] Note that in industry applications, the term RF usually includes the full microwave spectrum, but in this thesis it refers only to frequencies from ≈ 1 MHz up to a few tens of MHz.

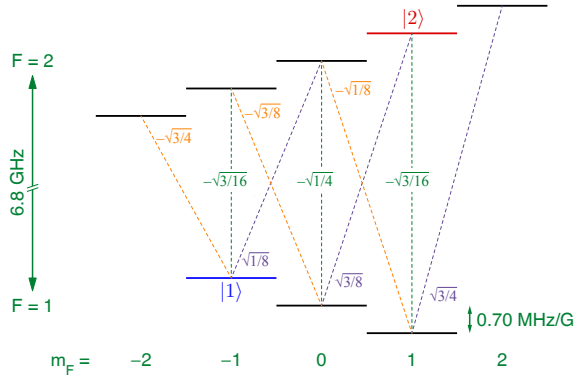

Figure 2.1: Level diagram of the hyperfine ground state manifold at small fields. Horizontal lines indicate the levels, with interferometer states $|1\rangle$ and $|2\rangle$ highlighted in blue and red, respectively. Dashed lines indicate possible microwave transitions for σ^- (orange), π (green) and σ^+ (purple) labeled by corresponding matrix elements $\langle 2, m_2|J_\alpha|1, m_1\rangle$, for $\alpha = -, z, +$, respectively, where $J_\pm = J_x \pm iJ_y$.

wave approximation by taking only one such group into consideration, leaving only 8 states like we had for the bare atom.

If in addition $n \gg 1$, we can ignore the difference between $|n\rangle$ and $|n+1\rangle$. This makes the problem independent of the field quantization, and we can drop the quantized field in favor of the classical field

$$\vec{B}_{\mathrm{mw}}(t) = B_{\mathrm{mw}} \frac{1}{2} \left(\vec{\epsilon} e^{-i\omega t} + \vec{\epsilon}^{*} e^{i\omega t} \right)$$

with amplitude B_{mw} and unit polarization vector $\vec{\epsilon}$. The calculation no longer depends on which value of $|n\rangle$ we chose to keep. Note that, by dropping reference to the field state, we lose track of the energy difference $\hbar\omega$ between the $|1, m_F\rangle|n+1\rangle$ and $|2, m_F\rangle|n\rangle$ groups. This is equivalent to transforming to the reference frame co-rotating at ω, as is usually done when the field is treated classically from the start (see e.g. [39]).

Finally, we simplify H_{BR} to include only the linear Zeeman shift as discussed in section 2.3.1. The resulting Hamiltonian in the $|F, m_F\rangle$ basis is

$$\begin{aligned} H = &\sum_{m_2} \left(-\frac{1}{2}\hbar\Delta_0 + g_2 \mu_B m_2 B \right) |2, m_2\rangle\langle 2, m_2| \\ &+ \sum_{m_1} \left(+\frac{1}{2}\hbar\Delta_0 + g_1 \mu_B m_1 B \right) |1, m_1\rangle\langle 1, m_1| \\ &+ \sum_{m_1, m_2} \left(\frac{1}{2}\hbar\Omega_{1,m_1}^{2,m_2} |2, m_2\rangle\langle 1, m_2| + h.c. \right). \end{aligned} \tag{2.10}$$

On the diagonal, we have the (linear) Zeeman energies, frequency-shifted by $\pm\Delta_0/2$ which is the hyperfine splitting in the frame co-rotating at ω. Off-diagonal,

we have the coupling elements characterized by the Rabi frequencies

$$\Omega_{1,m_1}^{2,m_2} = \mu_B B_{\mathrm{mw}} \langle 2, m_2 | \vec{\epsilon} \cdot \vec{J} | 1, m_1 \rangle. \tag{2.11}$$

These couplings can be separated into linearly polarized π transitions sensitive to $\vec{\epsilon} \cdot \vec{e}_z$ and $\Delta m_F = 0$, and circular polarized $\sigma^{\pm}$ transitions sensitive to $\vec{\epsilon} \cdot (\vec{e}_x \pm i\vec{e}_y)/\sqrt{2}$. The corresponding matrix elements $\langle 2, m_2 | \vec{\epsilon} \cdot \vec{J} | 1, m_1 \rangle$ are calculated in appendix A.3 of reference [51], and summarized in figure 2.1, where we define $J_{\pm} = J_x \pm i J_y$.

The eigenstates of equation (2.10) can be written as superpositions of $|F, m_F\rangle$ states. Far detuned from any possible transition, that is when $|\Omega_{1,m_1}^{2,m_2}| \ll |\Delta_{1,m_1}^{2,m_2}|$ for all combinations of m_1, m_2 where Δ_{1,m_1}^{2,m_2} is the detuning to the respective transition, the eigenstates are very close to the bare $|F, m_F\rangle$ states and their energies are well described by summing the AC Zeeman shift contributions from each off-resonant transition

$$E_{|F,m_F\rangle} \approx E_Z \mp \frac{1}{2}\hbar\Delta_0 \mp \hbar \sum \frac{|\Omega_{1,m_1}^{2,m_2}|^2}{4\Delta_{1,m_1}^{2,m_2}}, \tag{2.12}$$

where the sum runs over all levels coupled to $|F, m_F\rangle$ and the minus (plus) sign corresponds to $F = 2$ ($F = 1$).

Combined with spatial gradients of the microwave field intensity, this AC Zeeman shift can be used to make a spatially structured potential for the atoms. Interestingly, this potential is state-selective, and the state-selectivity can be chosen by adjusting the microwave frequency.

Early work in microwave trapping of neutral atoms has been done in the standing wave of a cavity field [56], but large field gradients are difficult to achieve due to the large microwave wavelength. In contrast, the near-field distribution close to small microwave guiding structures can be used to generate strong gradients [57]. In this thesis, we use such near-field gradients to generate state-dependent potentials (see section 5.5).

2.3.4 Rabi oscillations

Before considering resonant Rabi coupling in the full 8-level system, it is useful to consider the simple scenario of Rabi coupling in 2-level and 3-level systems.

Two-level system

Consider a two-level atom with energy eigenstates $|1\rangle$ and $|2\rangle$ separated in energy by $\hbar\omega_0$. The levels are coupled by an oscillating field at frequency ω, detuned from resonance by $\delta = \omega - \omega_0$.

Close to resonance ($|\delta|, |\Omega| \ll \omega_0$) we can again make the rotating wave approximation. The Hamiltonian in the frame co-rotating at ω is [39, 58]

$$H = \frac{\hbar}{2} \begin{pmatrix} \delta & \Omega^* \\ \Omega & -\delta \end{pmatrix} \tag{2.13}$$

in the basis $\{|1\rangle, |2\rangle\}$. Here, the Rabi frequency Ω is in general complex. The complex phase of Ω corresponds to the phase of the driving field with respect to the co-rotating frame[7].

Writing a general two-level state $|\psi\rangle = c_1|1\rangle + c_2|2\rangle$, the solution to the Schrödinger equation is [58]

$$\begin{aligned} c_1(t) &= c_1(0)\left[\cos\left(\frac{\Omega' t}{2}\right) - \frac{i\delta}{\Omega'}\sin\left(\frac{\Omega' t}{2}\right)\right] - i\frac{\Omega^*}{\Omega'}c_2(0)\sin\left(\frac{\Omega' t}{2}\right) \\ c_2(t) &= c_2(0)\left[\cos\left(\frac{\Omega' t}{2}\right) + \frac{i\delta}{\Omega'}\sin\left(\frac{\Omega' t}{2}\right)\right] - i\frac{\Omega}{\Omega'}c_1(0)\sin\left(\frac{\Omega' t}{2}\right), \end{aligned} \tag{2.14}$$

where $\Omega' = \sqrt{|\Omega|^2 + \delta^2}$ is the *generalized Rabi frequency*. Starting from an initial state $|1\rangle$, the population oscillates with frequency Ω'. On resonance, the oscillation frequency is minimal and the populations oscillate fully between $|1\rangle$ and $|2\rangle$. For $\delta \neq 0$, Ω' increases and the oscillation amplitude is reduced, such that state $|2\rangle$ is never fully reached. In our experiment, we use the hyperbolic form of Ω' as a function of δ to find the resonance condition $\delta = 0$.

Two-photon transitions in a three-level system

Next, we consider a three-level system with levels $\{|1\rangle, |2\rangle, |3\rangle\}$, where $|3\rangle$ is denoted the *intermediate state*. It may lie in energy between $|1\rangle$ and $|2\rangle$ ("ladder system") or outside that interval ("Λ" or "V" system). Here we choose the signs corresponding to a Λ system[8]. We denote the energy difference between $|i\rangle$ and $|j\rangle$ as $\hbar\omega_{ij}$.

Two coupling fields are introduced, with frequencies ω_1 and ω_2 and coupling strengths Ω_1 and Ω_2, respectively. Here, Ω_i is the single-photon Rabi frequency for coupling between state $|i\rangle$ and $|3\rangle$, and we assume there is no direct coupling between $|1\rangle$ and $|2\rangle$. We define the *intermediate-state detuning* Δ and the *two-photon detuning* δ such that

$$\begin{aligned} \omega_1 &= \omega_{13} + \Delta + \delta/2, \\ \omega_2 &= \omega_{23} + \Delta - \delta/2. \end{aligned}$$

Consequently, for $\delta = 0$ the frequency difference between the two light fields corresponds exactly to the frequency difference ω_{12} between $|1\rangle$ and $|2\rangle$.

[7] It is useful to define the phase of the co-rotating frame as a fixed phase reference for an entire experiment. Complex sequences of Rabi pulses can then be described by repeatedly evolving the system under Hamiltonian (2.13). Each pulse can be phase-shifted, and phase of Ω keeps track of these phase shifts.

[8] In a Λ system, we can choose both fields with similar frequency and the rotating frame is more clearly visualized than in a ladders system.

The Hamiltonian after making the RWA in the co-rotating frame at $(\omega_1+\omega_2)/2$ is [58]

$$H = \frac{\hbar}{2}\begin{pmatrix} \delta & 0 & \Omega_1^* \\ 0 & -\delta & \Omega_2^* \\ \Omega_1 & \Omega_2 & -2\Delta \end{pmatrix}. \tag{2.15}$$

If the intermediate-state detuning is large enough, $|\Delta| \gg |\Omega_1|, |\Omega_2|, |\delta|$, both coupling fields are off-resonant and significant population of $|3\rangle$ does not occur. However, a coherent *two-photon transition* between $|1\rangle$ and $|2\rangle$ is possible, if δ is chosen to ensure two-photon resonance (which will be defined below). This is a useful technique when selection rules do not allow a direct transition between $|1\rangle$ and $|2\rangle$, as is the case in our experiment, or when sources at the direct transition frequency are not conveniently available.

Under these conditions, the two-photon transition behaves similar to a single-photon Rabi transition, which can be demonstrated by adiabatic elimination of the intermediate state. Although $|c_3|^2 \approx 0$, it has small-amplitude oscillations at frequency Δ. On the other hand, we might make the ansatz that $c_1(t)$ and $c_2(t)$ oscillate at much slower frequency. An approximate solution for $c_3(t)$ can then be found by direct integration, assuming $dc_1/dt = dc_2/dt = 0$ [59]. Substituting this solution into the Schrödinger equation leads to a system of two equations, equal to a two-level Schrödinger equation with effective Hamiltonian [58, 59]

$$H_{\text{eff}} = \frac{\hbar}{2}\begin{pmatrix} \frac{|\Omega_1|^2}{2\Delta} + \delta & \frac{\Omega_1\Omega_2^*}{2\Delta} \\ \frac{\Omega_1^*\Omega_2}{2\Delta} & \frac{|\Omega_2|^2}{2\Delta} - \delta \end{pmatrix} \tag{2.16}$$

Comparison with equation (2.13) shows that this is, up to a global shift, equivalent to a two-level system with effective Rabi frequency and detuning [58]

$$\begin{aligned} \Omega_{\text{eff}} &= \frac{\Omega_1\Omega_2}{2\Delta}, \\ \delta_{\text{eff}} &= \delta + \frac{|\Omega_1|^2 - |\Omega_2|^2}{4\Delta}. \end{aligned} \tag{2.17}$$

The two-photon resonance does not occur in general at $\delta = 0$, but at a shifted frequency $\delta_{\text{eff}} = 0$ due to the AC Zeeman shift due to the individual fields. On two-photon resonance, the populations $|c_1|^2$ and $|c_2|^2$ oscillate at frequency $|\Omega_{\text{eff}}| \ll |\Delta|$, showing that the solution indeed satisfies our ansatz, at least for $\delta_{\text{eff}} \ll |\Delta|$. Note that the complex phase of Ω_{eff} equals the total phase of the two driving fields, again with respect to the co-rotating frame.

Multilevel system

Similar to the three-level system discussed above, two-photon transitions can be used in multi-level systems. Provided that all detunings and coupling strengths are chosen such that no single-photon resonances occur and only one two-photon

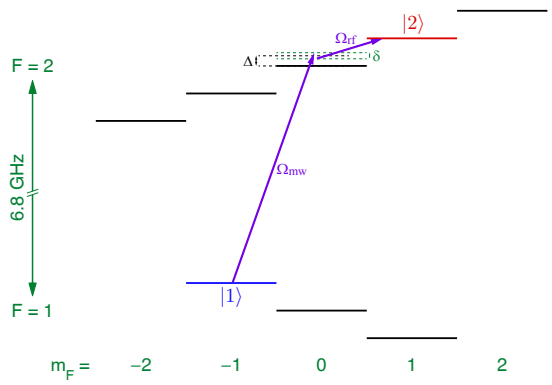

Figure 2.2: Two-photon transition. The figure shows the MW and RF couplings with Rabi frequencies Ω_{mw} and Ω_{rf}, respectively, and the definitions of the intermediate-state detuning Δ and the two-photon detuning δ.

combination is close to resonance, the same process of adiabatic elimination can be used to eliminate all "unwanted" states and generate an effective two-level system.

In reference [58], this calculation is carried out for coupling the interferometer states $|1\rangle$ and $|2\rangle$ via the intermediate state $|2,0\rangle$ in the ^{87}Rb ground state. The corresponding level diagram is shown in figure 2.2. The coupling fields are a microwave field with Rabi frequency Ω_{mw} coupling $|1,-1\rangle$ to $|2,0\rangle$ and an RF field with Rabi frequency Ω_{rf} coupling $|2,0\rangle$ to $|2,1\rangle$. The intermediate-state detuning Δ is defined with respect to $|2,0\rangle$.

Assuming a linearly polarized RF field, the full 8-level system can approximated as an effective two-level system with effective Rabi frequency and detuning given by [58]

$$\begin{aligned} \Omega_{\mathrm{eff}} &\approx \frac{\Omega_{\mathrm{mw}}\Omega_{\mathrm{rf}}}{2\Delta} \\ \delta_{\mathrm{eff}} &\approx \delta + \frac{|\Omega_{\mathrm{mw}}|^2}{4\Delta}, \end{aligned} \tag{2.18}$$

where only the microwave level shift due to the $|1,-1\rangle \leftrightarrow |2,0\rangle$ transition is taken into account. The most important difference from the three-level system is that, at this level of approximation, the AC Zeeman shift is caused only by the microwave field. This is a special feature of our state pair: for linearly polarized RF and in the linear Zeeman regime, both states have equal level shifts. The microwave level shift predicted by equation 2.18 gives a good approximation for small detuning $\Delta \ll \Omega$. However, for larger detunings, all microwave transitions to either $|1,-1\rangle$ or $|2,0\rangle$ are significant, and the level shift depends strongly on the polarization of the microwave field. For example, in our experimental situation we use $\Delta = 2\pi \times 500$ kHz and $B_0 = 3.23$ G. In that case, a linearly polarized

microwave field perpendicular to the static magnetic field corresponds to an error of 22% compared to the microwave level shift predicted by equation 2.12.

2.4 Pseudo-spin description

The internal state of any two-level system can be conveniently described by associating it with a pseudo-spin-1/2 (or artificial spin-1/2). This allows the state to be described geometrically in a pseudo-spin space. For convenience, express all such spins in units of $\hbar$, such that we can write $\hbar = 1$ in the pseudo-spin space.

2.4.1 Two-level Bloch sphere

The state of a two-level system can be described by the two complex amplitudes c_1 and c_2, as was done in section 2.3.4. However, since the total population $|c_1|^2 + |c_2|^2 = 1$ for a valid quantum state, such a description is overdetermined. Furthermore, the absolute phase of c_1 and c_2 is of no physical interest, as only the relative phase can be measured in experiments. Therefore, it is useful to define a new set of parameters that describe the population difference and relative phase independently.

This goal is conveniently achieved by defining the *Bloch vector* $\vec{s}$ [60],

$$\begin{aligned} s_x &= \frac{1}{2}(c_1^* c_2 + c_1 c_2^*) = \frac{1}{2}\sin\vartheta\cos\phi, \\ s_y &= \frac{1}{2i}(c_1^* c_2 - c_1 c_2^*) = \frac{1}{2}\sin\vartheta\sin\phi, \\ s_z &= \frac{1}{2}(|c_2|^2 - |c_1|^2) = \frac{1}{2}\cos\vartheta. \end{aligned} \tag{2.19}$$

The Bloch vector uniquely describes any pure state of the two-level system. Since the length $||\vec{s}|| = 1/2$ is conserved, the vector can be graphically depicted as a point on a sphere of radius 1/2, as shown in figure 2.3. Similarly, it is well represented by spherical coordinates. The polar angle ϑ describes the population difference $2s_z = \cos\vartheta$, and the azimuthal angle ϕ gives the relative phase of the two states.

With the normalization chosen here as $||\vec{s}|| = 1/2$, the components of $\vec{s}$ are equal to the expectation values of the corresponding components of a spin-1/2 particle, and hence we sometimes refer to a two-level system as a *pseudo-spin-1/2* system. In this equivalence, $|1\rangle$ and $|2\rangle$ correspond to spin down and up eigenstates of the pseudo-spin-1/2.

Rabi oscillations (equation 2.14) are represented on the Bloch sphere as rotations around the *Rabi vector*

$$\vec{\Omega} = \begin{pmatrix} \mathrm{Re}(\Omega) \\ \mathrm{Im}(\Omega) \\ \delta \end{pmatrix}. \tag{2.20}$$

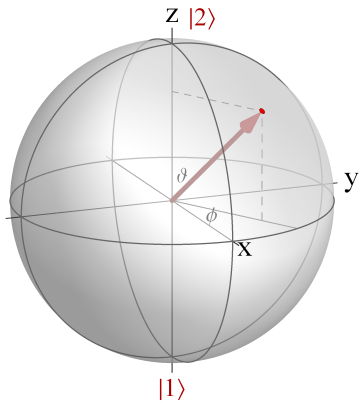

Figure 2.3: Bloch sphere. The state of a two-level system can be described by a vector of length 1/2 (red arrow). The projection on the z-axis describes the population difference $(|c_2|^2 - |c_1|^2)/2$ and the angle ϕ in the x, y-plane corresponds to the phase of the system.

The Schrödinger equation with Hamiltonian (2.13) can be written as

$$\frac{d\vec{s}}{dt} = \vec{\Omega} \times \vec{s}. \tag{2.21}$$

Resonantly driven Rabi oscillations correspond to rotations around a vector in the x, y-plane, and free evolution with a detuning δ corresponds to a rotation around the z-axis. Note that the Bloch vector is defined in the rotating frame (at ω), even if we set $|\Omega| = 0$.

2.4.2 Collective spin

To describe an ensemble of N (effective) two-level atoms, we define the *collective spin* $\vec{S} = \sum_{i=1}^{N} \vec{s}_i$, where $\vec{s}_i$ is the pseudo-spin-1/2 operator describing the internal state of atom i. The components of $\vec{S}$ are the spin operators $\hat{S}_x$, $\hat{S}_y$ and $\hat{S}_z$.

Like for the single-particle pseudo-spin $\vec{s}$, Rabi rotations and free evolution can be described by rotations around the Rabi vector $\vec{\Omega}$ (equation 2.20). A rotation by an angle α around the normalized direction $\vec{A} = \vec{\Omega}/||\vec{\Omega}||$ can be expressed as the unitary operation

$$|\psi_{\text{rot}}\rangle = e^{-i\alpha\vec{A}\cdot\vec{S}}|\psi\rangle. \tag{2.22}$$

A phase shift corresponds to a rotation around $\hat{S}_z$, whereas a Rabi pulse with phase ϕ corresponds to a rotation around $\hat{S}_{(\phi)} = \hat{S}_x \cos\phi + \hat{S}_y \sin\phi$.

The observables we measure in our experiment are the populations N_1 and N_2 of states $|1\rangle$ and $|2\rangle$, respectively. In the collective spin description, this is equivalent to measuring the eigenstates $|S, m\rangle$ of $\vec{S}^2$ and S_z, where the population difference $N_2 - N_1 = 2S_z$. To efficiently deal with fluctuating total N, we also define the relative population difference $n = 2S_z/N$.

2.4.3 Collisional interaction Hamiltonian

In the collective spin description, the collisional interactions present in the two-mode BEC (the last two terms in equation (2.4)) can be written as [50, 61, 62]

$$H = c + \nu_N \hat{S}_z + \chi \hat{S}_z^2, \tag{2.23}$$

which contains a constant offset c, an N-dependent phase rotation with rate ν_N, and a nonlinear interaction with rate χ. In this thesis, we generally ignore the first two terms of equation (2.23) (but the N-dependent phase shift is measured in the experiment, see section 6.9.1), and write the nonlinear interaction Hamiltonian

$$H_{\text{int}} = \chi \hat{S}_z^2, \tag{2.24}$$

which is also called the *one-axis twisting* Hamiltonian (see section 3.5). The rate χ is given by [62]

$$\chi = \frac{1}{2}\left(\frac{\partial \mu_1}{\partial N_1} + \frac{\partial \mu_2}{\partial N_2} - \frac{\partial \mu_1}{\partial N_2} - \frac{\partial \mu_2}{\partial N_1}\right), \tag{2.25}$$

with the chemical potentials of the two BEC components

$$\mu_i = \langle \psi_i | h_i | \psi_i \rangle + \sum_{j=1,2} g_{ij} N_j \int |\psi_i|^2 |\psi_j|^2 d^3\vec{r}, \tag{2.26}$$

where ψ_i is the mode function normalized to 1, and h_i is the single-particle Hamiltonian including kinetic and potential energy of component i. The derivatives in equation (2.25) are to be evaluated in the mean $\langle N_1 \rangle$ and $\langle N_2 \rangle$.

If the mode functions are independent of N, equation (2.25) simplifies to

$$\begin{aligned} \chi &= \frac{1}{2}u_{11} + \frac{1}{2}u_{22} - u_{12}, \\ u_{ij} &= g_{ij} \int |\psi_i|^2 |\psi_j|^2 d^3\vec{r}, \end{aligned} \tag{2.27}$$

where ψ_i is the mode function of component i normalized to 1.

The strength χ of this non-linear interaction depends both on the scattering lengths a_{ij} (through g_{ij}) and on the wave-function overlaps $\int |\psi_i|^2 |\psi_j|^2 d^3\vec{r}$. Modifying the relative scattering length a_{ij} is possible in some combinations of atomic species and states with a Feshbach resonance, which has been used to tune χ [20]. Alternatively, χ can be modified by changing the wave-function overlap, as is done in this work and previously in our experiment [12].

For our interferometer states $|1\rangle$ and $|2\rangle$, the scattering lengths are similar but not equal: $a_{11} = 100.40a_0$, $a_{12} = 98.01a_0$ and $a_{22} = 95.44a_0$, with a_0 the Bohr radius [63, 64]. Because the difference in scattering lengths is small, χ is usually very small for overlapping clouds. On the other hand, χ can be increased by three orders of magnitude by fully separated wave functions [60].

The rate ν_N of the N-dependent phase rotation can be written as [62]

$$\nu_N = (\mu_1 - \mu_2) - 2\chi\langle\hat{S}_z\rangle + \tilde{\chi}(\hat{N} - \langle N\rangle), \tag{2.28}$$

where $\hat{N}$ is the total particle number operator, and

$$\tilde{\chi} = \frac{1}{2}\left(\frac{\partial\mu_1}{\partial N_1} - \frac{\partial\mu_2}{\partial N_2}\right). \tag{2.29}$$

2.4.4 Wigner function

Actual experiments are not well described by pure states. A general mixed state is described by the density matrix

$$\hat{\rho} = \sum_i a_i|\psi_i\rangle\langle\psi_i|, \tag{2.30}$$

where a_i are the statistical weights of pure state $|\psi_i\rangle$ in the mixture. The density matrix provides a full description of the system, but is not easy to visualize for many-particle systems.

Alternative to the density matrix, we describe the state through the spherical Wigner function [65, 66]. It is a phase-space distribution on a sphere of radius S, which we call the *generalized Bloch sphere*. In terms of the spherical harmonics Y_{kq}, the Wigner function is

$$W(\vartheta,\phi) = \sum_{k=0}^{2S}\sum_{q=-k}^{k}\rho_{kq}Y_{kq}(\vartheta,\phi), \tag{2.31}$$

where ϑ and ϕ are the polar and azimuthal angles on the generalized Bloch sphere, respectively, and the weights ρ_{kq} are related to the density matrix elements $\rho_{mm'} = \langle S,m|\hat{\rho}|S,m'\rangle$ in the $|S,m\rangle$-basis as

$$\rho_{kq} = \sum_{m=-S}^{S}\sum_{m'=-S}^{S} t_{kq}^{Smm'}\rho_{mm'}, \tag{2.32}$$

with the transformation coefficients

$$t_{kq}^{Smm'} = (-1)^{S-m}\sqrt{2k+1}\begin{pmatrix} S & k & S \\ -m & q & m' \end{pmatrix} \tag{2.33}$$

where the last term in parentheses is the Wigner $3j$ symbol.

The spherical Wigner function is similar to the traditional Wigner function defined on the planar phase space of a harmonic oscillator. $W(\vartheta,\phi)$ can be seen as a quasi-probability distribution, and the "center of mass" of W corresponds to the expectation value of $\vec{S}$.

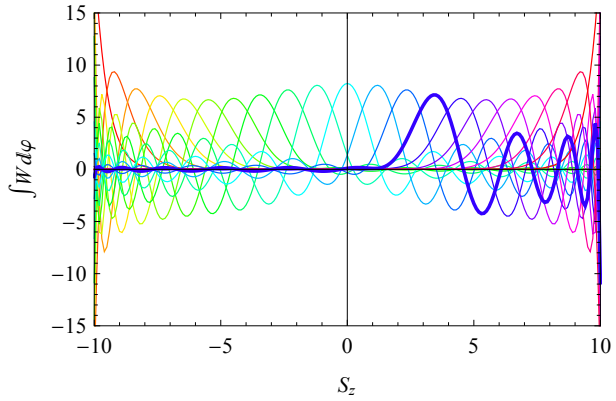

Figure 2.4: Marginal of the Wigner function $W(\vartheta, \phi)$ along $S_z = S\cos\vartheta$ calculated for Dicke states $|S, m\rangle\langle S, m|$ with $S = 10$. The state $m = 3$ is highlighted for clarity.

In contrast to the planar Wigner function, the marginals of W do not directly represent the probability distribution of an observable. Instead, integrating $W(\vartheta, \phi)$ over ϕ gives the distribution

$$P(\cos\vartheta) = \frac{1}{2}\sqrt{2S+1}\sum_{m=-S}^{S}\rho_{mm}\left(\sum_{k=0}^{2S} t_{k0}^{Smm}\sqrt{2k+1}P_k(\cos\vartheta)\right).$$

Figure 2.4 shows these distributions for the Dicke states $|S, m\rangle\langle S, m|$ with $S = 10$. These are peaked functions around $S_z = m$, but they are not strictly positive as would be required for a probability distribution.

The Dicke states are an extreme example, since they are eigenstates of the operator $\hat{S}_z$ that is measured, and the actual probability distributions are discrete delta functions at $S_z = m$. A superposition of Dicke states has a broader probability distribution, and also broader features on the Wigner function. Similarly, the feature size in W perpendicular to a general spin direction $\hat{S}_{\vec{n}}$ can be related to the probability distribution of measuring $\hat{S}_{\vec{n}}$. This can give an intuitive understanding of the usefulness of a state for quantum metrology: smaller features mean that a smaller angular change is needed to "significantly change" the state [67]. In this thesis, we use the spherical Wigner function mostly to provide such an intuitive visualization of quantum states.

2.4.5 Coherent spin state

So far, we have discussed the Dicke states $|S, m\rangle$. Though straight-forward to describe mathematically the Dicke states are not easily prepared in experiments[9],

[9] A measurement of $\hat{S}_z$ stochastically projects the system onto a Dicke state $|S, m\rangle$, and could be used in principle as a generator if post-selection is allowed. However, in our experiment we can only *destructively* measure the atom numbers and we do not have single-atom resolution required to resolve a single Dicke state.

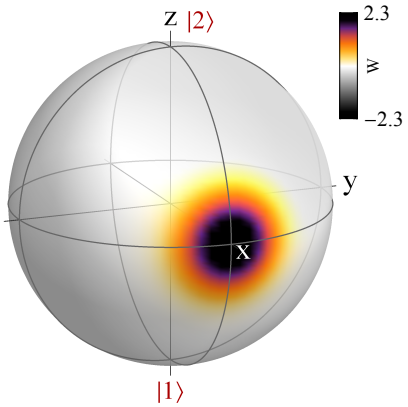

Figure 2.5: Wigner function W of a coherent spin state $|\mathrm{CSS}{:}\pi/2, 0\rangle$, calculated for $N = 20$ atoms.

with the exception of the *stretched states* $|S, \pm S\rangle$. In contrast, a *coherent spin state* (CSS) can be easily prepared (within experimental accuracy) and can be thought of as the "most classical" pure quantum state of the ensemble of two-level systems.

An N-particle coherent spin state is the product of N identical single-particle states $|\vec{s}\rangle$,

$$|\mathrm{CSS}{:}\vartheta, \phi\rangle = |\vec{s}\rangle^{\otimes N}, \tag{2.34}$$

characterized by the angles ϑ, ϕ that correspond to the single-particle Bloch vector $\vec{s}$. The expectation value of the collective spin $\langle \mathrm{CSS}|\vec{S}|\mathrm{CSS}\rangle = N\vec{s}$ has the same angular coordinates on the generalized Bloch sphere.

A CSS can be expanded as a binomial distribution of Dicke states,

$$|\mathrm{CSS}{:}\vartheta, \phi\rangle = \sum_{m=-S}^{S} \left[\binom{N}{x} p^x (1-p)^{N-x} \right]^{\frac{1}{2}} e^{-im\phi} |S, m\rangle, \tag{2.35}$$

with $N = 2S$, $x = S + m$ and $p = \cos^2 \frac{\vartheta}{2}$. Special cases of equation (2.35) are the stretched spin states $|\mathrm{CSS}{:}0, \phi\rangle = |S, S\rangle$ and $|\mathrm{CSS}{:}\pi, \phi\rangle = |S, -S\rangle$, which are independent of ϕ. A general coherent spin state $|\mathrm{CSS}{:}\vartheta, \phi\rangle$ can be generated from a stretched state by a single Rabi pulse. For example,

$$\begin{aligned} |\mathrm{CSS}{:}\vartheta, \phi\rangle &= e^{-i\vartheta \hat{S}_{(\phi + \frac{\pi}{2})}} |S, S\rangle \\ &= e^{-i(\pi - \vartheta) \hat{S}_{(\phi - \frac{\pi}{2})}} |S, -S\rangle. \end{aligned} \tag{2.36}$$

A CSS is a minimum uncertainty state with equal uncertainty in two quadratures. This is most easily shown for the stretched states $|S, \pm S\rangle$, which have variances $\mathrm{var}(\hat{S}_x) = \mathrm{var}(\hat{S}_y) = S/2$ and $\mathrm{var}(\hat{S}_z) = 0$. For a general CSS with

arbitrary ϑ, ϕ the projection noise is

$$\mathrm{var}(\hat{S}_z) = \frac{S}{2} \sin^2 \vartheta. \tag{2.37}$$

Figure 2.5 shows the spherical Wigner function of a coherent spin state with $N = 20$ atoms.

2.5 Atom chips

Among the many ways of preparing and studying ultracold atoms that have been developed in recent years, atom chips [25–27] provide an excellent platform for trapping and manipulating small atomic ensembles in tightly confining microtraps, studying atoms close to a surface and interfacing atoms with magnetic, microwave or optical fields.

An atom chip is a micro-fabricated device structured to interface with neutral atoms close to the chip surface, in an ultra-high vacuum (UHV) environment. Using existing micro-fabrication techniques used in semiconductor technology and solid-state physics, a wide variety of structures and devices can potentially be integrated on atom chips, and structure sizes on the micrometer-scale or even smaller are possible.

The most common atom chip technique uses current-carrying wire structures, which in combination with an external magnetic field provide magnetic potentials for the atoms. Precise control over the trap geometry can be achieved by modulating the wire currents, and various guiding, trapping and transportation configurations have been demonstrated [26]. Wire structures can also be used to carry microwave or radio frequency currents, creating strong near-field gradients close to the surface which can couple on- or off-resonantly to atomic transitions [34, 57, 68, 69]. In this thesis, on-chip microwave fields are a crucial component for generating internal-state dependent potentials.

Other materials than current-carrying wires can be integrated on atom chips. To name a few examples, permanent magnetic materials have been used to create complex trapping potentials [70–72], and on-chip optical fibers and micro-cavities have been used to couple to strong optical fields [73–75].

A practical advantage of atom chips is that they allow for relatively compact experimental setups. Thanks to the tight confinement possible in chip-based traps, fast evaporative cooling to Bose-Einstein condensation is possible compared to traditional free-space BEC experiments. This reduces the required vacuum quality, and allows BEC creation in the same vacuum chamber as loading of a magneto-optical trap from background vapor.

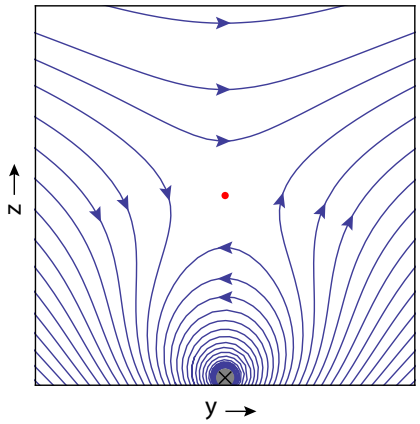

Figure 2.6: Schematic of the magnetic field of a wire guide. The wire carries a current I_L along the x-direction (gray circle, out of plane). A static field B_y is added in the positive y direction. At the red point, the wire field exactly cancels B_y and the total field is zero, creating a so-called quadrupole point. Magnetic field lines are shown in blue.

2.5.1 Magnetic trapping potentials

An atom in a state with $g_F m_F > 0$ can be trapped in the minimum of a magnetic field, with a trapping potential $V(\vec{r}) = g_F m_F \mu_B B$ (see equation (2.7))[10].

Magnetic trap configurations on atom chips have been described in various reviews [25–27, 76, 77]. The basis of most trap designs is formed by a single wire carrying a current I_L, for example in the x-direction, in combination with a static field B_y in the y-direction. This creates a field

$$\vec{B} = \frac{\mu_0 I_L}{2\pi(y^2+z^2)} \begin{pmatrix} 0 \\ -z \\ y \end{pmatrix} + \begin{pmatrix} 0 \\ B_y \\ 0 \end{pmatrix}, \tag{2.38}$$

where the origin is chosen in the wire center. If I_L and B_y have the same sign, the field is zero along a line $z = z_0$ at a distance z_0 above the surface,

$$z_0 = \frac{\mu_0 I_L}{2\pi B_y}. \tag{2.39}$$

Around this field zero the field is a two-dimensional quadrupole field, which can serve as a guide for the atoms. Figure 2.6 shows an example of such a wire guide. The field distribution shows a quadrupole point, which extends infinitely in the x-direction. Any static fields added in the y, z-plane translate the quadrupole point. An offset field B_x in the x-direction does not move the quadrupole point, but it makes the magnitude B nonzero in the center. Therefore, B_x can be used to choose the curvature and thus trap frequency around the field minimum.

[10] Provided that the direction of the atomic angular momentum can adiabatically follow the local field direction as the atom traverses the trap

To create a three-dimensional trap, confinement in the x-direction has to be added. Our main experimental trap is a so-called "dimple" trap, formed by crossing the quadrupole wire with a perpendicular "dimple" wire. For a dimple wire along y with a current $I_D \ll I_L$, a field minimum is created above the wire crossings. Around the minimum, the field can be expanded as [60]

$$\vec{B} = B_0 \begin{pmatrix} 1 \\ 0 \\ 0 \end{pmatrix} + B' \begin{pmatrix} 0 \\ -y \\ z \end{pmatrix} + \frac{B''}{2} \begin{pmatrix} x^2 + (y^2 + z^2)/2 \\ -xy \\ xz \end{pmatrix}, \tag{2.40}$$

where

$$\begin{aligned} B_0 &= |B_x + \frac{\mu_0 I_D}{2\pi z_0}| \\ B' &= \frac{\mu_0 I_L}{2\pi z_0^2} \\ B'' &= \frac{\mu_0 I_D}{\pi z_0^3}. \end{aligned} \tag{2.41}$$

This forms a harmonic potential for an atom with mass m and magnetic moment μ, with trap frequencies[11] [60]

$$\begin{aligned} \omega_l &= \sqrt{\frac{\mu}{m} \frac{\mu_0 I_D}{\pi z_0^3}}, \\ \omega_\perp &= \sqrt{\frac{\mu}{m} \frac{\mu_0^2 I_L^2}{4\pi^2 z_0^4} \frac{1}{|B_x + \frac{\mu_0 I_D}{2\pi z_0}|}}, \end{aligned} \tag{2.42}$$

in the x-direction and the y, z-directions, respectively. Here, z_0 is given by equation (2.39) and B_x is the static field in x-direction. B_x had opposing sign to I_D.

Various other configurations exist for creating three-dimensional confinement and complex trap configurations. Two popular configurations, which we use in different stages of our experiment, are the U-wire potential and the Z-wire trap. A U-shaped wire in combination with a bias field creates a three-dimensional quadrupole potential, which always has a field zero in the center. A Z-shaped wire creates a field similar to equation (2.40), with a finite magnetic field in the center. For a full description of U- and Z-wire traps, see reference [77].

To model the trapping configurations in our experiment, we use a numerical calculation described in section 5.3. Modeling the chip wires as finite conductors, it gives a flexible and accurate description of the trapping fields.

[11] These are angular frequencies defined such that the potential energy $V(r) = \frac{1}{2} m\omega^2 r^2$ for some spatial coordinate r relative to the trap center. We define three orthogonal trap frequencies, where ω_l is taken along the longitudinal axis of the trap.

3

Quantum Metrology

In an atom interferometer, the external (motional) or internal (spin) state of atoms is coherently split and allowed to follow two different pathways [2,3]. During the interrogation time T_R, a phase φ between the paths is accumulated, which depends on the quantity to be measured. When the paths are recombined, the wave-character of the atoms gives rise to an interference pattern, from which φ can be determined. In recording this interference, however, the particle-character of the atoms is revealed, as a measurement randomly projects the wave function of each atom into a definite state. When operating with an ensemble of N uncorrelated (non-entangled) atoms, the resulting binomial statistics of counting individual atoms in the output states limits the phase uncertainty of the interferometer to $\sigma_\varphi \geq 1/\sqrt{N}$, the standard quantum limit (SQL) of interferometric measurement [5].

In this chapter, I first describe the interference pattern of a general interferometer using the language of classical optics, and derive the SQL from the statistics of counting uncorrelated particles. The results are confirmed for the internal state Ramsey interferometer, described more rigorously in the collective-spin language of section 2.4.2.

In *quantum metrology* the SQL is overcome by replacing the uncorrelated particles with a suitably correlated quantum state. The interferometric precision can in theory be improved down to the Heisenberg limit $\sigma_\varphi \geq 1/N$. The usefulness of a particular state for quantum metrology can be characterized by the squeezing parameter, or more generally by the quantum Fisher information. I introduce both concepts, and show examples of useful states that can be generated by the *one-axis twisting* Hamiltonian. Finally, I briefly discuss the relation between quantum metrology and entanglement, which is an active field of theoretical study and debate.

3.1 Classical interferometer

A typical interferometric experiment is depicted schematically in figure 3.1. An input state $|\psi_{\text{in}}\rangle$ is split by a first beam splitter into a superposition of two

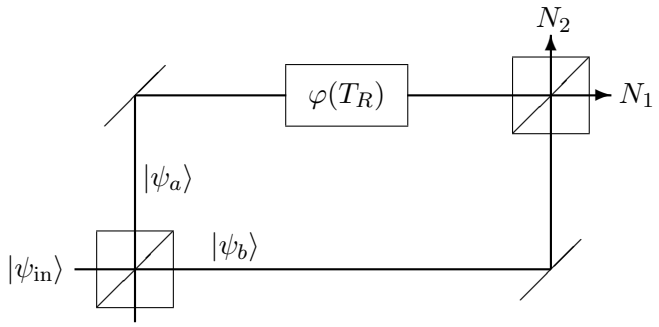

Figure 3.1: Schematic interferometer. We assume a single input state and time-independent H_R.

interferometer pathways, $|\psi_a\rangle$ and $|\psi_b\rangle$. Then, the pathways evolve for a time T_R under the presence of a Hamiltonian H_R through the time-dependent Schrödinger equation, which introduces a relative phase shift φ between the two paths. A second beam splitter recombines the pathways, and the resulting interference fringes are recorded by counting the number of particles N_1 and N_2 in the output arms.

This description applies in principle to any interferometer with two pathways. In a Ramsey interferometer with an ensemble of atoms, two internal states of the atoms are used as interferometer pathways, and resonant Rabi pulses are used as beam splitters, as will be discussed in section 3.3.

After the first beam splitter, choosing real reflection and transmission coefficients R_1 and T_1 (satisfying $R_1^2 + T_1^2 = 1$), we have in the two pathways

$$\begin{aligned} |\psi_a(0)\rangle &= R_1|\psi_{\text{in}}\rangle + T_1|0\rangle \\ |\psi_b(0)\rangle &= T_1|\psi_{\text{in}}\rangle - R_1|0\rangle, \end{aligned} \tag{3.1}$$

where the vacuum state $|0\rangle$ is assumed as the second interferometer input. We first treat the system classically, taking $|0\rangle = 0$.

The system evolves for a time T_R under a Hamiltonian H_R, which depends on the quantity to be measured, and generates a differential phase shift φ,

$$\begin{aligned} |\psi_a(T_R)\rangle &= \alpha_a e^{i\varphi}|\psi_a(0)\rangle \\ |\psi_b(T_R)\rangle &= \alpha_b|\psi_b(0)\rangle. \end{aligned} \tag{3.2}$$

Here, we choose H_R such that $|\psi_b\rangle$ is not affected, and the factors α_a and α_b describe amplitude losses that may occur during T_R in $|\psi_a\rangle$ and $|\psi_b\rangle$, respectively.

At T_R, a second beam splitter recombines the pathways, and creates the output states

$$\begin{aligned} |\psi_2\rangle &= R_2|\psi_a(T_R)\rangle + T_2|\psi_b(T_R)\rangle \\ |\psi_1\rangle &= T_2|\psi_a(T_R)\rangle - R_2|\psi_b(T_R)\rangle, \end{aligned} \tag{3.3}$$

again choosing real coefficients R_2 and T_2.

The interference fringes are then recorded by measuring the populations,

$$\begin{aligned}\langle N_2\rangle &= |\psi_2|^2 = N_{\text{in}}\left(\alpha_a^2 R_1^2 R_2^2 + \alpha_b^2 T_1^2 T_2^2 + 2\alpha_a\alpha_b R_1 T_1 R_2 T_2 \cos\varphi\right) \\ \langle N_1\rangle &= |\psi_1|^2 = N_{\text{in}}\left(\alpha_a^2 R_1^2 T_2^2 + \alpha_b^2 T_1^2 R_2^2 - 2\alpha_a\alpha_b R_1 T_1 R_2 T_2 \cos\varphi\right)\end{aligned} \tag{3.4}$$

where $\langle\cdots\rangle$ denotes the mean or expectation value and $N_{\text{in}} = |\psi_{\text{in}}|^2$. Combining the result,

$$\begin{aligned}\langle N_2 - N_1\rangle &= (N_a - N_b)(R_2^2 - T_2^2) + 4R_2T_2\sqrt{N_aN_b}\cos\varphi \\ \langle N_2 + N_1\rangle &= N_a + N_b = N,\end{aligned} \tag{3.5}$$

where $N_a = |\alpha_a R_1|^2$ and $N_b = |\alpha_b T_1|^2$ are the intensities in arms $|\psi_a\rangle$ and $|\psi_b\rangle$ before the last beam splitter, respectively. The amplitude of the fringes, or interferometric contrast, is largest for $R_2 = T_2 = \frac{1}{\sqrt{2}}$, and best performance is thus obtained with a $50:50$ output beam splitter. In that case, we have

$$\cos\varphi = \frac{\langle N_2 - N_1\rangle}{2\sqrt{N_aN_b}}. \tag{3.6}$$

In general, the largest interferometric contrast is obtained for $N_a = N_b$, such that $2\sqrt{N_aN_b} = N$. In an interferometer without (asymmetric) losses, this situation is obtained by choosing also the input beam splitter with a $50:50$ splitting ratio.

It is convenient to define the relative population difference n as

$$n = \frac{N_2 - N_1}{N_2 + N_1}. \tag{3.7}$$

The expectation value of the interferometer output can then be written as

$$\langle n\rangle = C\cos\varphi, \tag{3.8}$$

where $C \leq 1$ denotes the interferometric contrast,

$$C = \frac{2\sqrt{N_aN_b}}{N}. \tag{3.9}$$

3.2 Standard Quantum Limit

Assuming noiseless detection and constant (or known) total N, we can expand the variance in φ as

$$\sigma_\varphi^2 \approx \left(\frac{\mathrm{d}\varphi}{\mathrm{d}N_2}\right)^2 \sigma_{N_2}^2 = \frac{\sigma_{N_2}^2}{N_aN_b - \frac{1}{4}\langle N_2 - N_1\rangle^2} = \frac{\sigma_{N_2}^2}{N_aN_b\sin^2\varphi}. \tag{3.10}$$

Here, N_1 is perfectly anti-correlated with N_2, and we do not have to consider its variance $\sigma_{N_1}^2$.

If the input state consists of *uncorrelated* particles and H_R contains only single-particle operators, we can equivalently describe the N-particle interferometer as N independent realizations of a single-particle interferometer. In that case, N_2 follows a binomial distribution, where for each realization $\langle N_2\rangle/N$ is the probability to detect the particle in output state 2, such that

$$\sigma^2_{N_2} = \frac{\langle N_1\rangle\langle N_2\rangle}{N} = \frac{1}{4}N - \frac{N_a N_b}{N}\cos^2\varphi, \tag{3.11}$$

For balanced populations $N_a = N_b = N/2$, we have $\sigma^2_{N_2} = \frac{N_a N_b}{N}\sin^2\varphi$ and the phase uncertainty is independent of φ,

$$\sigma^2_\varphi = \frac{1}{N}. \tag{3.12}$$

This is the lowest uncertainty possible with N uncorrelated particles, and can in practice be achieved only with sufficiently suppressed technical noise. Therefore, the *Standard Quantum Limit of interferometery (SQL)* is often written as

$$\sigma^2_\varphi \geq \frac{1}{N}. \tag{3.13}$$

Note that the SQL depends on the *final* atom number N at the end of the interferometer sequence, and not on the initial atom number N_{in}.

If the populations before the last beam splitter are not equal, we have the more general form

$$\sigma^2_\varphi = \frac{N}{4N_a N_b \sin^2\varphi} - \frac{1}{N\tan^2\varphi}, \tag{3.14}$$

and the lowest uncertainty is achieved by operating on the slope of the fringe, at $\langle\cos\varphi\rangle = 0$. The resulting phase uncertainty is

$$\sigma^2_\varphi = \frac{N}{4N_a N_b}. \tag{3.15}$$

Note that, even for balanced populations, operating on the slope of the fringe is often still advantageous[1]. In our experiments, for example, we experience additive detection noise. Since the detection noise in n is independent of φ, it is least significant at $\langle\cos\varphi\rangle = 0$ where the slope of equation (3.8) is maximal.

3.2.1 Linear and non-linear interferometry

In most practical precision measurement experiments, H_R is independent of the number of particles and we can write $H_R = \hbar\omega|\psi_a\rangle\langle\psi_a|$, where ω is (directly related to) the quantity of interest. In such a *linear interferometer* the acquired

[1] A notable exception is the situation where only *one* output port N_2 can be measured, and thus the total N is not known, for example in an optical Michelson interferometer. In that case, it can be advantageous to operate close to the dark fringe, where $N_2 \to 0$ [78].

phase is $\varphi = \omega T_R$, and the signal-to-noise ratio (SNR) for a single run of the experiment is

$$\mathrm{SNR} = \frac{\omega}{\sigma_\omega} = \frac{\omega T_R}{\sigma_\varphi}. \tag{3.16}$$

The standard quantum limit of a linear interferometer can be written as

$$\sigma_\omega^2 \geq \frac{1}{N T_R^2}, \tag{3.17}$$

for a single run of the experiment and equal populations.

Typically, the interferometric measurement is repeated many times, and the long-term performance also depends on the repetition rate. However, for an interferometer on an atom chip, the experimental cycle time is often much longer than T_R, due to the time needed for trapping and cooling the atoms. In our experiment, for example, the cycle time is $T_{\mathrm{cycle}} = 11$ s, and we measure for T_R up to a few hundred ms. Therefore, we can assume the repetition rate to be independent of T_R, and use the SNR defined in equation (3.16) as a measure for the performance of the interferometer. In section 4.2 I will use this definition of SNR analyze interferometric performance in the presence of particle losses.

Note that in general, a more favorable scaling of SNR with N can be achieved using *nonlinear* interferometry, where H_R depends on N. For example, an interferometer using non-linear Faraday rotation of light by a sample of cold atoms has demonstrated a scaling of H_R with the number of photons [79]. However, a nonlinear interaction is only available in specific cases, and most current practical applications of interferometry rely on linear interactions. Note that in this thesis the SQL and Heisenberg limit are defined with respect to estimating the phase φ of the quantum state, and these results do not depend on a linear or non-linear choice of interaction. A rigorous analysis of the quantum limits in linear and non-linear interferometry is given in references [6, 80, 81].

3.3 Internal state Ramsey interferometer

In the previous sections, an optical interferometer has been used as a model system. The results, however, apply to many interferometric scenarios. For internal-state atom interferometry, the direct analogy and most common experiment is the Ramsey interferometer.

In a Ramsey interferometer the role of input and output beam splitters is taken by two $\pi/2$-pulses, which are resonant Rabi pulses (see equation (2.21)) with a duration t such that $\Omega t = \pi/2$. The time between the pulses is the interrogation time T_R, and the interferometric pathways are the internal states $|1\rangle$ and $|2\rangle$ of the atoms. As input to the interferometer, all atoms are polarized in state $|1\rangle$. The interferometer is sensitive to a relative phase φ between $|1\rangle$ and $|2\rangle$ accumulated during T_R.

The action of a Ramsey interferometer can be described in terms of rotations of the collective spin $\vec{S}$ by consecutively applying the actions of each interferometer step. For an input state $|\psi_{\text{in}}\rangle$, the output state of the Ramsey sequence is [82–84]

$$\begin{aligned} |\psi_{\text{out}}\rangle &= e^{i\frac{\pi}{2}\hat{S}_y} \cdot e^{-i\varphi\hat{S}_z} \cdot e^{i\frac{\pi}{2}\hat{S}_y} |\psi_{\text{in}}\rangle \\ &= e^{-i\pi\hat{S}_z} \cdot e^{-i(\varphi-\pi)\hat{S}_x} |\psi_{\text{in}}\rangle, \end{aligned} \tag{3.18}$$

where the phase of both Rabi pulses is chosen equal, and we define this phase to correspond to rotations around $-y$ on the Bloch sphere. The simplification on the second line directly shows that the Ramsey sequence turns the phase φ into a population difference S_z which can be measured.

If initially all atoms are in state $|1\rangle$, the input state of the Ramsey interferometer is the stretched state $|\psi_{\text{in}}\rangle = |S, -S\rangle$. The output state is a coherent spin-state

$$|\psi_{\text{out}}\rangle = |\text{CSS}{:}\varphi, \pi/2\rangle, \tag{3.19}$$

as can be seen from equation (2.36). A measurement of the relative population n yields expectation values of

$$\begin{aligned} \langle n \rangle &= \frac{\langle \hat{S}_z \rangle}{S} = \cos\varphi \\ \sigma_n^2 &= \frac{1}{S^2}\text{var}(\hat{S}_z) = \frac{1}{N}\sin^2\varphi \end{aligned} \tag{3.20}$$

for the mean and variance, respectively. Combining the results and using linear error propagation, the phase sensitivity of an ideal Ramsey interferometer is

$$\sigma_\varphi = \frac{\sigma_n}{\sin\varphi} = \frac{1}{\sqrt{N}}, \tag{3.21}$$

confirming the standard quantum limit of equation (3.13).

It is often useful to add a known phase offset to φ. For example, when $\langle\varphi\rangle$ is approximately known a phase offset can be used to set $\langle n \rangle = 0$ in subsequent runs of the experiment, optimizing the SNR. The offset phase φ_{rf} can be added by changing the phase of the second Rabi pulse. The full Ramsey sequence then becomes

$$\begin{aligned} |\psi_{\text{out}}\rangle &= e^{i\frac{\pi}{2}\hat{S}_{(\varphi_{\text{rf}}+\frac{\pi}{2})}} \cdot e^{-i\varphi\hat{S}_z} \cdot e^{i\frac{\pi}{2}\hat{S}_y} |\psi_{\text{in}}\rangle \\ &= e^{i\frac{\pi}{2}\hat{S}_y} \cdot e^{-i(\varphi+\varphi_{\text{rf}})\hat{S}_z} \cdot e^{i\frac{\pi}{2}\hat{S}_y} |\psi_{\text{in}}\rangle, \end{aligned} \tag{3.22}$$

where $\hat{S}_{(\phi)} = \hat{S}_x\cos\phi + \hat{S}_y\sin\phi$.

Three types of Ramsey experiments are typically performed, differing only in the parameter that is varied to record interference fringes.

1. *Frequency Ramsey*: T_R is kept constant and the Rabi detuning δ is varied. This leads to a somewhat more complicated fringe pattern centered around $\delta = 0$, which is not further discussed here.

2. *Time Ramsey*: The detuning δ is kept fixed on resonance, and the interrogation time T_R is varied. The resulting fringe pattern directly measures the energy difference between $|1\rangle$ and $|2\rangle$, with respect to the co-rotating frame of the Rabi oscillations (see section 2.3.4). If no level shifts are applied ($H_R = 0$), the fringes oscillate with $\varphi = \delta T_R$. Note that for two-photon Rabi pulses in our experiment, δ is nonzero on resonance and a time Ramsey can be used to measure the microwave level shift (see equation (2.18))[2].

3. *Phase Ramsey*: The detuning and T_R are kept constant and instead the offset phase φ_{rf} is varied. The interference fringes then have a known frequency, which is useful in particular to measure the interferometric contrast C.

3.4 Spin-squeezing parameter

It is possible to overcome the SQL using entanglement between the atoms. One way to overcome the SQL is to reduce ("squeeze") the variance in some spin quadrature below that of a coherent state. Since a coherent state is a minimum uncertainty state, the Heisenberg uncertainty principle requires that the variance in the perpendicular ("anti-squeezed") quadrature is increased. Such a state is called a *spin-squeezed state* [85].

In addition to reducing the variance, the interferometric contrast C must remain high to beat the SQL. The contrast is not only affected by technical limitations such as decoherence, but also fundamentally. Because the phase space of the collective spin system is spherical, a large variance in the anti-squeezed quadrature leads to the state "wrapping around" the sphere, reducing the contrast. The maximum contrast of any state is the *length* of the collective spin $C_{\max} = \frac{1}{S}\sqrt{\langle \hat{S}_x\rangle^2 + \langle \hat{S}_y\rangle^2 + \langle \hat{S}_z\rangle^2}$.

To characterize *interferometrically useful* squeezing, the Wineland squeezing parameter ξ is defined as [86]

$$\xi^2 = \frac{N \mathrm{var}(\hat{S}_\theta)}{\langle \hat{S}_x\rangle^2}, \tag{3.23}$$

where the coordinate frame is chosen such that $\langle \vec{S}\rangle \parallel x$, and $\hat{S}_\theta = \hat{S}_z \cos\theta - \hat{S}_y \sin\theta$. Here, θ is a rotation angle around x which may be freely chosen (and

[2] In addition, we often add an "artificial detuning" δ_{clock} by adjusting the Rabi phase $\varphi_{\mathrm{rf}} = \delta_{\mathrm{clock}} T_R$. This aids in resolving the sign of δ and in monitoring the contrast C as function of T_R.

optimized). Again using linear error propagation, the phase uncertainty of a spin-squeezed state is

$$\sigma_\varphi = \xi/\sqrt{N}. \tag{3.24}$$

Thus, the SQL corresponds to $\xi = 1$ and a state with $\xi < 1$ is useful for sub-SQL interferometry. Thus, the squeezing parameter ξ^2 is a measure for *interferometrically useful* squeezing.

Pure states for which $\mathrm{var}(\hat{S}_\theta) < S/2$ but still $\xi > 1$ are called *over-squeezed states*. An extreme example of an over-squeezed state is the Dicke state $|S, 0\rangle$, for which $\mathrm{var}(\hat{S}_z) = 0$, but also $\langle \hat{S}_x \rangle = \langle \hat{S}_y \rangle = 0$, such that the contrast is 0 for every rotation angle.

In an experiment, a measurement of $\mathrm{var}(\hat{S}_\theta)$ can be performed by first rotating by an angle θ around $-\hat{S}_x$, and then measuring the variance $\mathrm{var}(\hat{S}_z) = \langle N \rangle^2 \sigma_n^2/4$. The squeezing parameter is then calculated as

$$\xi^2 = \frac{\langle N \rangle \sigma_n^2}{C^2}, \tag{3.25}$$

where the interferometric contrast $C = \langle \hat{S}_x \rangle / S$ is determined from a separate measurement. In this definition, technical noise sources such as imaging noise increase the measured ξ^2, and therefore ξ^2 compares the sensitivity of an experiment to that of an *ideal* coherent-state-interferometer with the same particle number.

In the context of our experimental results, we also define an alternative parameter which does *not* measure interferometrically useful squeezing, but only measures noise reduction compared to the projection noise of a coherent state. We define

$$\zeta^2 = \langle N \rangle (\sigma_n^2 - \sigma_{n,\mathrm{det}}^2), \tag{3.26}$$

where σ_n^2 is the measured variance in n, and $\sigma_{n,\mathrm{det}}^2$ is the imaging noise, which is determined separately. Subtracting the imaging noise contribution is not meaningful in the context of interferometry, but it can be useful for the characterization of a quantum state (see e.g. section 6.4.1).

3.5 One-axis twisting Hamiltonian

One way to produce spin-squeezed states is with the *one-axis twisting* Hamiltonian [62, 85, 87]

$$H_{\mathrm{int}} = \chi \hat{S}_z^2, \tag{3.27}$$

where χ is an angular frequency characterizing the strength of the twisting. As discussed in section 2.4.3, the one-axis twisting Hamiltonian is present in our two-component BEC due to collisions, and χ can be modified by changing the density overlap between the wave functions of $|1\rangle$ and $|2\rangle$.

The action of H_{int} can be intuitively understood by considering the action of $\hat{S}_z$ on the Bloch sphere, which causes a phase rotation of the entire sphere.

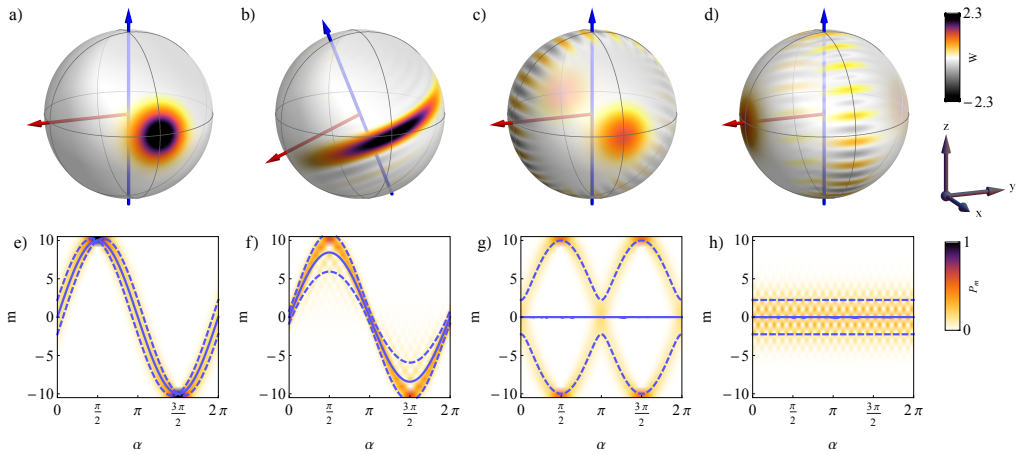

Figure 3.2: Example quantum states for $N = 20$. Top row: Spherical Wigner function W of a) coherent state, b) squeezed state with $\chi t = 0.13$ and c) and d) Schrödinger-cat state generated with $\chi t = \pi/2$. Bottom row: (e-h) Probability distributions of the eigenstates of $\hat{S}_\theta$ corresponding to (a-d). The projection $\hat{S}_\theta$ is taken along the blue axis, after a rotation by an angle α around the red axis. Solid lines show the expectation value of m and dashed lines are offset by $\pm$ one standard deviation.

Loosely speaking, $\hat{S}_z^2$ can be thought of as a phase rotation $\hat{S}_z$ with an angular velocity proportional to the *value* of $\hat{S}_z$. As a result, $\hat{S}_z^2$ "twists" the state on the sphere. In terms of the Dicke states, acting with H_{int} for a time t corresponds to

$$|S, m\rangle \xrightarrow{H_{\text{int}}} e^{-im^2\chi t}|S, m\rangle. \tag{3.28}$$

3.5.1 Spin-squeezed states

Figure 3.2 (a-d) shows the Wigner functions of several example states for $N = 20$. Panels (e-h) of the figure show the probability distribution of the eigenstates of $\hat{S}_\theta$ (taken along the blue axis) after turning by a variable angle α around the axis shown in red. In panels (e, g, and h) $\hat{S}_\theta = \hat{S}_z$ and the probabilities are $P_m = |\langle\psi|S, m\rangle|^2$ for the Dicke states $|S, m\rangle$. These are the detection probabilities at the end of an interferometer sequence.

Sphere a) shows a coherent state $|\text{CSS}{:}\pi/2, 0\rangle$, which is used as the initial state for the other examples. Panel e) shows the corresponding probability distribution. For the coherent state, the phase uncertainty is independent of α.

On sphere b) of figure 3.2, the result of applying H_{int} on the CSS for a duration $\chi t = 0.13$ is shown. As the top part of the Wigner function is rotated towards the right, and the bottom part to the left, the state is "twisted" apart. The resulting state is clearly spin-squeezed: it has a narrower distribution than the CSS along the blue axis (squeezed direction), and a much broader distribution along the perpendicular red axis (anti-squeezed direction). Panel f) shows the corresponding measurement probabilities. Around $\alpha = 0$ the variance of $\hat{S}_\theta$ is

reduced by −8.5 dB compared to that of a coherent state. However, due to the strong squeezing the contrast is also reduced to $C = \langle \hat{S}_x \rangle / S = 84\ \%$. Combined, this state has a squeezing parameter of $\xi^2 = -7.0$ dB.

3.5.2 Schrödinger cat state

For small values of χt, the "twisting" of the Bloch sphere described above gives a good intuition for the squeezed states that are produced, but for larger χt the details of quantum mechanics have to be taken into account. The Wigner function of figure 3.2b shows small fringes on either side of the squeezed state, indicating that some interference effects are present. As H_{int} is applied for longer times complex fringe patterns are formed, corresponding to highly entangled quantum states.

The ability of H_{int} to generate highly entangled states originates from the finite dimensionality of the system, which can be visually understood by considering the spherical phase space: the "twisting" effect leads to states that wrap around the sphere, creating interference effects in the Wigner function. It can be shown that H_{int} in combination with Rabi rotations can generate any spin state in the $S = N/2$ manifold [88]. In an infinite-dimensional system, on the other hand, the phase space is planar and Gaussian (coherent or squeezed) states stay Gaussian under the influence of H_{int}.

It can be seen from equation (3.28) that for certain values of χt all Dicke states gain the same phase shift. For a general input state, this means that there will be a *revival* of the input state. The first revival occurs at $\chi t = \pi$ [89]. To show this, we have to treat integer and half-integer values of the collective spin S separately.

- For half-integer S, each $|S, m\rangle$-component of the input state gains a phase shift $e^{-i\pi(k^2+k+1/4)}$ for an integer $k = m - \frac{1}{2}$. Since $k^2 + k$ is always an even number, this results in only a global phase shift $e^{-i\pi/4}$ which has no physical meaning.
- For integer S, the phase shift gained by component $|S, m\rangle$ is $e^{\pm i\pi}$ for even $(+)$ and odd $(-)$ m. This is identical to a phase rotation $e^{i\pi \hat{S}_z}$, and thus the resulting state is a rotated version of the input state.

Apart from the complete revival of the input state when χt is a multiple of π, more interesting rephasing effects occur at *partial revivals*. At $\chi t = \pi/2$, half of the Dicke states are rotated by π and the other half back at their original phase. When applied to a coherent input state on the equator of the Bloch sphere ($\langle \hat{S}_z \rangle = 0$), this generates a *Schrödinger cat* state, named after Schrödinger's famous thought experiment and also known as the Greenberger-Horne-Zeilinger (GHZ) state. The prototype of a Schrödinger cat or GHZ state is

$$|\text{cat}\rangle = \frac{1}{\sqrt{2}} \left(|S, -S\rangle + |S, S\rangle \right). \tag{3.29}$$

This means that upon measurement either all atoms are found in state $|1\rangle$, or all atoms are found in $|2\rangle$, with equal probability. A cat state is a maximally entangled state [90], which is intuitively demonstrated by the fact that knowing the measurement outcome for any one particle fixes the outcome of all other particles – the measurement outcomes are fully correlated. Here, we use the term Schrödinger cat state to refer either to the state $|\text{cat}\rangle$, or any state that can be mapped to $|\text{cat}\rangle$ by applying global rotations on the Bloch sphere.

Sphere c) of figure 3.2 shows a Schrödinger cat state generated by applying H_{int} for $\chi t = \pi/2$ on the initial state of sphere a) for $N = 20$ atoms. It is a cat state along x, and shows half the population of a coherent state at x and half at $-x$ on the Bloch sphere. Between these points is a ring of N fringes in the y, z-plane of the sphere. These fringes signify the entanglement, and distinguish a pure cat state from a statistical mixture of two coherent states.

Panels g) and h) show the probability distributions for measurement outcomes of $\hat{S}_z$ after rotating around the $-y$ and x axes, respectively. When rotating around $-y$, the distribution splits into two branches, producing the state of equation (3.29) at $\alpha = \pi/2$. Interestingly, the expectation value $\langle \hat{S}_z \rangle = 0$ for all angles, showing that the mean measurement outcome is not a useful interferometric signal for rotations around this axis. However, the variance of $\hat{S}_z$ does vary with angle (although it is always at least that of a coherent state), and can be used as an interferometric signal. For rotations around x shown in panel h), both the mean and variance of $\hat{S}_z$ are independent of angle. However, a checkerboard fringe pattern is visible in the probability distribution.

Since the mean of a measurement in any spin direction is 0, the squeezing parameter of a Schrödinger cat state is infinite. However, this does not mean the cat state is not useful for quantum metrology. On the contrary; it can be shown directly that a cat state can be used to attain the Heisenberg limit $\sigma_\varphi = 1/N$ in an interferometer, provided that a suitable measurement is used for readout [81, 91]. It is worth noting that the derivations found in the literature generally use local measurements, where the state of each particle can be measured separately[3], whereas for our two-component BEC we can only measure the *total* spin projection $\hat{S}_z$. However, using a Bayesian estimation scheme the Heisenberg limit can be approached for a large number of repeated measurements [67].

While cat states are promising for metrology in theory, they are extremely sensitive to losses. Since there are N fringes on the Bloch sphere, the loss of a single particle changes the fringe pattern, and in an experimental realization even small fluctuations in N will wash out the signature of entanglement.

The Hamiltonian H_{int} can also be used to generate variants of the cat state. For example, after $\chi t = \pi/3$ a *triple cat* state is produced, which is like the normal cat state but with three-fold instead of two-fold symmetry. Another alternative is using different input states before applying H_{int}. When a coherent

[3] Some derivations use a global but strongly correlated measurement, but in [81] it is shown explicitly that classically correlating local measurements is equivalent.

state $|\mathrm{CSS}{:}\vartheta, \phi\rangle$ with a small angle ϑ is used, a analog to the cat is produced at $\chi t = \pi/2$ where the two "blobs" of the cat state are not on opposing sides of the Bloch sphere, but close together separated by an angle 2ϑ. The advantage of such a state is that only a few fringes are produced, which makes the state more robust to losses (but it cannot achieve the Heisenberg limit). We call this kind of state a "Schrödinger kitten" state.

3.6 Quantum Fisher information

The results of the previous section demonstrate that the squeezing parameter ξ^2, while useful for moderately spin-squeezed states, does not characterize the usefulness of highly entangled states for quantum metrology. The limitations of the squeezing parameter result from two assumptions. First, it assumes the measurement performed is a projection onto the total spin $\hat{S}_\theta$. Although the angle θ can be freely chosen, other quantum measurements may give better results[4]. Secondly, it assumes that the phase is estimated from the measurement result by using the (sample) mean $\langle \hat{S}_\theta \rangle$ as an estimator.

3.6.1 Fisher information

The second issue can be avoided by considering the Fisher information F instead of means and variances. Suppose some parameter φ is measured, and the probability to get measurement outcome x is described by a probability density function (PDF) $P(x|\varphi)$. The Fisher information is defined as [92]

$$F = -\left\langle \frac{\partial^2}{\partial \varphi^2} \log P(x|\varphi) \right\rangle, \tag{3.30}$$

where $\langle f \rangle = \int P(x|\varphi) f(x)\, dx$ denotes the expectation value calculated with the same PDF. Here, $P(x|\varphi)$ is not used as a function of x, but rather as a function of φ. This way it is sometimes called the *likelihood function* $P(\varphi|x)$, describing the probability that the parameter value was φ for a given measurement outcome x. The Fisher information gives an estimate for how much information a measurement outcome x gives about the value of the parameter φ. It does so by estimating the curvature of the log-likelihood function, essentially estimating how "sharply peaked" $P(\varphi|x)$ is in φ.

Related to the Fisher information is the Cramér-Rao bound (CRB), which states that the variance of any unbiased estimator is bounded by [92]

$$\sigma_\varphi^2 \geq \frac{1}{F}. \tag{3.31}$$

[4] Note that in our experiment, and for indistinguishable particles in general, we are in fact limited to measuring projections of the total spin $\hat{S}$. When the particles can be individually addressed, however, other projective measurements exist.

An estimator is any procedure to extract (estimate) φ from the measured result, and an unbiased estimator yields *on average* the true value of φ.

When taking a set X consisting of M independent measurements, the CRB is sometimes written as $\sigma_\varphi^2 \geq \frac{1}{MF}$, with F calculated for a single measurement. Equivalently, one can calculate F directly for the set of measurements, with the total PDF $P_M(X|\varphi) = \Pi_{i=1}^M P(x_i|\varphi)$.

The Fisher information and the CRB give a benchmark to check whether an estimation procedure is efficient. For example, for a set of M measurements x_i drawn from a Gaussian probability distribution with mean φ, the sample mean $\mu = \frac{1}{M}\sum_{i=1}^M x_i$ is an unbiased estimator whose variance $\langle\mu^2\rangle - \langle\mu\rangle^2$ is equal to the CRB [92]. Thus, in this case the sample mean is an optimal unbiased estimator of φ. This confirms that the squeezing parameter ξ^2 is sufficient to describe the usefulness of coherent and mildly squeezed states for metrology, since for these states the PDF is very close to Gaussian.

3.6.2 Quantum Fisher information and the Heisenberg limit

The Fisher information can be extended to measure the information a quantum state gives about the parameter φ, by realizing that the probability distribution $P(x|\varphi)$ can correspond to the quantum-mechanical probability distribution of measurement outcomes for any measurement of choice on the state. The quantum Fisher information F_Q is defined as the largest value of F optimized over all possible measurements on the quantum state [67]. This makes F_Q a property of the quantum state, and not of any specific measurement and estimation procedure. The quantum Cramér-Rao bound states that $\sigma_\varphi^2 \geq \frac{1}{F_Q}$ and for a coherent state $F_Q = N$.

We can now define a more general alternative to the spin-squeezing parameter ξ^2. An N-particle quantum state is useful for metrology with sub-SQL precision if and only if [67]

$$\Xi^2 \equiv \frac{N}{F_Q} < 1. \tag{3.32}$$

For any state $\Xi^2 \leq \xi^2$ [7], and there are states that are not squeezed (i.e., $\xi^2 \geq 1$) but that are still useful for quantum metrology ($\Xi^2 \leq 1$). Examples of such states are over-squeezed states.

The quantum Fisher information can be used to derive the the ultimate phase sensitivity that can be obtained with any N-particle quantum state, the Heisenberg limit $\sigma_\varphi = 1/N$ [6,7]. The the Schrödinger-cat state discussed in section 3.5.2 is an example of a state that can attain the Heisenberg limit.

3.6.3 Estimation strategies

The (quantum) Fisher information determines how much information on φ is available from a quantum state or data set, but it does not specify how to extract this information. There is no general guarantee that an optimal estimator

that attains the CRB can be found for a given probability distribution. However, in many cases the maximum-likelihood estimator (MLE) can be found, which is approximately optimal for large data sets (large M). It is found by maximizing $\log P(x, \varphi)$ as a function of φ [92]. When this is not possible analytically, which often the case for large parameter spaces, numerical maximization may be possible.

A similar numerical method to find a nearly optimal estimate of φ is Bayesian estimation scheme [67, 93]. In Bayesian estimation, the likelihood function after M measurements is estimated to be $P_M(\varphi|X) = \Pi_{i=1}^{M} P(x_i|\varphi)P(\varphi)/P(x_i)$, where $P(\varphi)/P(x_i)$ is a normalized distribution describing any *prior knowledge* of φ that may be available. One advantage of Bayesian estimation is that it can be used iteratively as more measurement data comes available, by using the last estimate of $P_M(\varphi|X)$ as the prior knowledge. In an interferometer, fast convergence to the CRB can often be obtained by iteratively adjusting the offset phase to the position where most information is expected to be available (e.g., the best estimate of slope of the interference fringe).

Another practical concern in both classical and quantum interferometers is to keep track of the *total* phase acquired during T_R. A classical interferometer measures the phase φ modulo 2π, and for example a Schrödinger-cat-state interferometer even measures φ modulo $2\pi/N$. As a result, the sensitivity analysis in this chapter only applies to measuring the *least significant digit* of φ. This problem can be solved by repeating measurements for different values of T_R. Although this reduces the sensitivity, for large data sets most measurements can be devoted to measuring the least significant digit and the sensitivity predicted by the relevant CRB can be approached. Several adaptive algorithms have been proposed to get fast convergence to the optimal phase sensitivity [81, 94, 95]

3.7 Spin squeezing and entanglement

A quantum state of N particles characterized by a density matrix $\hat{\rho}_{\text{sep}}$ is called *separable* if it can be written as [67]

$$\hat{\rho}_{\text{sep}} = \sum_k p_k \hat{\rho}_k^{(1)} \otimes \hat{\rho}_k^{(2)} \otimes \cdots \otimes \hat{\rho}_k^{(N)}, \tag{3.33}$$

with normalized positive weights p_k and $\hat{\rho}_k^{(i)}$ the single-particle density matrix of the ith particle. Any state which *cannot* be written as a separable state, is called an *entangled* state.

There is a large theoretical interest in the role of entanglement in quantum technologies, and quantum metrology and entanglement are closely related concepts. A separable state has been shown to have $\xi^2 \geq 1$, and thus a spin-squeezed state is necessarily an entangled state [87]. Later, the more general statement that any state with $F_Q > N$ is entangled has been shown [67], and both statements have been extended to the case of a fluctuating number of particles [7].

Although not every entangled state is useful for quantum metrology [67, 83], entanglement between particles is a requirement for sub-SQL interferometry and can thus be seen as the key resource for quantum metrology.

Extending these results, spin-squeezing and the quantum Fisher information can also be used to classify the *depth of entanglement*. For this, the notion of separability is extended as follows: a state is said to be *k-producible* if it can be written as a product of density matrices that contain at most k particles each. This means it can be produced from a separable state with interactions between at most k particles. If a state is not k-producible, it must be at least $(k+1)$-particle entangled [96]. An N-particle entangled state can be called a maximally entangled state.

Several measures have been established to classify states by finding a lower bound on k. For spin-squeezed states, a lower bound can be established based on the variance $\mathrm{var}(\hat{S}_\theta)$ in the squeezed direction and the interferometric contrast C [97]. This is an experimentally useful entanglement measure, since the variance and contrast can be directly measured. In section 6.4.1 we use this method to calculate the (minimum) depth of entanglement of experimentally generated spin-squeezed states. This entanglement measure has been generalized to states with a fluctuating total number of particles [98].

A tighter bound on the depth of entanglement can be obtained from the quantum Fisher information. The Fisher information of a k-particle entangled state is bounded by [96]

$$F_Q \lesssim Nk. \tag{3.34}$$

A state with larger F_Q is thus at least $(k+1)$-particle entangled. The approximation in equation (3.34) is exact when N/k is integer, such that N/k separate groups of exactly k entangled particles each can be formed. When N/k is non-integer the best possible F_Q is smaller, because there will be one "remainder"-group with less than k particles.

3.7.1 Indistinguishable particles

In the definition of entanglement (equation 3.33), it is implicitly assumed that the particles are distinguishable. For indistinguishable particles, it is not meaningful to talk about the ith particle, and $\hat{\rho}_{\mathrm{sep}}$ is not a valid quantum state [99]. There is an ongoing theoretical debate on the concept, definition and meaning of entanglement for indistinguishable particles, and its relation to quantum metrology (see e.g. [100, 101] and references therein).

A natural way to define entanglement of indistinguishable bosons is to say that a separable pure state of N such particles can be written as $|\psi\rangle^{\otimes N}$, with $|\psi\rangle$ a single-particle state [98]. In this definition, the squeezing parameter and Fisher information can still be used to identify entangled states. However, the concept of k-particle entanglement has no meaning, since either *all* or *none* of the particles are entangled.

Other authors argue that the definition of entanglement has to be de-coupled from the notion of particles altogether. In references [99,100] a definition based on entanglement of modes is used. In such a definition, the choice of basis (modes) affects whether or not a particular state is entangled, and furthermore sub-SQL interferometry is possible with mode-separable states [102]. Interestingly, sub-SQL interferometry seems to require either mode-entangled input states, or the interferometric phase shift needs to be generated by an operation that is not local to the chosen modes [99, 102].

An interesting subtlety is highlighted in reference [98]. While a BEC at zero temperature clearly consists of indistinguishable particles, a thermal ensemble of (cold) bosons can be treated as distinguishable. Unless the temperature is very close to the BEC transition, the probability of two atoms occupying the same motional state is negligible, and the motional state can be used to label the particles (even if it is not experimentally resolved).

Whichever definition of entanglement is most appropriate for theoretical analysis does not affect the metrological gain obtained in quantum metrology experiments. In relation to the experiments presented in this thesis I will speak of particle entanglement without taking (in)distinguishability into account. It is worth pointing out, however, that the sub-SQL precision obtained in our experiment is the result of interparticle collisions, and it can be instructive to think of correlations between particles as the resource used for quantum metrology.

3.8 Previous work on quantum metrology with atomic ensembles

In recent years, a range of suitable entangled states for quantum metrology has been created in atomic ensembles, and several demonstrations of entanglement-enhanced interferometry have been reported.

In the group of M. Oberthaler, squeezing of motional states of $\xi^2 = -3.8$ dB was demonstrated using collisional interactions between several wells of an optical lattice potential [8]. In the same group, spin squeezing of the internal states $|F = 1, m_F = 1\rangle$ and $|F = 2, m_F = -1\rangle$ of ^{87}Rb with the one-axis twisting Hamiltonian was demonstrated, using a Feshbach resonance to control χ. A squeezed state with $\xi^2 = -8.2$ dB with $N = 2300$ atoms distributed over 6 wells of the optical lattice was achieved. The state was used in a squeezed-state interferometer achieving $\xi^2 = -1.4$ dB after an interrogation time of 2 µs [20].

The group of E. Polzik has demonstrated spin squeezing of $\xi^2 = -3.4$ dB in an ensemble of $N = 10^5$ cold Cs atoms in an optical dipole trap, where the squeezing was generated with quantum non-demolition (QND) measurements of S_z [9]; and using the same technique has demonstrated a squeezed-state interferometer operating $\xi^2 = -1.1$ dB below the SQL after an interrogation time of $T_R = 10$ µs in $N = 10^5$ atoms [21]. In the same group, entanglement-enhanced magnetometry

was demonstrated with 1.5×10^{12} Cs atoms in a vapor cell, reaching a sensitivity of $\xi^2 = -1.6$ dB and an entanglement lifetime of 4 ms [23]. In that experiment, the entanglement was created with strong atom-light interactions.

QND measurements have also been used to prepare spin-squeezed state in the group of V. Vuletić. Using cavity-enhanced QND measurements, spin squeezing of $\xi^2 = -3.0$ dB was demonstrated in an ensemble of 5×10^4 trapped ^{87}Rb atoms [10]. The same group has used cavity-based atom-light interactions to generate the one-axis-twisting Hamiltonian. With that technique, $\xi^2 = -5.6$ dB of spin-squeezing was demonstrated with 5×10^4 ^{87}Rb atoms [11], and a squeezed-state interferometer with $\xi^2 = -4$ dB and an interrogation time of $T_R = 600$ µs was shown with 3×10^4 atoms [22].

In the group of M. Mitchell, QND measurements were used to realize a magnetometer operating at $\xi^2 = -2.0$ dB in an ensemble of 8.5×10^5 ^{87}Rb atoms [24]. Very recently, the group of J. Thompson has demonstrated states with $\xi^2 = -10.2$ dB of spin squeezing by QND measurements in an ensemble of 5×10^4 ^{87}Rb atoms [18].

In our group, spin-squeezed states have been previously generated with $\xi^2 = -2.5$ dB in an ensemble of $N = 1250$ ^{87}Rb atoms on an atom chip [12], using the same techniques as described in this thesis, but an interferometer operating beyond the SQL had not yet been demonstrated.

Other useful states for quantum metrology have been demonstrated as well. The concept of spin-squeezing was generalized to spin-1 systems, and −8.3 dB of generalized spin-squeezing was observed in reference [17]. Recently, in reference [19], a macroscopic singlet state with a total collective spin of 0 was demonstrated with 3 dB of generalized squeezing in 5.5×10^5 atoms.

So-called twin-atom states, which contain an equal number of particles in each of two modes, have been generated in several experiments [13–16]. These are essentially the Dicke states $|S, m\rangle$, but have fluctuating total atom number. They are not spin-squeezed, since the interferometric contrast is zero, but are useful for quantum metrology if an appropriate estimation strategy is used (see section 3.6). In reference [14], a sensitivity of −1.6 dB in variance below the SQL is demonstrated by using $\mathrm{var}(\hat{S}_z)$ as estimator of the phase, and a Fisher information of $F_Q \geq 1.45 \times \langle N \rangle$ was reported.

4

Atom interferometry with high spatial resolution

In principle, quantum metrology is relevant to any interferometer, but creating and exploiting the required entanglement is often challenging in practice. Therefore, interferometric performance can often be more easily improved by increasing the number of particles N. However, in some situations N is fundamentally limited by a physical process, and entanglement-enhanced interferometry is particularly useful in such situations.

One situation where N is limited is in gravitational wave detectors, which are optical interferometers that aim to detect gravitational waves by monitoring the path length in a Michelson interferometer. While larger photon number N still reduces the relative phase uncertainty of the light in such an interferometer, the amplitude uncertainty increases, causing fundamental fluctuations in the radiation pressure force on the interferometer mirrors. This in turn translates into fluctuating mirror positions, and there exists an optimum N where phase and amplitude fluctuations balance [103][1]. Additional power limits arise from thermal deformation of the interferometer optics [105]. Recently, the sensitivity was improved beyond the shot-noise limit in the GEO 600 gravitational wave detector by applying squeezed states of light to the second (vacuum) input port of the interferometer [105], demonstrating the usefulness of quantum metrology in a situation where N is limited.

In atom interferometers N can be limited by density-dependent effects. For example, in atomic clocks the absolute accuracy is as important as the precision, and chip-based clocks suffer from density-dependent level shifts which limit the usable atom number to $N \lesssim 10^5$ [106]. Another scenario, which I will in this thesis, is when high spatial resolution is desired. A high-spatial-resolution interferometer necessarily requires a small probe volume, and the number of atoms in a small volume is fundamentally limited by density-dependent losses due to

[1] In fact, in a gravitational wave detector the standard quantum limit is usually defined as the uncertainty in path length at the optimum N, and it only depends on the interrogation time and the mirror mass [104].

collisions. Therefore, high-spatial-resolution interferometry is a useful application of quantum metrology. Additional fundamental limits to both N and the interrogation time arise from dephasing effects.

In this chapter, I discuss how density-dependent collisions limit atom interferometry with high spatial resolution, and apply the results to our experimental situation. I consider using a single atomic ensemble as a probe, whose size determines the spatial resolution. Such an ensemble can be used in a scanning-probe measurement to measure e.g. a spatial field distribution. The probe size in such a measurement must be smaller than the structure size of the field distribution. One can alternatively imagine using a larger one-dimensional or two-dimensional probe which is imaged with high resolution, but similar limits to the density apply. The relevant quantity is then the number of atoms in a single resolution element. At the end of the chapter, I discuss the effect of field gradients, sources of phase decoherence in Bose-Einstein condensates, and give an overview of relevant experimental work that has been done previously.

4.1 Density-dependent losses

Trapped atomic ensembles generally suffer from collisional losses, where inelastic collisions between two or more atoms cause all involved particles to be lost from the trap. Since the collision rate depends on the density in the ensemble, these losses place a fundamental restriction on the usable number of particles in an experiment, depending on the desired probe volume and interrogation time.

In this section I derive the evolution of the mean atomic density in the presence of multi-body loss processes in general, and for our experimental situation with ^{87}Rb atoms in particular[2].

4.1.1 Loss processes in a single ensemble

For an ensemble of atoms of a single species and with a single internal state under the influence of several m-body loss processes, where $m = 1, 2, 3, \cdots$, the mean atom number N evolves as

$$\frac{\mathrm{d}N}{\mathrm{d}t} = -\sum_m k_m N^m, \tag{4.1}$$

The rates k_m depend on the density profile, which may in turn depend on time. Writing the number density of the cloud as $n(\vec{r}) = N\eta(\vec{r})$, where $\eta(\vec{r})$ is the normalized density profile, such that $\int \eta(\vec{r})\mathrm{d}^3\vec{r} = 1$, we can write

$$k_m = \kappa_m \int \eta(\vec{r})^m \mathrm{d}^3\vec{r}. \tag{4.2}$$

[2] Although here we restrict our analysis to the mean atom number, collisional losses in general also affect the *fluctuations* in atom number [107].

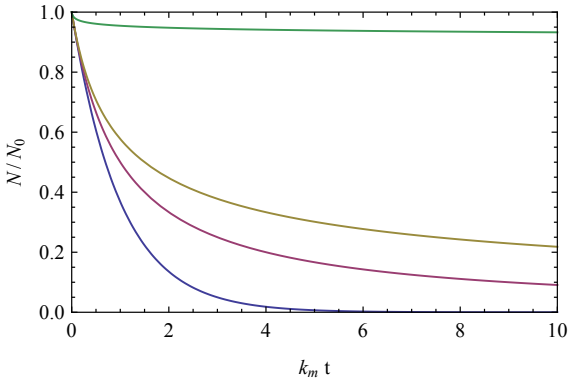

Figure 4.1: Example loss curves for one-body (blue), two-body (purple), three-body (yellow) and 100-body (green) losses. The horizontal axis is scaled such that the initial slope is the same, but higher-order loss processes slow down as the density decreases.

where κ_m is a property of the atomic species and internal state, and has units of volume$^{(m-1)}$/time. In the analysis below we assume $\eta(\vec{r})$, and therefore k_m, to be independent of time. While this is not generally true for a BEC, it provides a simple estimate of the loss processes. For more rigorous results, the density-dependent losses can be included in the GP equations (2.4), as is done in reference [64].

For a single loss process, equation (4.1) can be solved in general,

$$N(t) = N_0 \left((m-1)N_0^{m-1}k_m t + 1\right)^{\frac{1}{m-1}}, \tag{4.3}$$

where $N_0 = N(0)$. For example, for one-, two- and three-body loss,

$$\begin{aligned} N(t) &= N_0 e^{-k_1 t} && \text{(limit } m \to 1) \\ N(t) &= N_0 \frac{1}{1 + N_0 k_2 t} && (m = 2) \\ N(t) &= N_0 \frac{1}{\sqrt{1 + 2k_3 N_0^2 t}} && (m = 3) \end{aligned} \tag{4.4}$$

Figure 4.1 shows example loss curves for different single loss processes. For any m, the initial slope of the relative atom number $N(t)/N_0$ is given by $-k_m$. For larger m, however, the decay flattens off over time as the remaining density decreases and the collision probability goes down.

4.1.2 Experimental situation

Our experiment operates with the $|1\rangle = |F = 1, m_F = -1\rangle$ and $|2\rangle = |F = 2, m_F = 1\rangle$ states of ^{87}Rb. A superposition or mixture of these states suffers from two-body losses in $F = 2$, three-body losses in $F = 1$ and $F = 2$, and interstate two-body losses. The interstate losses result from collisions between

an $F = 1$ atom and an $F = 2$ atom. In addition, the experiment suffers from one-body losses due to collisions with the background vapor. The total system for a mixture of the two states evolves as

$$\begin{aligned} \frac{\mathrm{d}N_a}{\mathrm{d}t} &= -k_1 N_a - k_{3,1} N_a^3 - k_{2,\mathrm{i}} N_a N_b \\ \frac{\mathrm{d}N_b}{\mathrm{d}t} &= -k_1 N_b - k_{2,2} N_b^2 - k_{3,2} N_b^3 - k_{2,\mathrm{i}} N_a N_b, \end{aligned} \tag{4.5}$$

where N_a and N_b are the time-dependent atom numbers in state $|1\rangle$ and $|2\rangle$, respectively, during the interrogation time of the interferometer.

The relevant loss rate constants have been measured in several experiments,

F=1 three-body losses:	$\kappa_{3,1} = 5.8 \times 10^{-42}$ m^6/s	[108]
F=2 two-body losses:	$\kappa_{2,2} = 8.1(3) \times 10^{-20}$ m^3/s	[64]
F=2 three-body losses[3]:	$\kappa_{3,2} = 18(5) \times 10^{-42}$m^6/s	[109]
Interstate two-body losses:	$\kappa_{2,\mathrm{i}} = 1.6(2) \times 10^{-20}$ m^3/s	[64]
Background losses:	$\kappa_1 \approx 0.45$ s^{-1}	

The background loss rate depends on Rb vapor pressure and vacuum quality, and was chosen to match our experimental data.

As described in section 5.4, we approximate the atomic density profile by a Thomas-Fermi profile (inverted parabola) with radii $R_x = 4.0$ µm and $R_y = R_z = 1.05$ µm for $N = 1400$ atoms. By numerical integration, we obtain

$$\begin{aligned} \int \eta^2 \mathrm{d}^3\vec{r} &= 7.73 \times 10^{16}\ \mathrm{m}^{-3}, \\ \int \eta^3 \mathrm{d}^3\vec{r} &= 6.97 \times 10^{33}\ \mathrm{m}^{-6}. \end{aligned} \tag{4.6}$$

We verify these parameters by comparing the numerical solution of equation (4.5) to experimental data. Figure 4.2 shows decay curves measured in our experiment for an ensemble of $N_0 \approx 1440$ atoms in an equal superposition of $F = 1, m_F = -1$ and $F = 2, m_F = 1$, together with the numerical result. After adjusting the background loss rate to $\kappa_1 \approx 0.45$ s to match the tail of the decay in $F = 1$, we find good agreement between the literature values and our experiment. We find that the three-body losses have no significant effect at our experimental density. The short-time behavior of both states is dominated by $\kappa_{2,2}$ and $\kappa_{2,\mathrm{i}}$, whereas for longer times the $F = 2$ population is nearly depleted, and the decay for $F = 1$ is determined only by the background losses κ_1.

[3] The value used for $\kappa_{3,2}$ was measured for the $F = 2, m_F = 2$ state. An accurate value for $F = 2, m_F = 1$ is not available, since the two-body loss dominates at typical experimental densities, including the present experiment.

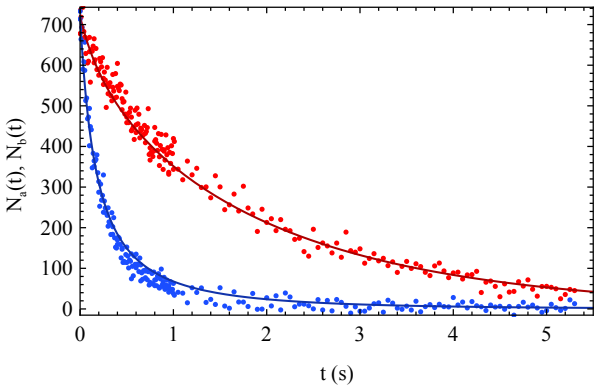

Figure 4.2: Comparison of numerically integrated loss equations (equation (4.5), solid lines) with experimental data (points), for N_a (red) and N_b (blue). The data were taken with an initial atom number of $N_0 \approx 1440$, using an equal superposition of $F = 1$ and $F = 2$. The one-body loss rate in the model was adjusted to match the experimental data, all other parameters are fixed to literature values.

4.2 Interferometry with density-dependent losses

As discussed in section 3.2, the performance of an interferometer using uncorrelated particles is limited by the standard quantum limit (SQL). Equation (3.17) shows that using a large total particle number N and long Ramsey time T_R is generally favorable in an interferometer. However, as discussed in the previous section, collisional losses generally limit the total density after a time T_R, and especially when high spatial resolution is desired, limits the regime of the interferometer to lower N and/or shorter T_R. In this section, I calculate the effect of collisional loss processes on the SQL for our experimental situation.

4.2.1 Interferometry with two-body losses

First, we consider the interferometric performance in the presence of only interstate two-body losses, characterized by $k_{2,\mathrm{i}}$. This is a symmetric loss process: the losses affect both arms of the interferometer in the same way. To maximize the interferometric contrast, the final populations in the two states should be equal, which for the symmetric case is achieved with an equal initial splitting ratio $R_1 = T_1 = 1/\sqrt{2}$, such that $N_a = N_b = N/2$ at all times.

The set of equations (4.5) reduces to a single equation for the total atom number,

$$\frac{\mathrm{d}N}{\mathrm{d}t} = -\frac{1}{2}k_{2,\mathrm{i}}N^2 \tag{4.7}$$

with the same form as the two-body loss equation in a single ensemble (equation (4.1) with $m = 2$), with $k_2 = k_{2,\mathrm{i}}/2$. The solution is given in equation (4.4).

The number of particles $N(T_R)$ *at the end* of the interferometer sequence defines the SQL and thus the achievable precision. The signal-to-noise ratio after

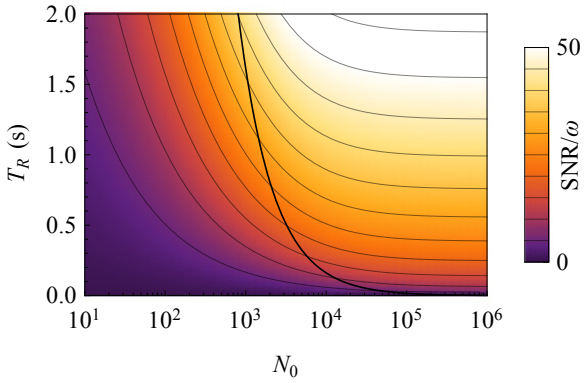

Figure 4.3: Signal-to-noise ratio (SNR) for an interferometer suffering from inter-state two-body losses, using our experimental parameters. The thick black line is the condition where half of the initial population was lost ($N_0 k_2 T_R = 1$), and the SNR starts to saturate.

a single realization of the experiment is

$$\mathrm{SNR} = \omega T_R \sqrt{N(T_R)} = \omega T_R \sqrt{\frac{N_0}{1 + N_0 k_2 T_R}}. \tag{4.8}$$

For $T_R \ll (N_0 k_2)^{-1}$ the SNR increases linearly with T_R, and for small N_0 the SNR increases as $\sqrt{N_0}$, as expected from the standard quantum limit. However, for $N_0 > 1/(k_2 T_R)$ the SNR saturates, and further increasing N_0 gives no more improvement in the final performance. Figure 4.3 shows the saturation behavior for our experimental parameters.

This result can be generalized to any symmetric m-body loss process with equal initial populations. The SNR saturates for large N_0, with the saturation point

$$N_0 > ((m-1) k_m T_R)^{\frac{1}{m-1}} . \tag{4.9}$$

At this point, a fraction $2^{\frac{1}{1-m}}$ of the initial population is left after T_R and the SNR is

$$\mathrm{SNR} = \omega T_R \, 2^{\frac{1}{2-2m}} \sqrt{N_0}. \tag{4.10}$$

A single *asymmetric* loss process, where the loss events occur only within one state, shows a similar saturation behavior of the SNR. However, with the same loss constant the maximum SNR is higher.

4.2.2 Interferometry with multiple loss processes

To take all loss processes into account, we solve equations (4.5) numerically for different N_0, still assuming a balanced initial population ($N_a = N_b$ at $T_R = 0$).

Figure 4.4 shows the resulting SNR as function of N_0 and T_R. Due to to the presence of *both* symmetric and asymmetric loss processes, there is a strict limit

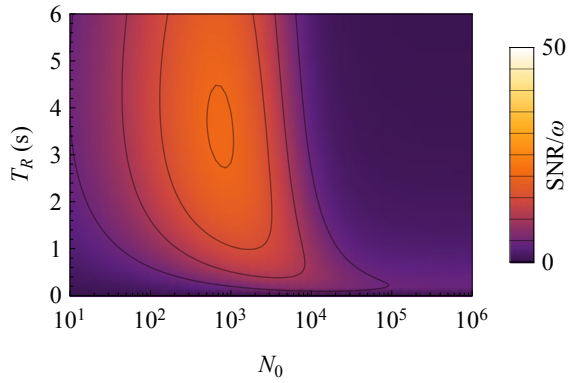

Figure 4.4: Signal-to-noise ratio (SNR) taking all experimental loss processes into account. Due to the one-body loss, a maximum SNR occurs for $N_0 = 750$ and $T_R = 3.5$ s.

in N_0 above which the performance decreases. This can be understood as follows. Consider a large initial atom number N_0. Initially, the two-body losses in $F = 2$ are dominant and quickly reduce N_b. This process is self-limiting, as lower N_b also reduces the collision rate between $F = 2$ atoms. However, as N_a is still large, the interstate collision rate remains large, and any remaining $F = 2$ atoms will quickly meet one of the many $F = 1$ atoms, completely depleting N_b. As the only remaining atoms are in $F = 1$, there is no interferometric contrast left and the SNR goes to 0. It is thus the combination of asymmetric losses, which initially break the symmetry, with symmetric losses, which completely deplete one of the two states, that creates an optimum N_0 for each desired T_R.

For longer T_R, we also observe a global optimum of the SNR, for our situation at $N_0 = 750$ and $T_R = 3.5$ s. This limit on T_R is due to the one-body background loss, which has an exponential decay curve which eventually overtakes the linear gain of SNR with T_R.

For very large densities ($N \gtrsim 10^5$), the SNR becomes independent of N_0. In this regime, three-body losses dominate, and the evolutions of N_1 and N_2 are effectively decoupled. Some SNR remains, but increasing N_0 beyond this point gives no further improvement.

Figure 4.5 shows the remaining atom number as function of N_0. For two-body (intra- and interstate, panel b) processes only, the population N_b depletes completely for large N_0, even at short interrogation times, due to the combination of asymmetric and inter-state losses, whereas N_a keeps growing. When three-body losses are also present (panel a), at large N_0 and short T_R, three-body losses dominate over the two-body processes, effectively decoupling N_a and N_b. In this regime, N_a and N_b saturate. For $T_R = 40$ ms, a maximum in N_b appears around $N_0 = 2 \times 10^4$, where the behavior crosses over from two-body to three-body processes.

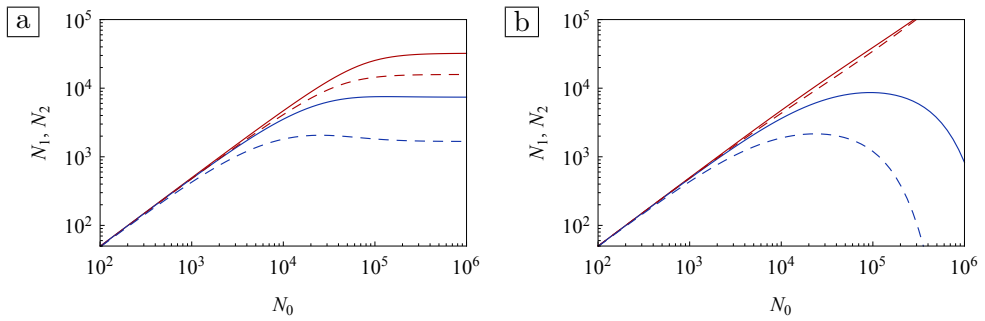

Figure 4.5: Remaining atom number after 10 ms (solid lines) and 40 ms (dashed lines), for N_a (red) and N_b (blue) as function of initial total atom number N_0. a) All loss processes included. b) Only two-body loss $\kappa_{2,2}$ and $\kappa_{2,\mathrm{i}}$ included.

4.2.3 Optimized initial populations

So far we have used equal initial populations $N_a(0) = N_b(0) = N_0/2$ by setting $R_1 = T_1 = 1/\sqrt{2}$. This is the optimal choice in a lossless interferometer as well as in an interferometer with symmetric losses. However, in our experimental situation we have a combination of symmetric and asymmetric loss processes, and the effect of asymmetric losses can be partially compensated by choosing to start with more particles in the state where losses are most severe.

The optimal beam splitter ratio depends on both the initially available N_0 and the desired T_R, in combination with the loss rates. As an example, we numerically optimize the SNR for various atom numbers and fixed $T_R = 1$ s.

Figure 4.6a shows the optimized SNR compared to using equal initial populations. As discussed in the previous section, when using equal populations there is an optimal N_0 for the chosen T_R. By optimizing the initial beam splitter ratio, it is possible to further increase the SNR. Furthermore, there is no more optimum in N_0, and instead the SNR saturates for large initial atom numbers. Figure 4.6b shows the value of $R_1^2 = N_a(0)/N_0$ required for reaching the optimum SNR. Note that for N_0 above the saturation point, almost all atoms are initially in the lossy state N_b, and most of these atoms are lost during the interrogation time.

4.2.4 Squeezed input states

As seen in the previous sections, density-dependent particle losses place a limit on both the useful atom number and interrogation time for high-resolution atom interferometry, when using an uncorrelated (coherent) input state. Higher signal-to-noise ratios may, however, be achieved by using spin-squeezed input states (see section 3.4).

The same loss processes that limit N_0 in a coherent state interferometer may also degrade the usefulness of such entangled input states for interferometry. As described in section 3.5.2, a Schrödinger-cat-like state allows in principle for in-

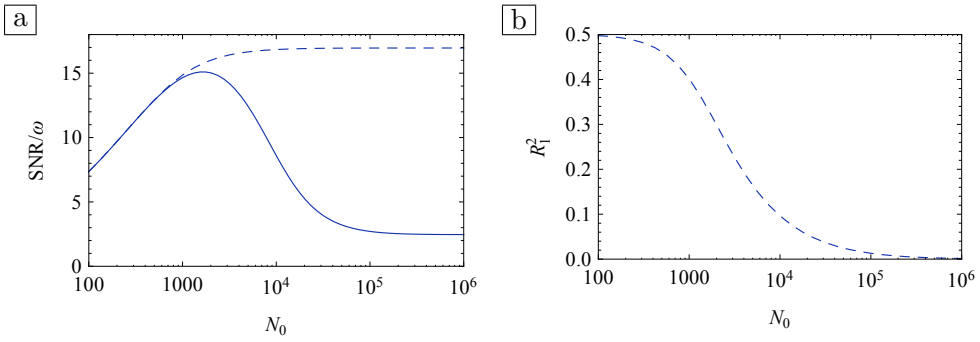

Figure 4.6: Optimized initial populations for $T_R = 1$ s and varying initial total atom number N_0. a) Signal-to-noise ratio for optimized R_1 (dashed line) and for $R_1 = T_1$ (solid line). b) Optimal value of R_1^2 corresponding to the dashed line in panel a.

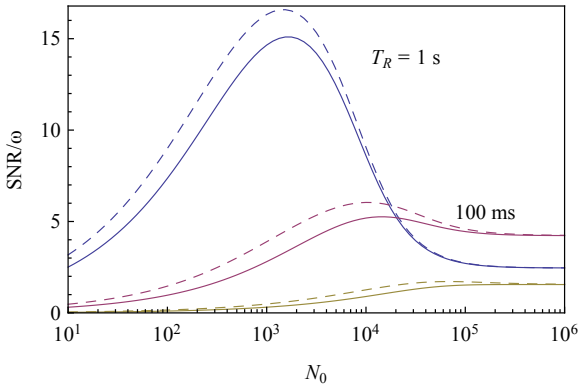

Figure 4.7: Signal-to-noise ratio (SNR) as function of N_0, for different interrogation times $T_R = 1$ s (blue), $T_R = 100$ ms (purple) and $T_R = 10$ ms (yellow). Solid lines correspond to the SQL, dashed lines to an initial state with $\xi_0^2 = -4$ dB of initial squeezing (see text).

terferometry at the Heisenberg limit, but loss of a single particle destroys the useful entanglement. For spin-squeezed states, analytical and numerical models have been established to characterize how particle losses limit the generation of spin squeezing through the one-axis twisting Hamiltonian [62, 110, 111]. For the survival of squeezing in an interferometer, there is no full analytical treatment taking multi-body processes into account. For one-body loss processes and assuming an initial squeezing factor ξ_0^2, the squeezing factor (3.23) evolves in time as [110]

$$\xi^2(t) - 1 = (\xi_0^2 - 1)e^{-\kappa_1 t}. \tag{4.11}$$

We can get a rough estimate of the remaining squeezing by substituting $e^{-\kappa_1 t}$ with the mean remaining fraction of atoms $(N_a(t) + N_b(t))/N_0$ obtained from the solution to equations (4.5).

Figure 4.7 shows the signal-to-noise ratio as function of N_0 for various values

of $t = T_R$, for an SQL limited interferometer and for a squeezed state with initial squeezing $\xi_0^2 = 0.4 = -4$ dB. The squeezing is particularly useful for small N_0, and allows one to obtain the same SNR with fewer atoms. At the optimal N_0 for each time, some squeezing remains in this estimate, and an absolute gain in SNR can be obtained through this route. In the regime where two-body losses have depleted N_2, squeezing gives no more benefit, as expected.

4.3 Field gradients

Density-dependent losses place a strict limit on both N_0 and T_R, but other processes might limit T_R to much shorter values. For example, when measuring a field that provides a differential energy shift V_{mw} between $|1\rangle$ and $|2\rangle$ with high spatial resolution, the field gradient constitutes a state-selective force on the atoms, and T_R must be sufficiently short to avoid demixing of states $|1\rangle$ and $|2\rangle$. Closely related, the gradients of the field across the probe lead to inhomogeneous dephasing, reducing C and imposing a limit on the product $T_R V_{\mathrm{mw}}$.

4.4 Phase coherence in Bose-Einstein condensates

Apart from low losses, long phase coherence is a crucial feature for interferometric measurements with long interrogation time. Coherence times of several seconds have been measured for our interferometer states in thermal ensembles [34, 54], and minute-long coherence was achieved thanks to naturally occurring collisional rephasing [55]. In Bose-Einstein condensates, coherence times of several seconds have also been reported in experiments where interactions were tuned or carefully controlled [112, 113]. Here, I discuss several possible limitations to phase coherence in a small BEC.

One-axis twisting Hamiltonian

One source of phase spreading is exactly the one-axis twisting Hamiltonian H_{int} (equation (3.27)) [114]. While H_{int} can be used to generate spin-squeezed states, in a standard interferometric measurement the anti-squeezed direction is almost perfectly aligned with the interferometer phase, reducing the sensitivity of the interferometer. The phase spreading due to H_{int} leads to an additional phase noise $\sigma_\varphi^2 = 4\,\mathrm{var}(S_{z,0})(\chi t)^2$ after time t, where $\mathrm{var}(S_{z,0})$ is the initial projection noise in $\hat{S}_z$ [60, 89]. For a coherent input state, $\sigma_\varphi^2 = N(\chi t)^2$. This emphasizes the need for control of the rate χ in our experiment: a large χ is needed to create a spin-squeezed state, but during the subsequent interferometric measurement χ should be small not to cause dephasing. Note that, while for fully overlapping components of the BEC χ is negligible, the asymmetry in scattering lengths may lead to demixing of the components even in a state-independent trap, increasing χ. Phase noise of this origin was observed in [112].

Atom number fluctuations

In this thesis, we usually ignore the difference in mean-field energy shifts between $|1\rangle$ and $|2\rangle$, treating it as a constant offset. However, when the number of particles N fluctuates, the mean-field shift also fluctuates and induces an additional phase spreading of [115]

$$\sigma_\varphi^2 = \frac{1}{\hbar^2}\left(\frac{d\mu}{dN}\right)^2 \sigma_N^2 t^2, \tag{4.12}$$

where σ_N is the preparation noise in N and μ is the chemical potential. However, if N can be detected with a precision better than σ_N, this phase noise can be corrected for in each shot of the experiment independently, at least down to the detection noise limit [106]. We use such a correction in our experiments, as described in section 6.9.1.

Finite temperature

For a realistic BEC a finite temperature T has to be taken into account. For a single-component BEC with homogeneous density the phase-spreading due to finite temperature has been theoretically studied in references [115,116]. A phase spreading scaling as $\sigma_\varphi^2 = At^2$ is predicted. Analytical expressions for A are derived in [116] for low and high temperature regimes,

$$\begin{aligned} A &= \frac{8\pi^4}{15}\frac{a^2\xi_h}{V}\left(\frac{k_BT}{\hbar}\right)^2\left(\frac{k_BT}{\mu}\right)^3, && (k_BT \ll \mu) \\ A &= \frac{12\zeta(3/2)^2}{5\zeta(5/2)}\frac{a^2\lambda_{\mathrm{dB}}}{V}\left(\frac{k_BT}{\hbar}\right)^2, && (k_BT \gg \mu) \end{aligned} \tag{4.13}$$

where a is the scattering length, $\lambda_{\mathrm{dB}} = \sqrt{2\pi\hbar^2/(mk_BT)}$ is the thermal de Broglie wavelength, $\xi_h = \hbar\sqrt{\mu/m}$ the healing length and V the system volume.

Figure 4.8 shows the estimated phase noise due to finite temperature calculated with equations (4.13) for our main experimental trap configuration (see section 5.4) and $N = 1400$. We estimate the volume by setting $V = Ng/\mu$, which holds for a homogeneous BEC, and where $g = 4\pi\hbar^2 a/m$. The transition temperature T_c is calculated with equation (2.1). The behavior between the low and high temperature regimes is shown in figure 7 of reference [116].

Note that these results are obtained for a single-component homogeneous BEC in the thermodynamic limit, and the phase noise might be quantitatively different for a harmonic trap and finite N. However, we take these results as a rough estimate for our system. The predicted phase noise scales with density, and reducing the transverse trap frequency by a factor 2 reduces the phase noise by a factor $\approx 1/3$.

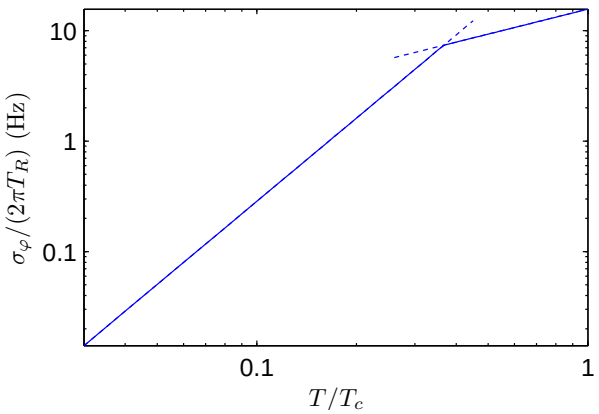

Figure 4.8: Phase noise due to finite temperature estimated for a BEC in our experimental trap configuration, based on reference [116].

4.5 Previous work

In this section I give a brief overview of existing experimental work relevant to high-resolution atom interferometry and magnetic field measurements.

4.5.1 Atom interferometry with high spatial resolution

Magnetic traps on atom chips have a proven track record for scanning probe measurements close to surfaces, as they provide sub-micrometer position control over small BECs. By bringing a BEC close to the surface of an atom chip, electro-magnetic and Casimir-Polder forces have been measured [28–33]. Chip-based interferometric measurements with small probes have been reported in proof-of-principle experiments [34–36], but up to now neither an interferometric scanning probe nor a measurement beyond the SQL have been demonstrated.

4.5.2 Microwave field imaging

High-resolution measurements of microwave near-fields are relevant for scientific applications e.g. in superconducting quantum information processing [117, 118], and for the design of new microwave circuits for use in communication technology [119]. There is currently no standard technique for microwave field imaging. An atomic sensor has the advantage of being intrinsically calibrated and minimally invasive. The electric microwave field was recently detected using Rydberg atoms [120]. The components of the magnetic microwave field were recently imaged in our group using cold thermal atoms on an atom chip, with 8.2 µm resolution and 20 nT sensitivity [121], and using hot atoms in vapor cells with spatial resolution down to 350 µm [122, 123].

Technique	V	σ_B (T/$\sqrt{\text{Hz}}$)	$\sigma_B\sqrt{V}$ (T$\sqrt{\mu\text{m}^3/\text{Hz}}$)
Vapor cell, ent. [23]	11 cm^3	4.2×10^{-16}	1.4×10^{-9}
Vapor cell [124]	0.3 cm^3	5.0×10^{-16}	2.7×10^{-10}
Vapor cell [126]	3.4 mm^3	2.0×10^{-14}	1.2×10^{-9}
Cold atoms, ent. [24]	3.7×10^6 μm^3	5.4×10^{-11}	1.0×10^{-7}
BEC [127]	480 μm^3	8.3×10^{-12}	1.8×10^{-10}
BEC [29]	27 μm^3	1.7×10^{-10}	9.0×10^{-10}
This work [37]	20 μm^3	7.7×10^{-11}	3.5×10^{-10}
NV array [129]	0.016 μm^3	2.0×10^{-8}	2.5×10^{-9}
Single NV [128]	16000 nm^3	5.6×10^{-7}	2.2×10^{-10}

Table 4.1: Comparison of several magnetometry techiques. For several recent experiments, the effective probe or resolution volume V, the magnetic-field sensitivity σ_B, and the volume-normalized magnetic field sensitivity $\sigma_B\sqrt{V}$ are shown. Ent. = uses entanglement between the atoms. The sensitivity obtained in this work is for microwave fields, and is discussed in section 6.8. All other experiments are sensitive to RF or DC magnetic fields.

4.5.3 Static and low-frequency magnetic fields

For static and RF magnetic field measurements, a wide range of technologies exist for a large range of spatial resolutions. Here, I consider atomic or atom-like techniques, which have been realized from centimeter down to nanometer scale. Ultimately, these techniques all rely on the atom-field interaction with characteristic energy $\mu_B B$, and the sensitivity depends mostly on the number of atomic probes and therefore on the total volume of the probe.

Room-temperature vapor cell magnetometers achieve sub-femtotesla sensitivity in the measurement of static and RF fields [124, 125], operating with probe volumes of cubic millimeters [126] to centimeters [23]. Cold-atom sensors sensitive to differential magnetic fields achieve picotesla-scale sensitivity with micrometer-scale probes [29,127]. Nitrogen vacancy (NV) centers in diamond are a promising emerging technology, making excellent sensors at the nanometer-scale [128] up to micrometer-scale [129].

Table 4.1 lists the sensitivities of selected state-of-the-art magnetometers with different technologies and probe volumes. To get a volume-independent comparison, we assume projection noise scaling of the sensitivity and constant probe density, such that the sensitivity scales a volume$^{-1/2}$. Note that such a volume scaling might not be realistic experimentally; for example in vapor cells atom-wall collisions become more significant at smaller volume, whereas cold atom techniques are difficult to scale to large volume. However, the best volume-normalized sensitivity achieved is remarkably similar over the full range of probe volumes from cm-scale to nm-scale magnetometers, owing to the same underlying atom-field interaction.

For practical applications, other factors than sensitivity and spatial resolu-

tion may play a decisive role, such as whether the sensor is sensitive to RF or DC fields, and whether it provides absolute or differential measurements. Finally, considerations on energy consumption, cost and size of the apparatus are important.

5

Experimental setup

The experiments described in this thesis have been performed with ^{87}Rb atoms on a multi-layer atom chip. The experimental setup has been previously used to demonstrate coherent evolution in state-dependent microwave potentials [36], generate spin-squeezed states [12] and image microwave fields [121]. Different parts of our experimental setup and techniques have been described in these references, and in PhD theses [51, 60, 130].

After the aforementioned experiments, and as part of this PhD project, we have moved the experiment from it's original location in the lab of T. W. Hänsch in Munich to our new labs in Basel. As part of the move, and in the years following, various parts of the experiment have been upgraded, replaced, modified or added in a continuing quest to achieve a low-noise environment for the atoms. In this chapter, I present the experimental setup, focusing on those parts that have changed since previous publications. Key elements of the current setup have also been described in reference [37].

5.1 Overview

Figure 5.1 shows an overview of our experimental setup. At the heart of the setup is the science chamber, a glass cell with a volume of $(3\ \mathrm{cm})^3$. The top wall is formed by our atom chip, which is glued to the cell with ultra-high vacuum (UHV) compatible glue (Epo-Tek 353ND). The glue attaches to the AlN base chip and its lead wires, realizing integrated electrical feed-through for both the direct (DC) and microwave (MW) chip wire currents. This results in a compact vacuum chamber.

On the bottom of the cell, a glass-to-metal adapter is attached, which connects via a six-way cross to a 40 l/s ion pump, a Ti-sublimation pump, an ion pressure gauge, and electrical feed-throughs for the Rb dispensers. The ion pump operates continuously, maintaining a pressure of a few times 10^{-10} mbar, whereas the Ti-sublimation pump is activated periodically (typically once every 1-2 months) when the pressure approaches 10^{-9} mbar.

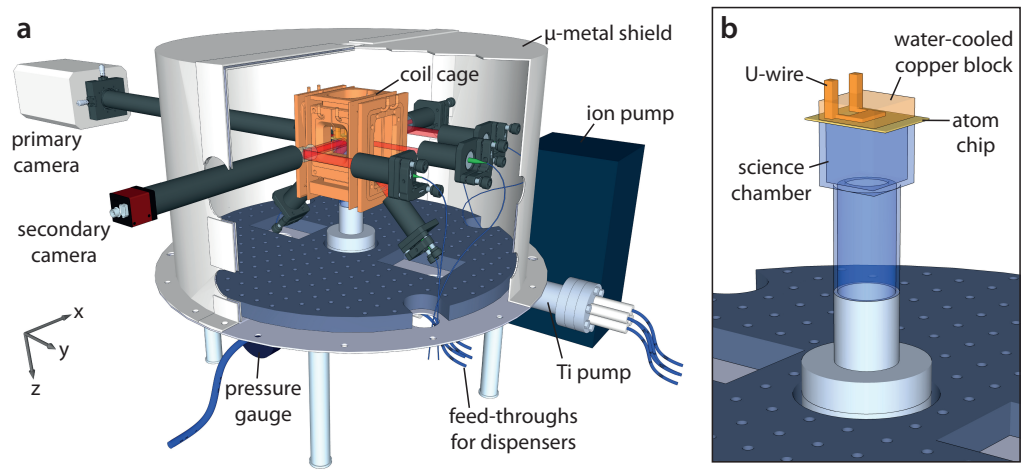

Figure 5.1: Overview of the experimental setup. a) Schematic view of the vacuum system, coil cage, μ-metal shield, laser beams and imaging cameras. b) Detailed view of the science chamber showing the atom chip with copper cooling block and U-wire used for the magneto-optical trap.

As Rb source we use one of three dispensers, installed below the science chamber in the glass-to-metal transition. So far all experiments have used either one of two SAES Getters dispensers[1], operated continuously at a current of 3.8 - 4.1 A. The third dispenser[2] has not been used since the initial vacuum bake-out. It is interesting to note that the vacuum pressure measured by the gauge lowers when the Rb dispensers are running in steady-state, suggesting the released Rb is effectively functioning as a getter material. All dispensers contain the natural isotope mixture of rubidium.

The science chamber is surrounded by a water-cooled coil cage, consisting of a three sets of Helmholtz coils providing approximately homogeneous bias fields in all three directions. The coils generate a field 6.1 G/A in x-direction and 1.7 G/A in z-direction. In the y-direction, the coils have two independent windings, where we use one winding for strong fields (4.3 G/A) and the second winding for weaker fields (1.7 G/A). To the backside (air side) of the atom chip a water-cooled copper block is attached, with an integrated U-shaped wire which is used to create a strong magnetic quadrupole field during the magneto-optical trapping phase. The water-cooled elements are connected in series to a chiller which stabilizes the water temperature to 19° C.

Surrounding the vacuum chamber and coil cage are fiber output couplers for all required laser beams, imaging optics for imaging along both the y- and x-direction, a microwave horn and radio frequency antenna. The whole assembly is enclosed in a μ-metal shield to reduce the effect of external magnetic field noise.

[1] SAES Getters RB/NF/3,4/12FT10+10
[2] Alvatec AS-RbIn-5-F

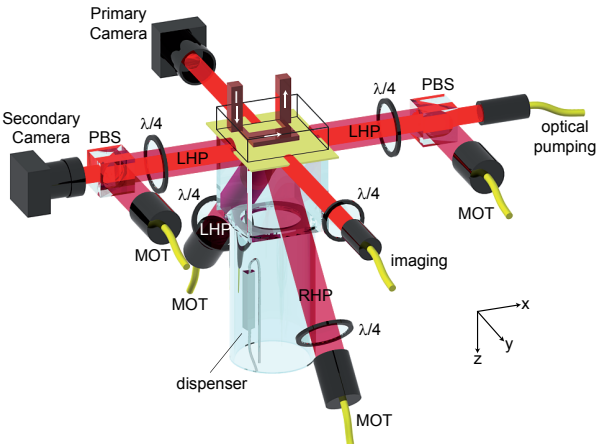

Figure 5.2: Optics setup surrounding the science chamber, consisting of four MOT beams for laser cooling, a primary imaging beam along $-y$, and an optical pumping and secondary imaging beam along $-x$. Indicated are polarizing beam splitters (PBS), quarter-wave plates ($\lambda/4$), and right-hand and left-hand circular polarization of the MOT cooling beams (RHP and LHP, respectively). Figure adapted from [51].

5.1.1 Optics setup

Figure 5.2 shows the optics configuration surrounding the science chamber. All laser light is brought to the setup through optical fibers, and the resulting optics setup fits inside the μ-metal shield.

For laser cooling we employ a mirror-magneto optical trap (MOT), using only four beams compared to the traditional six-beam free-space setup [76, 131]. Two diagonal beams, pointing along $z \pm y$, are reflected off the chip surface to provide cooling in both the y and z-direction. Two horizontal beams along $\pm x$ provide cooling in the x-direction. MOT repumping light is overlapped with the diagonal beams. The MOT beams are circularly polarized, and form a MOT in combination with a magnetic quadrupole field generated by the U-shaped wire (current direction indicated in figure 5.2). The MOT operation is described in detail in reference [51].

Optical pumping light (see section 5.6) is overlapped with the horizontal MOT beams, and has right-hand circular polarization. The same fiber also carries probe light to the secondary imaging camera. The primary imaging light has a dedicated fiber along $-y$, and is also right-hand circularly polarized.

5.2 Atom chip

The design and fabrication of our atom chip is described in detail in [130]. Figure 5.3 shows a photograph of the multilayer atom chip. It consists of a base chip providing mechanical structure, vacuum feed-throughs and large DC wires;

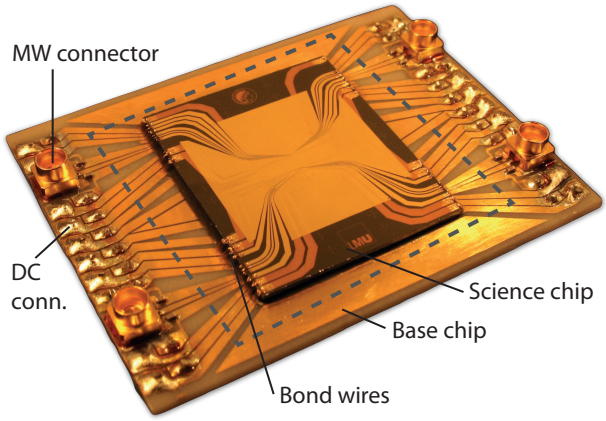

Figure 5.3: Photograph of the chip package. Outer dimensions: 38×50 mm. The gray dashed line indicates the approximate position where the glass cell is glued.

a science chip providing two layers of gold wires including microwave waveguides on the top layer; and a spacer chip between the two. For reference, detailed drawings of the chip wire structures are included in appendix A.

5.2.1 Base chip

The base chip is an 800 µm thick AlN ceramic substrate (38×50 mm) with a 12 µm thick patterned gold layer formed by electroplating. The pattern consists of a double "H" structure (see appendix A), part of which we use to generate a quadrupole field for a compressed magneto-optical trap, and lead wires for microwave and DC currents to the science chip.

For microwave currents, mini-SMP connectors are soldered to the base chip, facing down in the final experiment. DC connections are provided through standard 2.54 mm-pitched pin headers on the back (upward facing) side of the chip, which connect to ribbon cables. The ground lines of each coplanar waveguide are coupled to the microwave connectors via on-chip capacitors and directly connected to a DC pin. These on-chip bias tees allow both MW and DC currents to be used on the same wire (the MW signal wires also carry DC currents via external bias tees).

5.2.2 Science chip

Both the science chip and spacer chip consist of a 525 µm thick high-resistivity Si substrate. The science chip has two layers of gold wire structures. The lower gold layer is electroplated and has a thickness of 5 µm. It is structured with several interconnected wires, which can be used for dimple, Z-wire and U-wire trap configurations.

The lower gold layer is covered by a 6 µm thick layer of polyimide, which

provides electrical insulation. The polyimide is applied in three layers, which helps to planarize (smoothen) height variations in the chip surface due to the underlying wire structures.

The top layer is a 1 µm evaporated gold layer, structured with a lift-off technique. It contains two sets of wire structures, which we refer to as the five-wire structure and the six-wire structure. The five-wire structure is used in this thesis, and it features a MW co-planar wave guide (3 wires), surrounded by two auxiliary DC wires (not used in this thesis). The wires are 6 µm wide and spaced by 3 µm gaps. The six-wire structure consists of 2 MW wave guides, each with in-line terminators (shorts between the signal and ground wires). It has 2.5 µm wide wires spaced by 2 µm gaps.

Apart from the wire structures, the top gold layer also covers most of the chip surface and acts as a mirror for the magneto-optical trapping stage of the experiment.

5.3 Magnetic field simulation

To design different current configurations trapping atoms, we simulate both the static and microwave-dressed potential observed by the atoms. The simulation was originally developed in reference [51], and allows for a combination of models for both the static field and microwave fields.

In this thesis, the static magnetic field around the center of the chip is simulated by modeling the central part of the atom chip wires as rectangular planar conductors in the x, y-plane carrying homogeneous current densities.

The microwave magnetic field is calculated quasi-statically with the same model, by assuming a microwave current in the central conductor of the co-planar waveguide and return currents in the two ground conductors. In previous measurements of the microwave magnetic field [121], asymmetry in the field distribution was found which we attribute to coupling of microwave currents into neighboring structures on the chip. We take this asymmetry into account by choosing an asymmetric distribution of return currents, and by setting small currents in the outer two conductors of the five-wire structure. The relative currents are optimized to reproduce the distribution measured in [121] with good accuracy.

The absolute strength of the microwave field is calibrated in two ways. A first calibration is obtained by measuring the microwave transmission loss of 7.4 dB in the chip assembly (including the microwave connectors). We then estimate the current amplitude in the central wire by assuming equal losses before and after the CPW center. Finally, to verify the calibration we compare the simulated differential microwave potential to the scanning-probe interferometric measurements described in 6.7, and find excellent agreement.

The atomic potential is calculated for all microwave-dressed levels of the hyperfine ground state by numerically diagonalizing the Hamiltonian (2.10) at each point in space. In the experiment, we adiabatically switch the microwave dressing

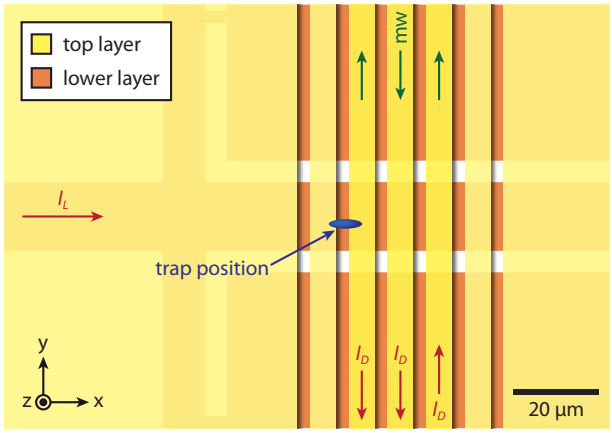

Figure 5.4: Schematic of the central region of the science chip, showing the wire configuration used for trapping.

on and off, and we assume the atoms stay in the states which have the largest component of their initial un-dressed states $|1\rangle$ and $|2\rangle$, respectively. Finally, the gravitational potential $U_{\text{grav}} = -mgz$ with $g = 9.81$ m/s^2 is taken into account. The potential minima are found by a simplex minimization algorithm, and the trap frequencies are estimated by numerically calculating the curvature around the minimum.

5.4 Static magnetic trap configuration

Our main experiments are performed in a dimple trap (see section 2.5.1), created with the five-wire structure of the science chip. Figure 5.4 shows a schematic of the wire configuration around the center of the five-wire structure. Transverse confinement comes from a wire in the lower gold layer carrying $I_L = 130$ mA in x-direction plus a static field $B_y = 5.2$ G. Longitudinal confinement is provided by three parallel dimple wires in the top gold layer carrying $I_D = 2$ mA each. Two dimple wires carry current in $-y$-direction, and the third in $+y$-direction. The total dimple current is thus 2 mA in $-y$-direction, and the asymmetric distribution of dimple currents is needed to realize a trap position x_0 along x that is not directly above the wire crossing. The static field along x is $B_x = 3.2$ G.

The simulated trap minimum is located at $x_0 = -12.6$ µm, $y_0 = -1.7$ µm and $z_0 = 40.3$ µm, where the origin is chosen at the central wire crossing and on the chip surface. The trap is approximately cylindrical and has trap frequencies $\omega_l = 2\pi \times 115$ Hz, $\omega_{\perp,1} = 2\pi \times 529$ Hz, and $\omega_{\perp,2} = 2\pi \times 544$ Hz; approximately along the x, y, and z-directions, respectively.

The size of the BEC determines the spatial resolution of an interferometric measurement. We estimate the cloud size based on an interpolation between the Thomas-Fermi and harmonic oscillator regime [49], where the atomic density

η	x_0 (µm)	y_0 (µm)	z_0 (µm)	B_0 (G)	$\frac{\omega_l}{2\pi}$ (Hz)	$\frac{\omega_{\perp,1}}{2\pi}$ (Hz)	$\frac{\omega_{\perp,2}}{2\pi}$ (Hz)
0.5	-7.8	-0.5	15.5	3.26	112	508	515
0.6	-8.9	-0.7	20.6	3.26	114	515	523
0.7	-9.9	-0.9	25.6	3.25	114	520	529
0.8	-10.9	-1.1	30.5	3.23	114	523	534
0.9	-11.8	-1.4	35.5	3.22	114	526	539
1.0	-12.6	-1.7	40.3	3.20	115	529	544

Table 5.1: Estimated trap parameters for the scanning probe measurements as function of the scanning parameter η. B_0 is the static field in the trap center, aligned approximately with the x-direction.

profile is approximated as a Thomas-Fermi profile (inverted parabola) with radii $R_x = 4.0$ µm and $R_y = R_z = 1.05$ µm for $N = 1400$ atoms. The volume within the Thomas-Fermi radii is 20 µm^3.

5.4.1 Scanning probe

To realize a scanning-probe interferometer, we move the trap to the position where the measurement is to be taken. For this, we define a parameter η, which we vary from $\eta = 1$ (original trap) to $\eta = 0.5$, and scale the trap parameters as

$$\begin{aligned} I_L &\propto \eta^2, \\ I_D &\propto \eta^4, \\ B_y &\propto \eta, \end{aligned} \tag{5.1}$$

while keeping $B_x = 3.2$ G constant. This keeps the trap geometry constant within 10%, and the magnetic field B_0 at the trap center within 50 mG of the "magic" value of 3.23 G (see section 2.3.1). We scan all currents and fields in a 20 ms smooth ramp. Table 5.1 lists the simulated final trap position, static field B_0 and trap frequencies for the values of η used in our experiments, and figure 5.6 shows the trap positions.

5.4.2 Positioning accuracy

The absolute positioning accuracy is relevant for a scanning-probe measurement. Since the wire configuration on the chip is well known, the accuracy of the simulated trap position (with respect to the chip wires) is limited by the accuracy of the wire currents and homogeneous bias fields. We calibrate the wire currents with a Keithley 2000 multimeter, giving an accuracy of 50 µA in I_L and 10 µA in I_D. We calibrate B_x using the atoms themselves: we measure the two-photon detuning δ in a time-domain Ramsey measurement (see section 3.3) as function of B_x, and extract the value of B_x where B_0 is equal to the magic field by comparing to equation (2.9). In combination with the trap simulation, this gives a

calibration of B_x with an accuracy of 10 mG. The magnetic fields B_y and B_z were calibrated with a flux gate magnetometer before the coil cage was installed around the science chamber. We estimate the accuracy of B_x and B_y to be 100 mG.

Using these uncertainties in the trap simulation, we estimate the total position uncertainty to be 0.5 µm in x_0 and 1 µm in y_0 and z_0. The calibration accuracy in y_0 and z_0 is dominated by the uncertainty in B_y and B_z. If better accuracy is desired, these fields could potentially be calibrated using the atoms in different trap configurations. The uncertainty of x_0 is affected by the accuracy of B_y as well as I_D, the latter of which could be improved with a better current meter.

The shot-to-shot reproducibility of the currents and fields is much better than the absolute accuracy[3]. Therefore, the shot-to-shot fluctuations of the trap position are much smaller than the cloud size and do not affect the spatial resolution.

With the simple parameter scaling scheme we use here, the trap position can be varied approximately along a line towards the central wire crossing. It has the advantage that it is easy to implement experimentally. However, a three-dimensional scanning probe could be realized with a more complex parametrization, or by numerical search with the trap simulation. By rotating the static field, the trap can be translated in the y, z-plane; the current distribution in the dimple wires can be used translate the trap along x. It is also worth noting that the trap frequencies do not necessarily have to remain constant in a scanning-probe measurement, at the expense of an inhomogeneous spatial resolution.

5.5 State-selective potential

The same wires that carry the dimple currents I_D also form a co-planar waveguide for microwave signals. The evanescent field of the wave guide generates a state-selective potential V_{mw} for the atoms. We simulate the field distribution as described in section 5.3. In the experiments described in chapter 6, we use microwaves blue-detuned by $\Delta_0 = 12$ MHz with respect to the $|1,0\rangle \leftrightarrow |2,0\rangle$ transition, creating a differential level shift between $|1\rangle$ and $|2\rangle$ of $-(71, 46, 39)$ kHz/G^2 for the $(\pi, \sigma^+, \sigma^-)$-components of the mw magnetic field amplitude.

Figure 5.5 shows the energy level diagram of the ground state hyperfine manifolds in the presence of the microwave field, calculated for the field at the static trap minimum with a microwave current of $I_{\mathrm{mw}} = 15$ mA. The level shifts are exaggerated by a factor 2×10^4 for clarity. With $I_{\mathrm{mw}} = 15$ mA, the minima of the total potential of $|1\rangle$ and $|2\rangle$ are separated by ≈ 140 nm. We use a smooth ramp of 350 µs to turn on and off the microwave power, to ensure the atoms adiabatically follow the dressed states.

[3] Stability estimates of our current sources and generated static magnetic fields are listed in table B.2. External magnetic field fluctuations are reduced to ≈ 15 µG (long-term drifts over several days) by the µ-metal shield surrounding the experiment, and negligible compared to fluctuations in the current sources.

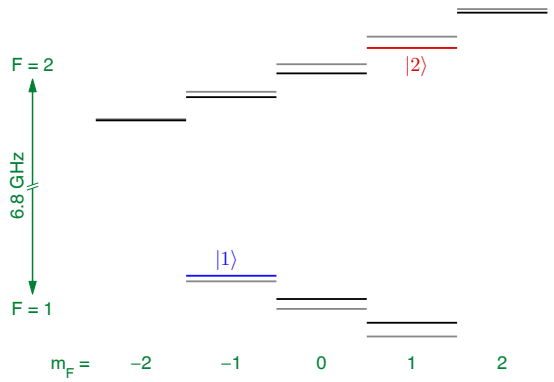

Figure 5.5: Energy level diagram with microwave-dressed potentials. Gray lines show the ground state levels in a static magnetic field of 3.2 G. Black, red and blue lines show the levels shifted by a microwave blue-detuned by $\Delta_0 = 12$ MHz. The microwave level shifts have been exaggerated by a factor 2×10^4.

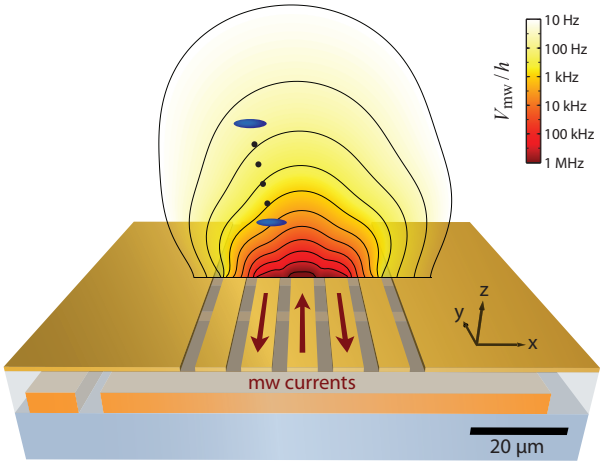

Figure 5.6: Microwave potential with $I_{\mathrm{mw}} \approx 5$ mA. The position and shape of the BEC is shown to scale in blue for $\eta = 1$ (top) and $\eta = 0.5$ (bottom), and black dots indicate intermediate trap positions.

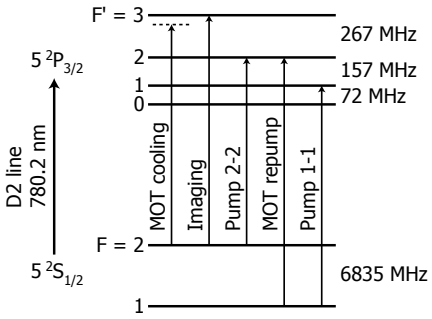

Figure 5.7: Level scheme of the ^{87}Rb D_2 line [52] and laser frequencies used in our experiment. Figure adapted from [51].

In section 6.7 we use the atoms as a scanning probe to measure the microwave potential. In that measurement, we use a microwave current of $I_{\mathrm{mw}} \approx 5$ mA. Figure 5.6 shows the calculated V_{mw}, as well as the positions listed in table 5.1 where the scanning probe measurement is performed.

5.6 Laser system

Our laser system generates laser light at several frequencies required for laser cooling, optical pumping and imaging of the atoms, as shown in figure 5.7. All laser frequencies are close to resonance with the ^{87}Rb D_2 line at a wavelength of 780 nm. In this section, I briefly discuss the operation of the laser system; for a detailed discussion see references [51, 60].

Figure 5.8 shows a schematic of the main components of our laser system. Components such as beam shaping optics, wave plates and additional mirrors have been omitted for clarity. All outputs of the laser system are coupled to single-mode polarization maintaining fibers, which bring the light to the vacuum chamber (see figure 5.2).

The laser system consists of three diode lasers. The *master* laser is grating-stabilized [132], and has a typical output power of 20 mW. It is locked via saturation spectroscopy [133] to the cross-over peak between the $F = 2 \leftrightarrow F' = (2, 3)$ transitions. The output light is frequency-shifted by an acousto-optic modulator (AOM) in double-pass configuration and injected into the *slave* laser, which acts as an amplifier. By changing the double-pass AOM frequency during the experiment we have control over the frequency of the slave laser without significantly changing the output power and beam pointing.

The slave laser generates ≈ 90 mW of light, most of which is used for the *MOT cooling* light. The cooling light is frequency shifted by an AOM in single pass configuration, which runs at fixed frequency but is used for fast switching of the power. A mechanical shutter is available to completely turn off the power. The cooling light is then split into four parts, carried by separate fibers to form

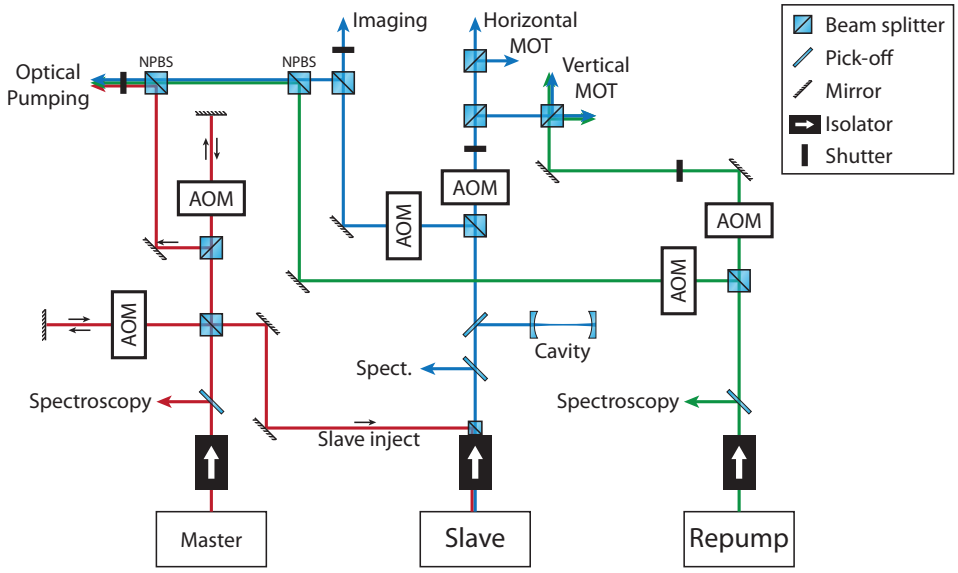

Figure 5.8: Overview of the laser system, excluding wave plates and several other components. The master and repump laser frequency are independently locked to Rb saturation spectroscopy. The slave laser is injection-locked to the frequency-shifted output from the master laser. A confocal cavity and Rb spectroscopy setup are used to diagnose the injection locking. All output beams are coupled to polarization maintaining single-mode optical fibers. NPBS = non-polarizing beam splitter.

two horizontal (along $\pm x$) and two diagonal (along $z \pm y$) MOT beams. The diagonal MOT beams each carry ≈ 10 mW, and the horizontal beams $\approx$ 4mW.

The third laser is the *repump* laser, which is independently grating-stabilized and locked to the $F = 1 \leftrightarrow F' = (1, 2)$ crossover resonance. It produces ≈ 50 mW of light. Part of it forms the *MOT repump* light, after an AOM for intensity control and mechanical shutter. The MOT repump light is overlapped with the diagonal MOT beams and carried through the same fibers.

The *imaging* light is taken from the slave laser, with a separate mechanical shutter and AOM for intensity control. The primary imaging beam is carried by a separate fiber and output along the y-direction. It can produce up to a few mW of probe light, but the probe intensity is chosen for best signal-to-noise imaging (see section 5.9).

Finally, the *optical pumping* fiber carries three different frequencies: the *pump 2-2* light, taken directly from the master laser via a double-pass AOM; the *pump 1-1* light, derived from the repump laser with a single-pass AOM; and some imaging light for the secondary imaging axis taken after the imaging AOM. The three beams are overlapped on non-polarizing beam splitters to have identical polarization, and they share a single mechanical shutter.

5.7 Current sources

Low noise and high stability current sources are essential for our experiment. Here, I briefly mention the most important current sources used in the experiment; for a detailed description see references [60, 130, 134]. Magnetic field noise and current noise will be discussed in section 6.10.

For the homogeneous bias fields we use home-built bi-polar current sources delivering up to ±5 A (the design is described in reference [134]). The additional strong-field winding for B_y is driven by a FUG NLN 350M-20 unipolar 15 A source. After the BEC is created, this current source is disconnected with a transistor (IGBT) switch to reduce magnetic field noise.

For the chip wire current I_L we use a similar home-built current source as for the bias fields, but configured to deliver ±3 A. The dimple currents I_D are generated by HighFinesse BCS 002/10 current sources, delivering up to ±20 mA each. These are designed to operate on battery power, but we use a linearly regulated power supply instead to enable long measurement runs.

5.8 Microwave and RF system

In our experiments we rely on microwave (MW) and radio frequency (RF) fields to coherently manipulate the internal state of the atoms, and both the phase coherence and amplitude stability of these fields are important. Since the initial spin-squeezing measurements [12], several upgrades to the MW and RF system have been made in order to improve both short-term and long-term stability. Here I describe the current state of the system, and in addition make a few notes about the components that were used for the experiments described in chapter 6.

We drive two-photon Rabi transitions with a microwave field (∼6.8 GHz) and a radio frequency field (∼1.7 MHz). Both fields are generated off-chip, intended to minimize spatial inhomogeneity of the field strength. The microwave field is emitted from a "horn" formed by a right-angle coax-to-waveguide transition. The RF field is emitted from a home-built square coil of 9 windings and 3 cm side length, connected in series with a 10 Ω resistor. The RF coil is placed around the probe beam used for absorption imaging. Even though the fields are created far from the chip, we experience gradients in the field strength at the position of the atoms in both the microwave and RF field (see section 6.1). These gradients are likely caused by coupling of the field to the chip wire structures.

In addition to these off-chip fields, we use the on-chip co-planar waveguides for the state-selective potential, as described in section 5.5. In this section, I describe the microwave and RF system for both the off-chip and on-chip fields.

Figure 5.9 shows an overview of the combined microwave and radio frequency system. The system consists of a reference clock, power-stabilized microwave setups for both the on-chip and off-chip microwaves, and an RF setup.

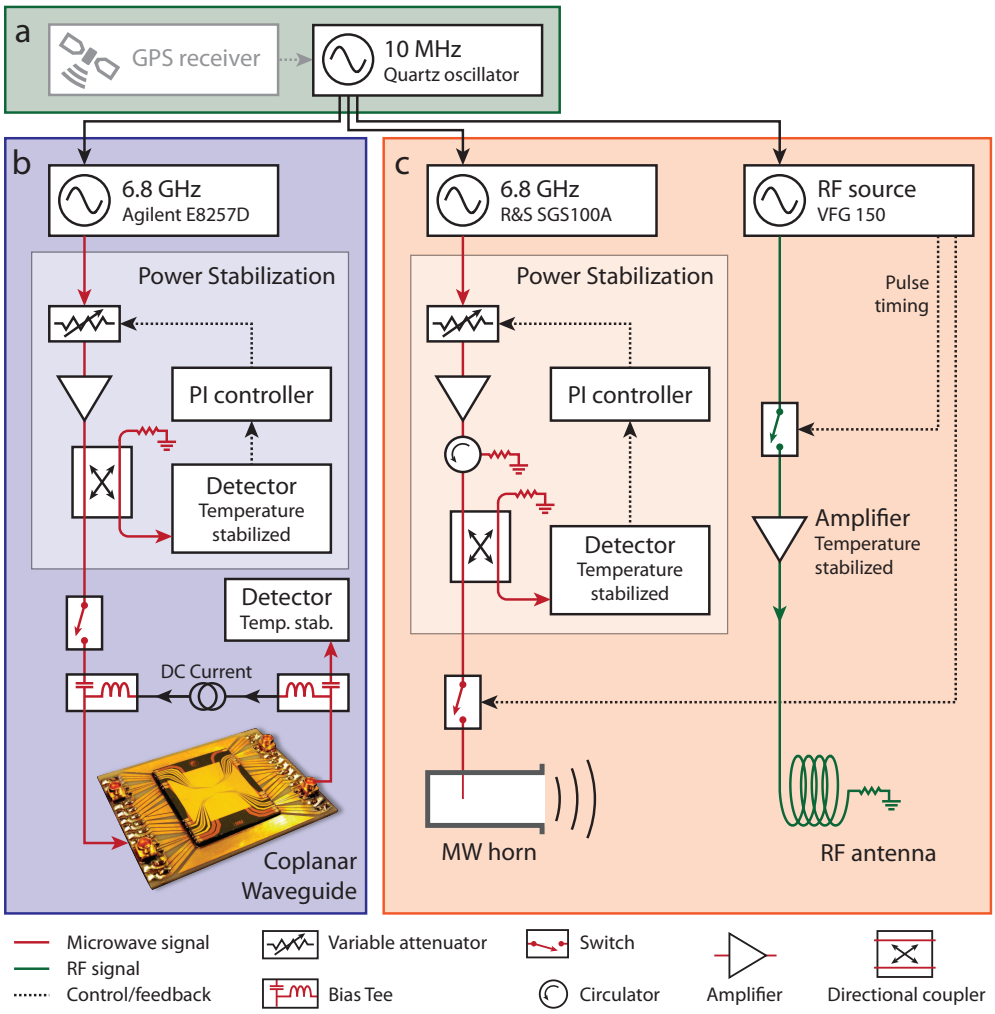

Figure 5.9: Schematic of the microwave and radio frequency electronics showing a) reference oscillator, b) on-chip microwave signal path and c) microwave and rf signal path for driving Rabi transitions.

5.8.1 Reference clock

To achieve good phase coherence, all signals are referenced from a high-quality BVA-mounted 10 MHz quartz oscillator from Quartzlock[4]. The quartz oscillator provides very good short-term stability, and can optionally be locked to time signals obtained from GPS satellites for improved long-term stability[5].

To characterize the performance of the different reference oscillators available in our lab, we perform Allan deviation measurements. The Allan deviation $\sigma_y(\tau)$ is a measure for the root-mean-square (rms) fractional frequency[6] stability between two measurements taken a time τ apart [135]. It is important to note that such a measurement provides only a comparison between two oscillators, since a second reference clock is always needed to measure frequency. Thus, the measured Allan deviation can be interpreted as a worst-case limit to the performance of both devices.

Figure 5.10 shows two Allan deviation measurements of the reference clock. One measurement is performed in our lab and compares the Quartzlock reference clock to the internal reference of our Agilent E8257D. The second measurement was performed by Quartzlock during development and testing of our device, and compares to a hydrogen maser. During this measurement, the phase-locked-loop (PLL) that locks the quartz oscillator to GPS was still being configured, and used different parameters from the final product. For short integration times ($\tau \lesssim 1$ s) both measurements are roughly consistent, indicating a short-term stability of $\approx 5\times10^{-13}$ Hz$^{-1/2}$. For long τ, both measurements scale as $\sigma_y(\tau) \propto \tau$, which indicates frequency drifts dominate on those time scales. The measurement performed in our lab shows slightly better long-time performance, possibly due to different PLL parameters. On intermediate time scales, the measurement in our lab may be limited by the Agilent clock.

5.8.2 On-chip microwave system

The on-chip microwave signal chain is shown in part b of figure 5.9. We use an Agilent E8257D signal generator[7] as signal source. To improve the power stability of the signal, we use a power stabilization feedback circuit, home-built in our lab by Roman Schmied. The feedback circuit also allows complex ramps and pulse shapes to be programmed by modulating the set point.

The feedback loop consists of a voltage variable attenuator[8], a low-noise am-

[4] Quartzlock E8000-BVA. The BVA option was custom made for our experiment.

[5] In our experiments GPS locking has not yet been used, because we were unable to obtain a stable GPS lock. This might be due to a problem in the GPS receiver, pre-amplifier or antenna.

[6] The fractional frequency is the time-dependent frequency error normalized by the nominal (or average) frequency of the oscillator.

[7] With UNX low phase noise option

[8] Pulsar AAT-25-479/251040, maximum attenuation 80 dB.

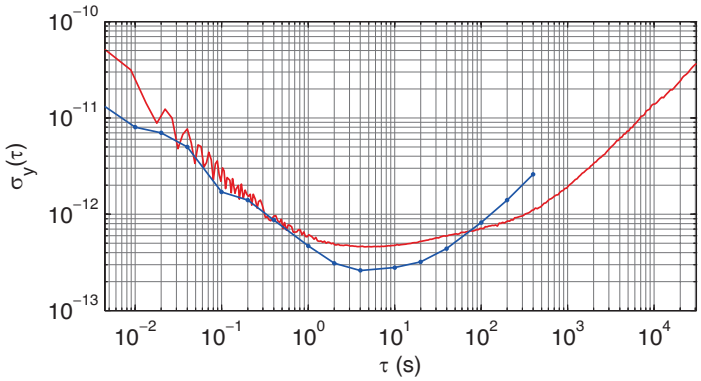

Figure 5.10: Allan deviation $\sigma_y(\tau)$ measured for our Quartzlock E8000-BVA reference clock. Red line: measured in our lab by comparing with the Agilent E8257D internal reference. Measured with a Zurich Instruments HF2LI lock-in amplifier. Blue circles: measured by Quartzlock during product development by comparing our unit with a hydrogen maser. The Quartzlock measurement does not represent the final PLL tuning parameters.

plifier[9], and a directional coupler[10] which splits off a small amount of power a broadband power detector[11]. Many microwave components have strongly temperature dependent transmission properties. To counter-act the effect of temperature drifts in the lab, the detector is mounted in a temperature-stabilized copper block. The detector output is fed to a home-built PI controller, whose output is fed back to the attenuator. The PI controller uses a current-to-voltage pre-amplifier based on an OPA111 low-noise operational amplifier (opamp). The feedback loop has a bandwidth of ≈ 150 kHz. The set point for the PI controller is provided by an analog channel from the experiment control, filtered by a 50 kHz low pass filter. We measure the relative power stability of the on-chip microwave system to be $\lesssim 10^{-4}$. The system can deliver up to ≈ 300 mW of microwave power to the chip, but we typically adjust the gain of the feedback loop to reduce the maximum power.

Although the feedback circuit can provide enough attenuation to effectively switch off the microwaves when driven with a negative set-point voltage, doing so drives the circuit into a saturated state from which it recovers slowly and not in a well-defined way, which is undesirable. Instead, an absorptive switch (Miteq N147BDM2, ≈ 95 dBm attenuation) is placed after the feedback loop. Finally, a bias tee (UMCC BT-5000-HS) is used to add a DC current to the microwave signal wire, and the combined signal is fed to the on-chip co-planar waveguide (CPW). The return signal from the chip passes through a second bias tee to separate the DC current, and the final microwave signal is terminated by a second

[9] Microsemi AML218P3203, 2–18 GHz, 32 dB gain, 30 dBm output (IP3), noise figure 4 dB.
[10] Pulsar CS20-10-435/1, 20 dB coupling
[11] Agilent 8471E

temperature-stabilized detector. This detector signal is normally not monitored, but can be used to analyze the power stability. It is also an important tool to verify the shape and reproducibility of microwave power ramps programmed via the experiment control[12].

5.8.3 Off-chip microwave and RF system

Part c of figure 5.9 shows the signal chain for the two-photon drive. The microwave signal is sourced from a Rohde & Schwarz SGS100A signal generator[13]. The signal is then fed to a similar power stabilization loop as described in the previous paragraph[14]. The feedback loop uses an SRS SIM960 analog PID controller plus an OPA111-based home-built pre-amplifier. The microwave amplifier is followed by a circulator to protect the output port from reflected power. Finally, a switch is placed before feeding the signal to the microwave horn. In our current experiments, we run the PID loop with a constant set point, and only use the switch for gated pulses.

The radio frequency signal is generated by a VFG 150 signal generator. It generates sine waves using direct digital synthesis (DDS) at a sample rate of 200 MHz, and can switch frequency, amplitude and phase almost instantaneously. After an RF switch (MiniCircuits ZASWA-2-50DR), the RF signal is fed to a power amplifier[15] and subsequently to the RF coil. The RF coil as load in combination with the VFG's AC-coupled output circuit causes potential feedback problems, where the circuit starts to oscillate at full amplifier power. We avoid these problems by carefully choosing cable lengths and using a 70 MHz low-pass filter between the VFG and the RF amplifier.

In addition to the RF output, the VFG has four binary (TTL) outputs, which can be switched in sync with the RF signal with a time resolution of 5 ns. We use these outputs to drive both the switch to the microwave horn and the RF switch. The external RF switch is needed because the VFG's RF output couples to electronic noise present in the lab, even when the VFG output amplitude is set to 0. This electronic noise originates mostly from switching-mode power supplies, whose kHz-range switches can have harmonics in the MHz range which couple to ground. In several cases, we noticed direct coupling to the spin-flip transitions around 2.2 MHz in our atoms. Although most switching-mode power supplies in our experiment have been replaced by linear supplies, the RF switch helps to isolate from residual noise sources during most of the experimental sequence.

[12] Pulse shape and reproducibility suffer if the changes are too fast for the feedback loop to follow, but also if the feedback loop has to come out of saturation. We typically use a 2 ms "warm-up" time at low power and with closed switch to allow the PI controller to reach a well-defined state.

[13] During most measurements described in chapter 6, a refurbished HP 8340B was used as microwave source. It had similar phase noise characteristics as the Rohde & Schwarz, but broke down after several months of continuous operation.

[14] The power stabilization loop was added after the measurements in chapter 6.

[15] MiniCircuits LZY-22+, 100 kHz – 200 MHz, 43 dB gain, 30 W output power

5.9 Absorption imaging

The precise and well-calibrated determination of the number of atoms N_1 and N_2 in output states $|1\rangle$ and $|2\rangle$, respectively, is essential to our measurements. We measure the atomic density distribution using absorption imaging.

In standard absorption imaging, laser light with intensity I resonant to a cycling transition passes through the atomic distribution. The atoms cast a shadow, and the resulting intensity is imaged on a camera and recorded as the absorption image A. A second reference image R is taken without atoms, to measure the intensity profile of the probe beam[16]. The two-dimensional atomic density $n_{2\mathrm{D}}$ can then be reconstructed on a pixel-by-pixel basis as [136, 137]

$$n_{2\mathrm{D}} = -\frac{\alpha}{\sigma_0}\ln\left(\frac{A}{R}\right) + \frac{\alpha}{\sigma_0}s\left(1-\frac{A}{R}\right), \tag{5.2}$$

where $\sigma_0 = 3\lambda^2/2\pi$ is the resonant absorption cross section of the imaging transition at wavelength λ, and the dimensionless parameter $\alpha \geq 1$ takes errors in the probe polarization or frequency into account. The second term in equation (5.2) takes the effect of saturation of the imaging transition into account, with $s = I/\alpha I_s$ is the effective saturation parameter and $I_s = 1.67\ \mathrm{mW/cm^2}$ the saturation intensity of the transition. We calculate s on a pixel-by-pixel basis from the reference image.

5.9.1 Primary imaging setup

To detect *both* output states after each run of the experiment, we use a modified version of absorption imaging. First, we briefly expose the atoms to a probe laser, tuned to resonance with the $F = 2 \rightarrow F' = 3$ transition, circularly polarized to drive the σ^+ cycling transition. After a delay of 1.5 ms, in which the $F = 2$ atoms fly out of the depth of field due to photon recoil from the probe pulse, we optically pump atoms from $F = 1$ to $F = 2$, and record a second absorption image containing only signal from atoms originally in $F = 1$. Finally, a reference image with no atoms is recorded.

Figure 5.11 shows our primary imaging setup. The probe light is emitted from an optical fiber along the $-y$-axis. A two-lens telescope collimates the probe beam, while at the same time imaging an aperture onto the position of the atoms (diameter ≈ 0.6 mm). The aperture makes sure the probe light does not reach the chip surface, reducing diffraction effects and creating a fairly homogeneous probe light field at the position of the atoms. Residual diffraction patterns from the aperture remain, with peak-to-peak intensity variations up to 20%.

The imaging objective is formed by a $4f$-telescope. The primary objective lens is a laser doublet (Melles Griot 06 LAI 005/076) with a focal length of 40 mm and

[16] Typically once per day, an additional *dark* image is taken, which is subtracted from both A and R. It takes residual background light and in particular a constant offset count measured by the CCD into account.

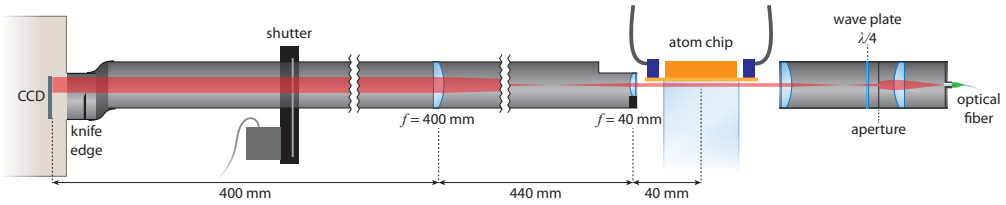

Figure 5.11: Schematic drawing of our primary imaging setup. The linearly polarized probe light from the fiber is made circularly polarized with a quarter wave plate and collimated. An aperture is imaged onto the position of the atoms. After passing through the science cell and atoms, the shadow of the atoms is imaged onto the CCD camera with a $4f$-telescope with 10-fold magnification. A shutter shields the CCD from light during the laser cooling phase of the experiment. A knife-edge is used to block 2/3 of the CCD, which is used as temporary storage for the first two images using frame transfer mode.

a numerical aperture of $NA = 0.32$. The second lens is an achromatic doublet (Thorlabs AC254-400-B) with a focal length of 400 mm. Before installing the imaging setup, we characterize the objective with a 1951 USAF optical calibration target. We measure a magnification of 9.89 and a resolution of ≈ 4 µm.

We record the images with an Andor Ikon-M back-illuminated deep-depletion CCD camera with a quantum efficiency of $Q_e = 0.9$ at $\lambda = 780$ nm. In order to take the three images (2 absorption images and 1 reference image) in quick succession, we use the camera in frame transfer mode. Each image is recorded on only 1/3 of the CCD, with the other 2/3 blocked by a black anodized aluminum "knife edge" placed in front of the camera. Between the images, the frame is shifted by 1/3 into the dark area, resulting in a dead time of only 1.5 ms between images. At the end, the full frame of 3 images (1024×1024 pixels) is read out.

In any imaging setup vibrations in optical elements can cause variations between successive images. These can be especially significant in the presence of interference fringes that may form reflections off optical elements. We minimize such fringes by using an anti-reflection coating on the outside of the science cell, and by carefully aligning the imaging optics. Furthermore, we rigidly mount the imaging optics and camera on damped mounting posts (Thorlabs DP14A/M) to reduce vibrations.

To prevent room light from reaching the camera, the imaging optics are enclosed in 1-inch aluminium tubing. To avoid exposure of the CCD during the laser-cooling phase of the experiment, an external camera shutter (Sutter SmartShutter) is installed between the objective lenses and the camera[17]. The shutter is separately mounted and mechanically detached from the imaging optics and camera. The resulting gaps are closed with electrical tape for blocking room light.

[17] The iKon-M camera also has an internal shutter, but we keep it open during normal operation to preserve the camera lifetime. The internal shutter is rated for 20000 exposures, and we routinely operate the experiments at $>$ 10000 shots per day.

5.9.2 Secondary imaging setup

The secondary imaging setup is aligned along the $-x$-axis (see figure 5.2), with a large field of view of 2.9×2.1 mm. It is used to diagnose the MOT, molasses and initial magnetic trapping stages of the experiment. Only one absorption image is taken with this setup. We can image either $F = 2$, $F = 1$ or both states. To image both states, an optical pumping pulse is used before imaging to include F=1 atoms in the image. To image only $F = 1$, $F = 2$ atoms are in addition "blown away" with a resonant laser pulse if desired.

The probe light is carried in the same fiber as used for optical pumping, and overlapped with the horizontal MOT beam path by a polarizing beam splitter cube (PBS) before the science cell. Then, a quarter-wave plate turns the initial linear polarization to circular. After the science cell, a second quarter-wave plate and PBS separate the MOT and imaging paths. The objective consists of a $4f$-telescope with magnification of 2.23. The images are recorded on an AVT Guppy F-044B NIR CCD camera.

5.9.3 Data analysis

Fringe removal algorithm

In standard absorption imaging, a separate reference image is used for each absorption image (or, in our case, for each set of two absorption images) taken in the same run of the experiment. Using an absorption and reference image taken in quick succession can help to reduce fringes due to vibrating components. However, there is no guarantee that this particular reference image best matches the absorption image. Furthermore, each reference image is affected by photon shot noise, which is the primary source of imaging noise in our setup.

To reduce the effect of photon shot noise in our images, we apply the fringe removal algorithm described in references [137, 138]. For this, we divide our data in blocks of typically 200 consecutive shots. The algorithm works by constructing, for each absorption image, an optimal reference image as a linear combination of the available reference images. The coefficients are chosen to minimize the mean squared residuals between the absorption and the optimal reference image, in a background region where no atoms are present. Thus, in a block of 200 shots, we construct 400 different optimal reference images (for $F = 1$ and $F = 2$) using the same 200 reference images as a basis. The block size is chosen to restrict computation time ($\approx$ 10 s per block). We do not see a significant change in residual image noise compared to a block size of 100.

In addition to reducing noise, the fringe removal algorithm also ensures that the probe intensity in the optimal reference image matches that in the absorption image. This compensates for a small systematic offset in atom number, which arises due to slightly different experimental conditions between the absorption and reference images. Removing this offset is particularly important when mea-

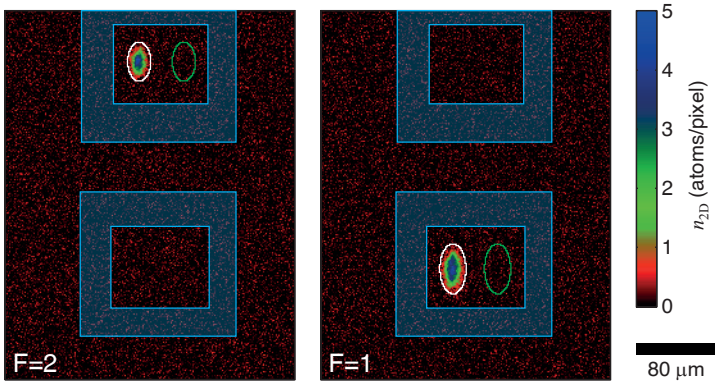

Figure 5.12: Typical absorption image and areas used for analysis. The figure shows n_{2D} for atoms in $F = 2$ (left) and $F = 1$ (right). Atoms are counted in the elliptical region indicated in white, whereas the green region is used to characterize the imaging noise. The blue shaded region is used as background region for the fringe removal algorithm.

suring the contrast of our interferometer, which relies on measuring very close to 0 atoms in either state.

Atom number counting

The number of atoms N_1 and N_2 in states $F = 1$ and $F = 2$, respectively, are calculated by integrating the column density n_{2D}. For the main experiments described in chapter 6, an elliptical integration region is chosen as follows. We extract the position and size of each image from a 2D Gaussian fit, and use the mean position and mean size over the entire data set to define the integration region. We choose the radius of the integration region to be 2.5 σ in each direction, where σ is the $e^{-1/2}$-radius of the fit. The resulting regions contain $> 95\%$ of the atomic distribution. In the scanning-probe measurement of section 6.7, the integration region is chosen for each trap position individually. In other measurements, a slightly larger rectangular region is chosen manually.

Figure 5.12 shows a typical absorption image for each state, and the regions used. Between detecting $F = 2$ and $F = 1$, the atoms have fallen due to gravity. To characterize the detection noise, we use a second integration region where no atoms are present, and calculate the shot-to-shot variance for that region. The background region for fringe removal is chosen outside both integration regions.

The detection noise in our images is dominated by photon shot noise, and for our standard experimental trap ($\eta = 1$) results in noise levels of $\sigma_{N_1,\mathrm{det}} = 5.7$ and $\sigma_{N_2,\mathrm{det}} = 4.2$ atoms (standard deviations) in detecting atoms in $F = 1$ and $F = 2$, respectively. The detection noise in $F = 1$ is larger because the cloud has had more time to expand, requiring a larger integration region. The detection noise corresponds to a noise level of $\sigma_{n,\mathrm{det}} = (5.1 \pm 0.4) \times 10^{-3}$ in the relative atom number difference n. Trap positions close to the surface result in slightly

higher noise levels up to $\sigma_{n,\mathrm{det}} = 6.5 \times 10^{-3}$ for $\eta = 0.5$.

Least-squares fitting to sinusoidal signals

In our experiments, we often measure sinusoidal interferometer fringes. In most measurements, we record Ramsey fringes with a fixed interrogation time T_R, and we vary the offset phase φ_{rf} (see section 3.3).

To extract the interferometric contrast C and phase φ, we perform a least squares fit to the sinusoidal model $n = C\cos(\varphi_{\mathrm{rf}}+\varphi)$. We generally deal with two relevant noise sources, phase noise in φ and detection noise in n. The phase noise is usually dominated by quantum projection noise. The effect of projection noise and other phase noise on n is dependent on φ. Using linear error propagation, the noise in n is

$$\sigma_n^2 = C^2 \sin(\varphi_{\mathrm{rf}} + \varphi)^2 \sigma_\varphi^2 + \sigma_{n,\mathrm{det}}^2 = (C^2 - \langle n\rangle^2)\sigma_\varphi^2 + \sigma_{n,\mathrm{det}}^2.$$

Thus, phase noise is most significant on the slope of the fringe. On the other hand, detection noise is dominant at the minimum and maximum of n, where phase noise has no effect.

To take both noise sources into account we use a weighted fitting routine. As weight, the standard deviation of each data point n_i is estimated by assuming[18] $C \approx 1$, $\langle n\rangle = n_i$ and the phase noise of the standard quantum limit $\sigma_{\varphi,\mathrm{SQL}} = 1/\sqrt{N}$. Using a properly weighted fit is particularly important for determining the interferometric contrast.

In other measurements, such as recording Ramsey fringes as a function of interrogation time, a similar fitting strategy is used with an appropriately adjusted model. Unless noted otherwise, uncertainties given on fit results are 68%-confidence intervals calculated from the fit residuals, and only take statistical uncertainties into account.

Calibration and linearity

We use the method of Ref. [136] to calibrate the parameter α in equation (5.2). The results are consistent with $\alpha = 1$, indicating our probe light is consistent with pure σ^+-radiation. Subsequently, we calibrate the atom number by measuring the shot noise of a coherent state (created by a single Rabi $\pi/2$-pulse) for varying $\langle N\rangle$, and compare to the model $\langle N\rangle^2 \mathrm{var}(n) = \beta\langle N\rangle + \sigma_{N_1,\mathrm{det}}^2 + \sigma_{N_2,\mathrm{det}}^2$. While for a coherent state we expect $\beta = 1$, a linear fit to the data (including the independently measured detection noise at $\langle N\rangle = 0$) yields $\beta = 0.82 \pm 0.07$. We attribute this to an error in calculating the density profiles, as our imaging system

[18] Since the interferometric phase φ is not yet known before the fit, we use each individual data point n_i as an estimate for $\langle n\rangle$ when calculating the weight. This is a good approximation if $\sigma_n \ll 1$. For very noisy data a more rigorous approach would be needed.

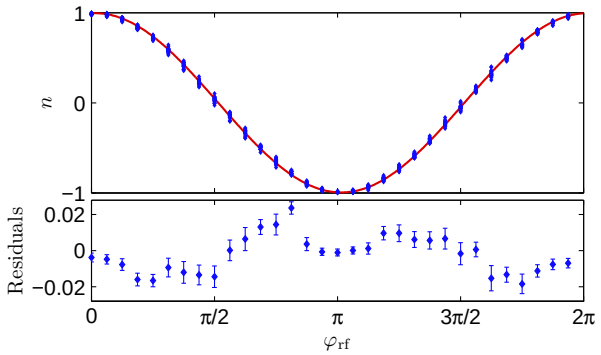

Figure 5.13: Ramsey interferometer output with $T_R = 100$ µs and a coherent input state as function of the offset phase φ_{rf}. Top: experimental data (blue diamonds), with 22 repetitions for each of 32 phase values, and fitted sine (red line). Bottom: residuals from the fit, showing the average (diamonds) and standard error (error bars) over each phase angle.

only partially resolves the clouds, and we divide N_1 and N_2 by β to correct for this error[19].

To verify the linearity of the measured atom number, we perform a phase Ramsey measurement with a short interrogation time of $T_R = 100$ µs and compare the result to equation (3.8). Figure 5.13 shows the measured data along with a fitted sinusoid, as well as the residuals from the fit. The fitted contrast is $C = (99.48 \pm 0.07)\%$. From the residuals, we conclude that the slope of our Ramsey fringes deviates by at most 2% from the model. Together with the calibration uncertainty, this results in a total systematic uncertainty of 10% (0.4 dB) in ξ^2.

5.10 Experiment control and data acquisition

The experiment is controlled by a computer equipped with 4 National Instruments input/output (I/O) cards[20] providing digital and analog outputs [130]. All cards operate at a sampling frequency of 100 kHz. Analog voltage control is used for current sources, the on-chip microwave power (via the set-point of the power stabilization loop), and the slave-injection AOM (via a voltage controlled oscillator). Digital output channels are for various switching and trigger signals.

To control the I/O cards we use the program *goodTime*, originally written by Jakob Reichel and further extended by Pascal Böhi [130]. It interprets a simple scripting language, and allows the construction of complex experimental

[19] In later experiments (mentioned only in the outlook of this thesis), we found that the shot noise was better described by a quadratic relationship $\langle N\rangle^2 \mathrm{var}(n) = \langle N\rangle + \gamma\langle N\rangle^2 + \sigma^2_{N_1,\mathrm{det}} + \sigma^2_{N_2,\mathrm{det}}$, with the linear component consistent with $\beta = 1$. A nonlinear scaling is expected for partially resolved clouds, and the effect may have gotten stronger due to e.g. misalignment of the imaging system.

[20] PCI-6723, PCIe-6259, and two times PCI-6733

sequences. Apart from the I/O cards, it controls test and measurement devices (such as microwave generators in our experiment) via the GPIB bus. I have extended the program to support modern device connectivity via e.g. ethernet and USB.

The VFG 150 RF generator uses a custom data format and is controlled by Matlab scripts running on the same computer. The Matlab scripts are in turn called and configured from goodTime via DCOM[21]. Apart from generating RF signals, the VFG has 4 digital outputs which we use to control MW and RF switces (see section 5.8). These provide 5 ns time resolution synchronized to the 10 MHz reference oscillator. In a typical sequence, we program several subsequences (RF cooling ramps and a Ramsey or other pulse sequence) into the VFG, each started by a separate trigger pulse from the I/O cards.

For data acquisition we use a second computer, which is connected to the imaging cameras. We use a program *MatCam* implemented in Matlab to control and readout the camera, and process the images. It is triggered from goodTime via a DCOM call. MatCam was originally written by Pascal Böhi for our experiment [130], and I rewrote the program from scratch. The new version is written in object-oriented Matlab, and its main advantages are easier extendibility with new fitting functions, post-processing, etcetera. In addition, all configuration parameters are automatically saved with each shot of the experiment. Camera connectivity is either provided by external DLL files (written in C++ by Pascal Böhi), or by using the Matlab Image Acquisition toolbox. The latter toolbox allows most new cameras to be used directly without additional programming.

For the main measurements of this thesis, presented in sections 6.6 and 6.7, I implemented a simple feedback mechanism from MatCam to goodTime. The measurement consists of a series of phase Ramsey measurements (see section 3.3) followed by a measurement whose parameters depended on the outcome of the phase Ramsey (e.g., a noise measurement on the slope of the Ramsey fringe). The MatCam was extended to include phase fitting of sinusoidal signals (see section 5.9.3), and the result was fed back to goodTime. This allowed most measurements to be taken overnight without people present in the lab, aiding the stability of the experiment.

5.11 Typical experimental sequence

The experimental sequence is discussed in detail in reference [60]. Compared to those experiments, small changes have been made over time. Here, I briefly outline the current sequence from hot background vapor to BEC creation.

The sequence starts with loading the MOT for 7 s, using a current of 48 A in the external U-wire (see section 5.1.1) and a laser detuning of -2.5Γ from resonance, where $\Gamma = 2\pi \times 6$ MHz is the natural line width of the cooling transition.

[21] Distributed Component Object Model, a Microsoft technology for inter-process communication.

Subsequently, the MOT is released and re-captured by a smaller MOT created with a current of 7 A in a U-shaped wire on the base chip. During the following 60 ms, the MOT is further compressed and the detuning is switched to $-3.6\ \Gamma$. Finally, the magnetic fields gradients are switched off and the cooling lasers are detuned to $-12\ \Gamma$ for a 2 ms optical molasses stage. At this point, we have up to $\approx 10^7$ atoms at a temperature of $\approx 10\ \mu$K.

After the molasses phase, we optically pump the atoms to $|F = 1, m_F = -1\rangle$ with an 80 µs pulse of both the pump 1-1 and pump 2-2 light (see section 5.6). It is followed by a 100 µs pulse of resonant imaging light, to blow away any atoms that might be left in $F = 2$ after the optical pumping. We then capture the atoms in the first magnetic trap, formed by a Z-wire on the lower layer of the science chip. With well-optimized laser cooling parameters, $\approx 4 \times 10^6$ atoms are trapped in this trap[22].

What follows is a series of magnetic traps, where each next trap is further compressed and closer to the chip surface. The compression raises the temperature, which is partially compensated by self-evaporative cooling by atoms that are too hot for the trap depth. After 4 stages, each with a 100 ms smooth ramp to the next trap, we have $N \approx 2 \times 10^5$ atoms at $T \approx 50\ \mu$K in a dimple trap (see section 2.5.1) with trap geometry of $(\omega_l, \omega_\perp) \approx 2\pi \times (0.5, 2.3)$ kHz at $z_0 = 50\ \mu$m. In this trap, we perform a first evaporative cooling ramp. We apply an exponential RF ramp from 30 → 4.2 MHz during 1.5 s, arriving at $N \approx 6 \times 10^4$ and $T \approx 14\ \mu$K. We then transfer to a dimple trap with $(\omega_l, \omega_\perp) \approx 2\pi \times (0.2, 2.1)$ kHz at $z_0 = 45\ \mu$m, which uses the final set of wires. We perform a second RF cooling ramp from 2.6 → 1.9 MHz during 1 s, producing a BEC of ≈ 4000 atoms.

Finally, we transfer the BEC to the experiment trap described in section 5.4 during 200 ms. To set the final atom number in the BEC, we apply a 20 ms RF pulse at fixed frequency and low power. We then perform the main experiments, which are described in chapter 6.

After the main experiment, we use a kick-out procedure to accelerate the atoms away from the chip surface. This allows absorption imaging with short time of flight, such that the cloud size in the absorption image is small, reducing detection noise. The kick-out procedure works by ramping down the homogeneous magnetic field in 1 ms, while keeping the chip-wire currents constant. The chip wire field then becomes a potential gradient, pushing the atoms way from the chip. After 1 ms, the chip-wire currents are also switched off, and a normal free-space time-of-flight of ≈ 3 ms is used before taking the absorption and reference images.

[22] The atom number in the first magnetic trap is measured after a hold time of 500 ms.

6

Experimental results

In this chapter, I present the main results of this thesis. We generate spin-squeezed states, and use such states as input state for an interferometer. In a scanning-probe measurement, we measure the spatial distribution of a microwave near-field potential. These results have also been published in reference [37]. I conclude the chapter with a discussion of the noise sources relevant to our experiments.

6.1 Rabi oscillations

We drive coherent Rabi rotations between states $|1\rangle$ and $|2\rangle$ using a two-photon microwave and radio frequency transition, described in section 2.3.4. Both fields are generated off-chip, as described in section 5.8.3. Compared to previous experiments [12], we use lower MW and higher RF power. For our state pair the linearly polarized RF field generates no differential level shift, and thus lowering microwave power while increasing the RF power reduces the total power sensitivity of the two-photon Rabi detuning δ at a fixed two-photon Rabi frequency.

We typically couple ≈ 2 W of RF power into the RF coil and ≈ 10 mW of microwave power into the microwave horn. We detune the MW by $\Delta = 2\pi \times 500$ kHz above the $|F = 2, m_F = 0\rangle$ intermediate state. We find the two-photon resonance condition by adjusting the RF frequency to minimize Ω_{eff}, and calibrate Ω_{eff} by measuring the relative population n for a varying time t for several Rabi cycles.

Figure 6.1 shows a measurement of Rabi cycles on an ensemble initially polarized in state $|1\rangle$. The contrast of the Rabi cycles shows a sinusoidal modulation, which we attribute to spatial inhomogeneity of the MW field. Such an inhomogeneity creates a state-selective potential, which could cause demixing and remixing dynamics of the two states, similar to that described in section 6.3. At the first contrast revival, around $t = 38$ ms, we observe $> 95\%$ contrast, indicating the $1/e$ decay time is > 700 ms at the contrast revival times.

Although we generate both MW and RF fields for the Rabi pulses off chip, a spatial inhomogeneity of the fields is not unexpected when operating close to

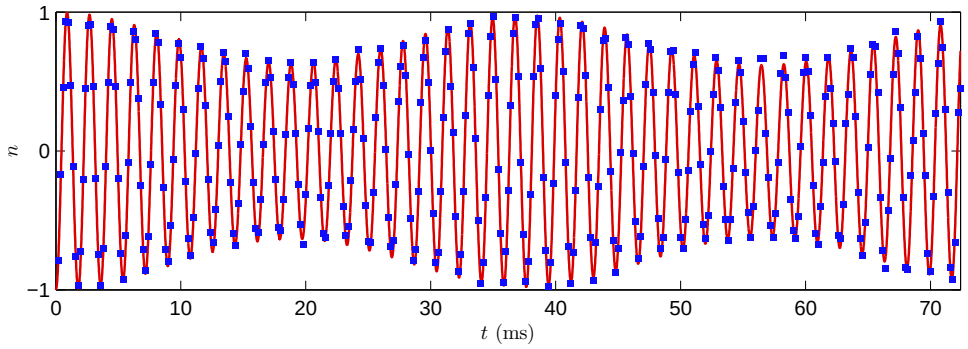

Figure 6.1: Rabi oscillations, showing experimental data (blue) and an amplitude-modulated sine fit (red). Due to inhomogeneity of the microwave and radio frequency field, we see a collapse and revival of the Rabi contrast. The Rabi frequency is $\Omega_{\text{eff}} = 2\pi \times (557.87 \pm 0.02)$ Hz in this measurement.

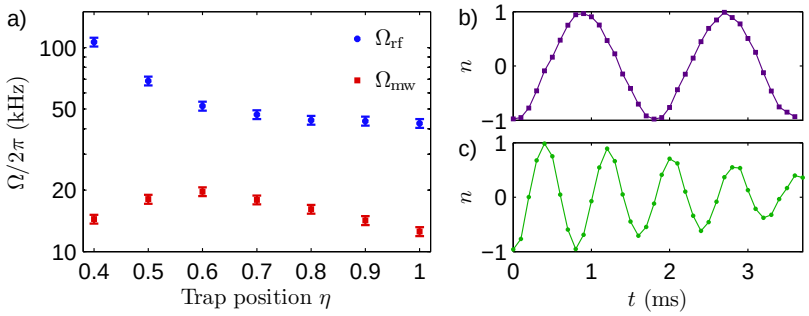

Figure 6.2: Position dependent Rabi frequency. a) Estimated microwave Rabi frequency Ω_{mw} (red squares) and RF Rabi frequency Ω_{rf} (blue circles). Error bars indicate statistical uncertainty. b) Example of Rabi oscillations for $\eta = 1$. c) Rabi oscillations at $\eta = 0.5$, where the contrast decays quickly due to the inhomogeneous Rabi frequency.

a structured metal surface such as our atom chip. The fields can couple to the metal structures, and thus create local gradients.

For a single short Rabi pulse the collapse and revival of contrast has little effect, since the contrast envelope is essentially a cosine. Based on the very short Ramsey measurement of figure 5.13, we estimate a fidelity of $(99.74 \pm 0.04)\%$ for a single $\pi/2$-pulse.

Due to the spatial inhomogeneity of the RF and MW fields, we see a different Rabi frequency and two-photon resonance condition at each trap position. Therefore, we calibrate both the two-photon resonance and Rabi frequency for each position independently. Using equations (2.18), we can estimate the individual MW and RF Rabi frequencies (Ω_{mw} and Ω_{rf}, respectively) from the calibration data.

Figure 6.2a shows the estimated MW and RF Rabi frequency for each trap

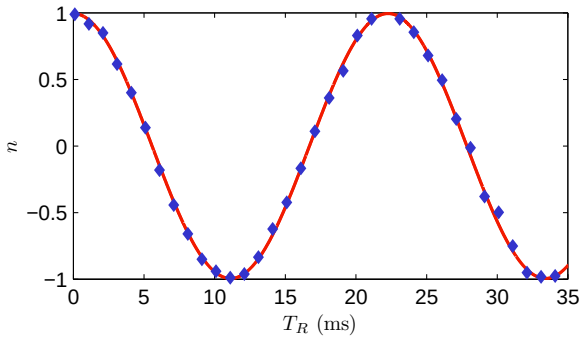

Figure 6.3: Ramsey measurement as function of interrogation time T_R. Shown are experimental data (blue diamonds) and sinusoidal fit (red line). The fit result an oscillation frequency of $\delta = -2\pi \times (44.9 \pm 0.1)$ Hz and a contrast of $C = (99.5 \pm 0.4)\%$.

position. The trap position is labeled by the parameter η from equation (5.1). Close to the surface, both fields show a strong position dependence, whereas around $\eta = 1$ only the microwave field has a strong gradient. Part b of figure 6.2 shows Rabi cycles recorded at $\eta = 1$ and at $\eta = 0.5$. Due to the stronger field gradient, the contrast decay occurs after only a few cycles for $\eta = 0.5$. However, after a single π-pulse, the contrast is still $\gtrsim 98\%$. The two-photon Rabi frequency at $\eta = 0.5$ is $\Omega_{\text{eff}} = 2\pi \times (1239 \pm 2.5)$ Hz.

In our present measurements, we use the same RF and MW power settings for each trap position. Note that for more complex sequences, where more or longer Rabi pulses are required, it may be beneficial to reduce in particular the RF power when operating close to the surface. Improvements may be gained by using on-chip RF and possibly MW fields. While on-chip MW and RF currents create large gradients close to the surface, their properties can be controlled understood very well. For example, the RF gradient can be aligned perpendicular to the long axis of the trap to minimize its effect. This technique has been used in several atom chip experiments [68, 69].

6.2 Ramsey interferometry

Figure 6.3 shows an example of a time-domain Ramsey measurement for varying interrogation time T_R at fixed phase and frequency. The sequence consist of two Rabi pulses with a duration t such that $\Omega_{\text{eff}} t = \pi/2$ ($\pi/2$-pulses), separated in time by T_R (see section 3.3). The Rabi pulses are tuned to two-photon resonance, and the remaining oscillation frequency is equal to the detuning δ due to the microwave level shift during the pulses (see equation (2.18)). From a sinusoidal fit to the data, we obtain $\delta = -2\pi \times (44.9 \pm 0.1)$ Hz. The sign of δ was separately verified by repeating the measurement with an added "artificial detuning" δ_{clock}, realized by setting the phase of the second $\pi/2$-pulse in each shot to $\varphi_{\text{rf}} = \delta_{\text{clock}} T_R$.

6.3 Splitting and recombination

As described in section 2.4.3, the strength χ of the non-linear Hamiltonian $H_{\text{int}} = \chi S_z^2$ scales with the wave-function overlap of the two states. We effectively "turn on" χ by spatially separating the wave functions of state $|1\rangle$ and $|2\rangle$, and "turn off" it's effect by recombining them. We control the separation using the state-selective microwave potential described in section 5.5. However, we find that the mean-field interactions also play an important role in determining the dynamics of the two-component BEC. For the experiments described in this chapter, we use a "dynamic" splitting and recombination technique: we separate the potential minima by only a small amount, but the mean-field interaction between the two components strongly enhances the separation[1].

The sequence is as follows. Initially, the atoms are polarized in the $|1\rangle$ state. We apply a $\pi/2$ Rabi pulse to create an equal superposition of $|1\rangle$ and $|2\rangle$. Then, we spatially separate the trapping potentials of the two interferometer states by switching on the state-dependent MW potential. We turn on the potential with a smooth ramp of 350 µs, slow enough to allow adiabatic microwave dressing of the potential, but much faster than the motional dynamics of the atoms. As the atomic wave-functions are now no longer in the minimum of their respective potential, they start to coherently de-mix and oscillate in the traps. After one oscillation, during which the squeezing rate χ is nonzero, we switch off the state-dependent potential to re-capture the atoms at the minimum of the original state-independent magnetic trap, and apply further Rabi rotations to orient the squeezed state as needed and perform interferometric measurements.

We use a far off-resonant microwave signal in the co-planar waveguide, blue-detuned by $\Delta_0 = 2\pi \times 12$ MHz from the $|1,0\rangle \leftrightarrow |2,0\rangle$ transition. We estimate the splitting distance between the potential minima of the two states to be $\Delta x_0 \approx 140$ nm, aligned with the x-direction. Although Δx_0 is much smaller than the extension of the BEC ($R_{\text{TF}} \approx 4.0$ µm along x), the wave functions split much further due to mean-field repulsion of the two states. The resulting oscillation frequency is slower than the trap frequency.

6.3.1 Collapse and revival of interferometric contrast

We characterize the splitting and recombination sequence by embedding it in a Ramsey measurement. After the first $\pi/2$-pulse, we turn on the state-selective potential for a variable time T_S. After T_S, a second $\pi/2$-pulse completes the Ramsey sequence and the populations are read out. Like in a normal time-Ramsey measurement, we observe interference fringes with a frequency determined by the

[1] Recently, a scheme has been proposed without state-dependent potentials, using only the mean-field interaction to drive splitting and recombination dynamics [139]. In that scheme, the difference in scattering lengths provides the required asymmetry, and the oscillations are in a spherical breathing mode. In our experiments, the state-dependent potential dominates over the difference in scattering length.

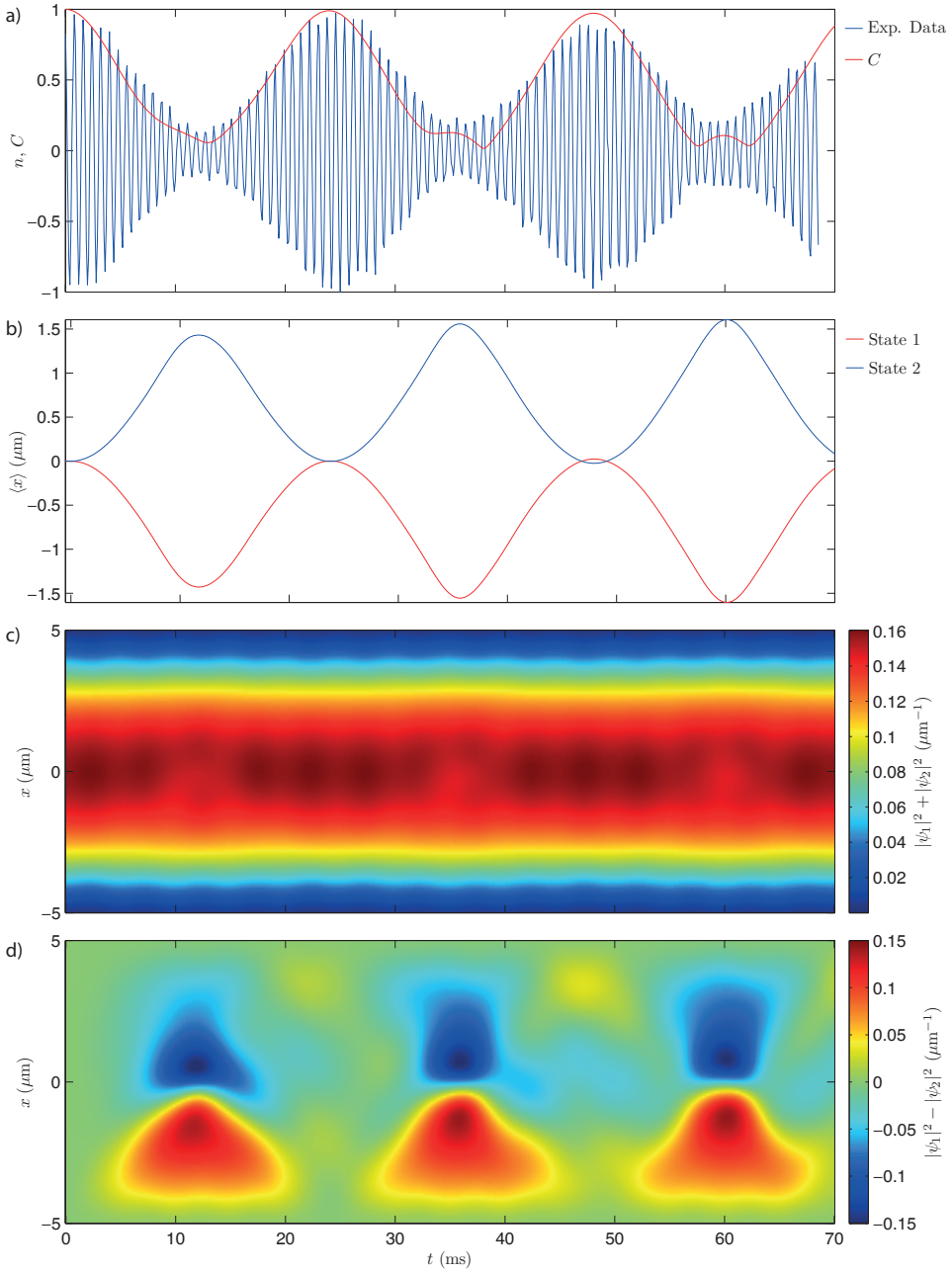

Figure 6.4: Dynamic splitting and recombination. a) Ramsey fringes (blue) recorded with a variable hold time T_S. During T_S the microwave near-field is turned on, and the potential minima of state $|1\rangle$ and $|2\rangle$ are separated by ≈ 140 nm. This causes the wave functions ψ_1 and ψ_2 to oscillate in opposing directions. The contrast C calculated from a 1D GPE simulation is shown in red. b) Simulated center-of-mass position along the splitting direction of each state. c) Sum and d) difference of the simulated densities.

energy shift between the two interferometer states. The *contrast* of the fringes scales with the wave-function overlap, since parts of the BEC that do not overlap also cannot interfere. As the two components of the BEC oscillate in opposing directions, we expect to see an oscillating collapse and revival of the interferometric contrast.

Figure 6.4a shows an example of such a Ramsey measurement with splitting and recombination. The interferometric contrast oscillates with a frequency of 42 Hz. At maximum separation, the contrast is reduced to $\approx 20\%$, but after one period the contrast is almost fully restored. The collapse and revival of contrast continues for many cycles, although with each cycle the peak contrast is reduced. Compared to previous experiments in our group [12], we use a smaller splitting distance. This results in longer time to the first revival and higher remaining overlap between the revivals (thus slower rate χ), but we find it gives larger contrast at the revival.

We compare the measured contrast with a numerical simulation of the two-component Gross-Pitaevskii equation (GPE, equation (2.4)) in one dimension. We numerically integrate the GPE using a split-step method, where the kinetic energy term is integrated in Fourier space and the potential and mean-field terms are integrated in real space [140]. In figure 6.4a, the simulated contrast $C = |\langle\psi_1|\psi_2\rangle|$ is shown. Here, ψ_1 and ψ_2 are the mode functions of state $|1\rangle$ and $|2\rangle$, respectively, normalized to 1. With the splitting distance adjusted to 138 nm, the simulation reproduces the experimentally observed frequency of collapse and revival of the contrast. The simulation predicts somewhat stronger collapse than observed in the experiment. This is likely because the one-dimensional simulation does not allow dynamics in the transverse trap dimensions, whereas in reality the BEC is not in the 1D regime[2].

Part b of figure 6.4 shows the center-of-mass (COM) position of each condensate component obtained from the simulation. The maximum separation between the two states' COM during the first oscillation is 2.9 µm. Part c and d of the figure show the simulated total and difference density profiles, respectively. The total density stays close to constant, even though the two components split almost completely. The shape of the individual wave functions thus changes dramatically during the sequence. The difference in shape between the two states arises from the slightly asymmetric scattering lengths a_{ij}. Setting all scattering lengths equal gives symmetric, but otherwise almost identical results.

First revival

Figure 6.5 shows another measurement of dynamic splitting embedded in a Ramsey sequence, focusing on the first revival of the contrast. To estimate the optimal

[2] Our experiment is between the 1D and the Thomas-Fermi (TF) regime. In the simulation, we adjust g such that μ would be correct in the TF regime, but the results are very similar if we choose g to match the 1D regime (by assuming the harmonic oscillator ground state wave function in the transverse direction).

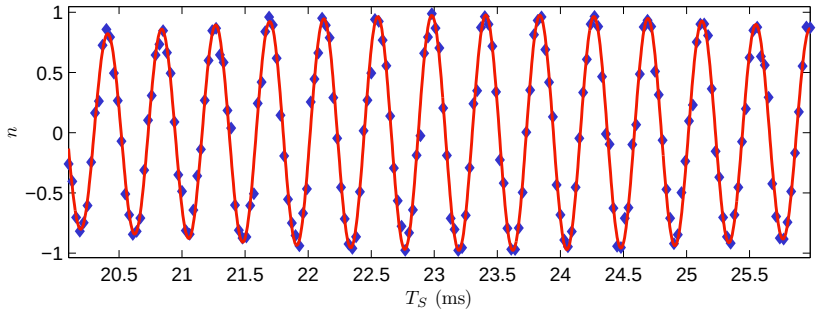

Figure 6.5: First contrast revival in dynamic splitting and recombination. Ramsey data (blue points) and fitted sine with Gaussian envelope (red line). The Ramsey fringes have a frequency of 2334 ± 1 Hz. The peak contrast in this measurement is found at $T_S = 23.3 \pm 0.1$ ms.

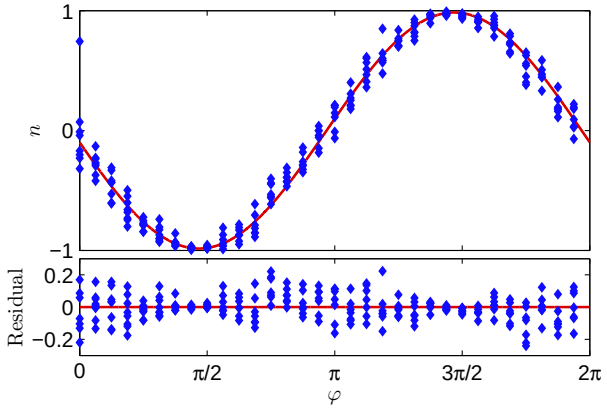

Figure 6.6: Ramsey measurement at the first revival, with fixed $T_S = 23.4$ ms and varying phase φ_{rf} of the second $\pi/2$-pulse. Experimental data (blue diamonds) and sine fit (red line) giving a contrast of $C = (98.4 \pm 0.4)\%$. Bottom: residuals of the fit.

T_S where the contrast is maximized, we fit a sinusoid multiplied by a Gaussian envelope to the data. The fitted maximum of the envelope is at $T_S = 23.3 \pm 0.1$. We routinely repeat this measurement before taking further data, and found the contrast revival time stable within ± 0.2 ms during the course of half a year in which the data for this chapter was recorded.

In this measurement, the Ramsey fringes have an oscillation frequency of $\delta_R = 2\pi \times (2334 \pm 1)$ Hz. It is composed of three contributions: the microwave level shift $\delta = -2\pi \times (44.9 \pm 0.1)$ Hz measured in figure 6.3; an artificial detuning $\delta_{\mathrm{clock}} = 2\pi \times 2$ kHz; and the level shift $V_{\mathrm{mw}}/\hbar$ due to the *on-chip* microwave field during T_S. Combining the results, we find $V_{\mathrm{mw}} = h \times (415 \pm 2)$ Hz in this data set.

Figure 6.6 shows a Ramsey measurement at the first contrast revival. Data is taken at fixed splitting time of $T_S = 23.3$ ms, as a function of the phase φ_{rf} of the

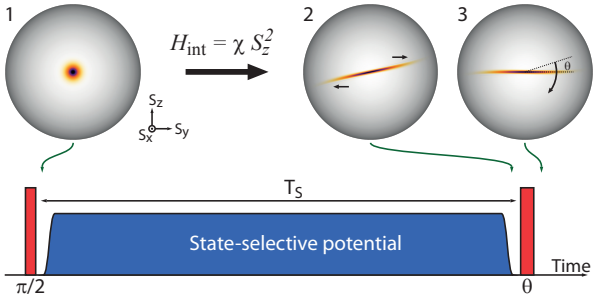

Figure 6.7: Sequence to prepare and characterize a spin-squeezed state. The figure shows Rabi pulses (red) and on-chip microwave pulses (blue). Spheres 1-3 show the Wigner function of the collective spin state at various stages of the experiment, simulated for $N = 200$ atoms.

second $\pi/2$-pulse. We fit the contrast as described in section 5.9.3, and obtain $C = (98.0 \pm 0.4)\%$. This characterizes the fidelity of our spin-squeezing sequence, and in particular gives a lower bound on the wave-function overlap obtained using the dynamic splitting and recombination scheme. We repeat this measurement each time we prepare spin-squeezed states, and typically find a contrast in the range of $97\% - 99\%$.

Compared to a standard Ramsey sequence such as shown in figure 5.13, one notices that the noise in figure 6.6 has significantly increased. Although this may in part be technical phase noise due to the longer interrogation time, it is also a first hint at the non-linear dynamics of the squeezing Hamiltonian (3.27) that have occurred during T_S. A Ramsey measurement is sensitive to the interferometer phase, and if no further rotations are performed the collisional interactions lead to phase diffusion (i.e., the anti-squeezed quadrature of the collective spin) [114]. To reveal the useful effects of collisions, a more complex sequence is needed, as described in the following section.

6.4 Spin-squeezed state

To characterize the quantum state after splitting and recombination, we use the sequence depicted in figure 6.7. To visualize the sequence, we show the expected Wigner function on the Bloch sphere, calculated for $N = 200$ atoms (see section 2.4.4). The sequence starts with a $\pi/2$-pulse as before. We now choose an explicit phase reference frame and denote this initial pulse to be around the $-y$-axis on the Bloch sphere. Sphere (1) shows the resulting coherent state, aligned with the x-axis. Next, we apply the state-selective potential for a time $T_S = 23.4$ ms, during which the wave functions split once and recombine to maximum overlap. We choose the phase-reference frame to co-rotate such that $\delta_R = 0$, and the state remains aligned with the x-axis. During T_S, χ is non-zero and the non-linear collisional interaction $H_{\text{int}} = \chi S_z^2$ leads to entanglement.

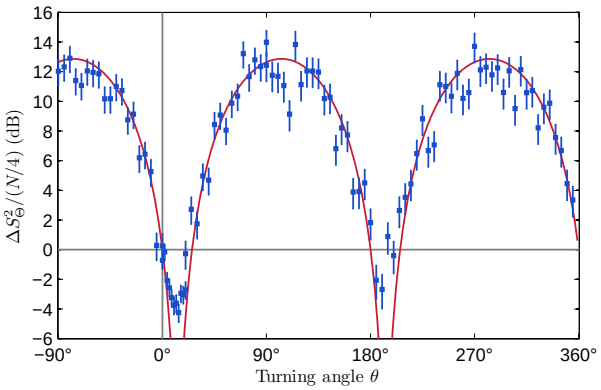

Figure 6.8: Characterization of a spin-squeezed state. Blue points show the variance relative to the SQL as a function of turning angle θ. The independently measured contribution from imaging noise has been subtracted. Error bars indicate statistical uncertainty based on the number of shots used in each data point. The best squeezing is found to be $\zeta^2 = -4.3 \pm 0.6$ dB at $\theta = 14°$. The contrast for this data set was $C = (94.1 \pm 0.4)\%$. Red line shows the variance of a simulated squeezed state with $\chi T_S = 0.003$, which has a minimum variance of $\zeta^2_{\text{sim}} = -12.9$ dB at $\theta = 12.8°$.

Sphere (2) shows the simulated Wigner function. Although the phase is diffused, the state is *squeezed* along a particular direction in the x, y-plane. To investigate the squeezing, we apply rotation by a variable angle θ around the $-x$-direction.

For each turning angle θ, we repeat the measurement many times. Although the mean $\langle n \rangle \approx 0$, the variance σ_n^2 varies with θ, reflecting the squeezed and anti-squeezed quadratures. Figure 6.8 shows an example of such a measurement, with up to 150 shots of the experiment per tuning angle. The figure shows the measured variance $\zeta^2 = 4\text{var}(S_\theta)/N$ (for a coherent state $\zeta^2 = 1$). The effect of detection noise is subtracted from each data point. Detection noise alone corresponds to $\zeta^2_{\text{det}} = -10.8$ dB.

For a turning angle of $\theta = 0$, the measured variance is consistent with that of a coherent state. For small positive θ, lower noise is observed. This corresponds to sphere (3) in figure 6.7, where the *squeezed* direction is aligned with S_z. The lowest variance in this measurement is found to be $\zeta^2 = -4.3 \pm 0.6$ dB at $\theta = 14°$. Turning another 90° aligns the *anti-squeezed* direction with S_z, and the measured noise is far above that of a coherent state. For comparison, the phase noise visible in figure 6.6 corresponds to $\theta = 90°$, and is almost along the anti-squeezed direction. Turning further, a second minimum is visible with $\zeta^2 = -2.2 \pm 0.9$ dB at $\theta = 190°$. In theory, this noise level should correspond exactly to $\theta = 10°$, but the longer pulse required may lead to extra technical noise.

We compare the squeezed measurement to that of a simulated state with $N = 1400$. In the simulation, after the first $\pi/2$-pulse the state is evolved under H_{int} for $\chi T_S = 0.003$. Then, the variance $\text{var}(S_\theta)^2$ is calculated as a function of the turning angle θ. No technical noise contributions or losses are taken into

Date	$\langle N \rangle$	Contrast (%)	ξ^2 (dB)	$\sigma_{n,\mathrm{det}}$	ζ^2 (dB)
14-12-2011	1320 ± 49	98.4 ± 0.4	-3.9 ± 0.3	5.0×10^{-3}	-4.4 ± 0.4
15-12-2011	1350 ± 47	98.1 ± 0.3	-4.6 ± 0.4	4.9×10^{-3}	-5.2 ± 0.5
16-12-2011	1429 ± 34	98.4 ± 0.6	-4.3 ± 0.4	4.4×10^{-3}	-4.8 ± 0.5

Table 6.1: Measurement of our spin-squeezed state on three consecutive measurement days, characterized by the mean atom number $\langle N \rangle$, the contrast C and the squeezing factor ξ^2, measured at a turning angle of $\theta = 12°$. Listed uncertainties are standard deviation of the data for $\langle N \rangle$, fit uncertainty for C and statistical uncertainty for ξ^2. The systematic uncertainty on ξ^2 is 0.4 dB. The detection noise $\sigma_{n,\mathrm{det}}$ is measured independently in each data set and used to calculate the estimated noise reduction $\zeta^2 = \langle N \rangle(\sigma_n^2 - \sigma_{n,\mathrm{det}}^2)$.

account. The optimal squeezing found in the simulation is $\zeta^2 = -12.9$ dB at $\theta_{\mathrm{opt}} = 12.8°$. The value of χT_S was chosen to approximately match θ_{opt} to the experimental data.

Following the measurement of figure 6.7, several experimental improvements were made to reduce technical noise. In particular, new signal generator[3] was installed for the microwave part of the Rabi pulses, significantly reducing the noise induced by multiple Rabi pulses.

Table 6.1 shows an overview of characterization measurements taken of spin-squeezed states after the new microwave generator was installed. Each measurement is taken at a turning angle of $\theta = 12°$, with up to 180 shots per measurement. The contrast C is measured for each set directly before measuring the variance. The interferometrically useful squeezing is calculated from the data as $\xi^2 = \langle N \rangle \sigma_n^2 / C^2$. We do not subtract detection noise when calculating ξ^2. We consistently obtain around 4 dB of useful squeezing with an interferometric contrast above 98 %.

6.4.1 Multi-particle entanglement

As described in section 3.7, quantum metrology and entanglement are closely related concepts. Figure 6.9 shows the measured depth of entanglement for our experiment. Plotted on the vertical axes is $\mathrm{var}(S_\theta)/S$, which we associate with $\zeta^2/2$ in the experimental data[4]. Lines correspond to the best results possible with a k-particle entangled state for several example values of k (based on equation (3) of reference [97]). The experimental results corresponding to the squeezed states listed in table 6.1 are overlayed on the graph. Our best result corresponds to at least 40 ± 8-particle entanglement. It should be noted that the particles in

[3] First a refurbished HP 8340B, later a Rohde & Schwarz SGS100A. Both devices have similar phase noise characteristics. Previously, an SRS SG384 with frequency doubling option was used.

[4] Note that $\mathrm{var}(S_\theta)/S = \zeta^2/2$ only for symmetric states with a fixed particle number, and ζ^2 measures phase uncertainty relative to the SQL corresponding to the *mean* $\langle N \rangle$. A detailed treatment including fluctuating particle numbers is given in [98].

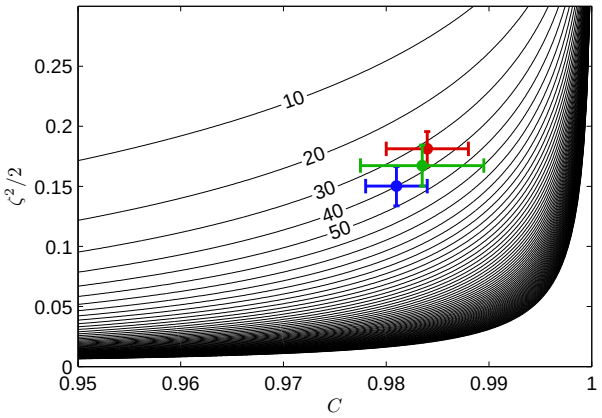

Figure 6.9: Depth of entanglement calculated according to reference [97]. The calculation is valid for large entanglement and $C \approx 1$. Lines correspond to k-particle entanglement for $k = 10, 20, 30, \cdots, 1400$. The red, blue and green data point correspond to the squeezed states of table 6.1 and fall on the lines $k = 32 \pm 7$, $k = 40 \pm 8$ and $k = 37 \pm 11$, respectively.

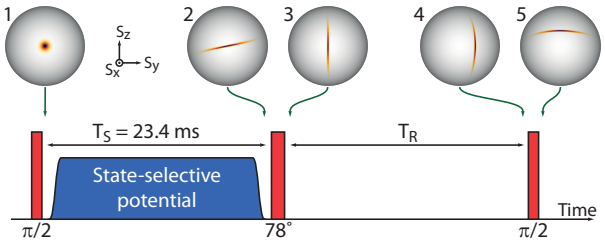

Figure 6.10: Squeezed-state interferometer sequence. The figure shows Rabi pulses (red) and on-chip microwave pulses (blue). Spheres 1-5 show the Wigner function of the collective spin state at various stages of the experiment, simulated for $N = 200$ atoms.

a pure BEC are indistinguishable, and separating the system into groups of 40 particles does not represent a symmetric state. Instead, we can conclude that all particles are entangled by some amount [98].

6.5 Squeezed-state interferometer

In the previous sections, I described how we have created and characterized spin-squeezed states of our two-component BEC. To demonstrate that these states can be used for entanglement-enhanced interferometry, we use the squeezed state as input to a Ramsey interferometer.

The sequence is shown in figure 6.10. First, we create the squeezed state with a $\pi/2$-pulse and the state-dependent potential (spheres 1-2). Then, we rotate by 78° around the positive x-axis. This aligns the squeezed quadrature with the

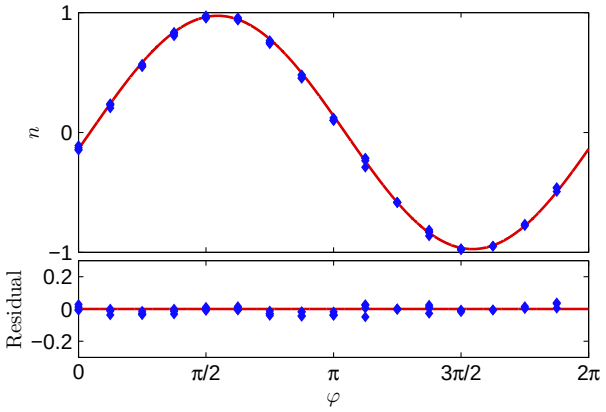

Figure 6.11: Squeezed-state interferometer fringe with $T_R = 729$ µs. Experimental data (blue diamonds) and sine fit (red line) giving a contrast of $C = (97.3 \pm 0.2)\%$. Bottom: residuals of the fit.

equator of the Bloch sphere (sphere 3) and makes the state maximally phase sensitive. The combined steps up to sphere 3 can be thought of as replacing the first pulse of a normal Ramsey interferometer. The sequence continues like a normal Ramsey sequence. During the interrogation time T_R, a phase φ_R is accumulated (sphere 4), which is the quantity to be measured. After T_R, a final $\pi/2$-pulse rotates the state around the y-axis and maps φ_R onto n (sphere 5).

Figure 6.11 shows a squeezed-state Ramsey measurement with an interrogation time of $T_R = 729$ µs. The interferometric contrast is $C = (97.3 \pm 0.2)\%$. Directly after this measurement, we measured the noise level on the slope of the fringe in 240 shots of the experiment. The squeezing factor at the end of the interferometer sequence was $\xi^2 = -3.9 \pm 0.4$ dB.

In general we observe slightly lower contrast compared to the input state due to the added complexity of the sequence. In particular, an error in calibrating the phase of the 78°-pulse translates into reduced contrast of the interferometer.

6.6 Lifetime of the squeezed state

In many applications such as atomic clocks, interferometric sensitivity scales linearly with T_R, and long interrogation times are desired. We therefore measure the performance of our interferometer as a function of T_R, similar to the measurements performed in reference [22].

Figure 6.12 shows the measured squeezing factor (at the end of the interferometer sequence) for varying T_R. The interferometer operates at $\xi^2 \approx -4$ dB below the SQL, and it performs below the SQL up to $T_R = 10$ ms. For comparison, we repeat the measurement with a coherent input state, using a standard Ramsey sequence. This reference measurement is consistent with the SQL plus

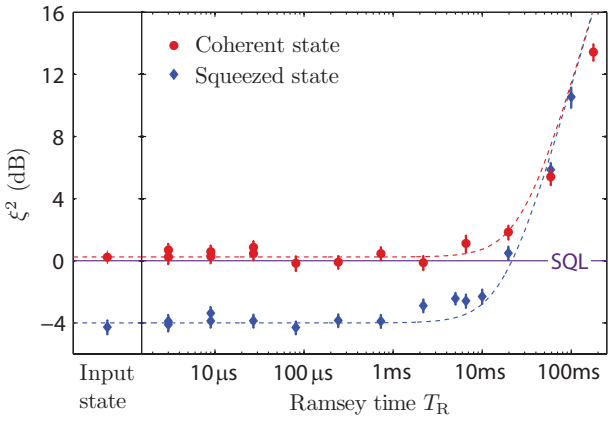

Figure 6.12: Interferometer performance. Observed phase noise in a Ramsey interferometer with squeezed (blue diamonds) and coherent (red circles) input states for varying interrogation times T_R. Dashed lines model constant performance of $\xi^2 = -4$ dB (squeezed state) and +0.2 dB (coherent state), plus noise due to shot-to-shot frequency fluctuations. Each data point is the result of 240 measurements, and error bars indicate statistical uncertainty.

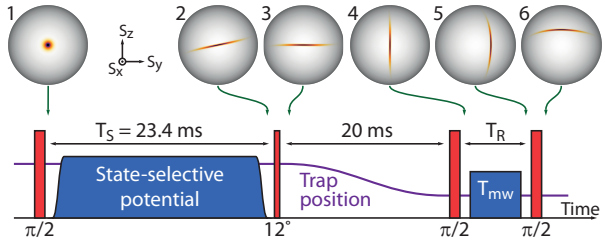

Figure 6.13: Experimental sequence for the scanning-probe interferometer. The figure shows Rabi pulses (red), on-chip microwave pulses (blue) and the trap position (purple). Spheres 1-6 show the Wigner function of the collective spin state at various stages of the experiment, simulated for $N = 200$ atoms.

detection noise.

For $T_R > 20$ ms, both measurement are limited by technical or other noise. The measured noise level is consistent with shot-to-shot fluctuations of 150 mHz in the relative frequency between our reference oscillator and the atomic resonance. Possible contributions to this noise are discussed in section 6.10.2.

6.7 Scanning-probe interferometer

In the previous sections, we have demonstrated sub-SQL interferometry with a small probe, but have only measured at one position in space. To demonstrate position-dependent measurements, we realize a scanning-probe interferometer with squeezed input state.

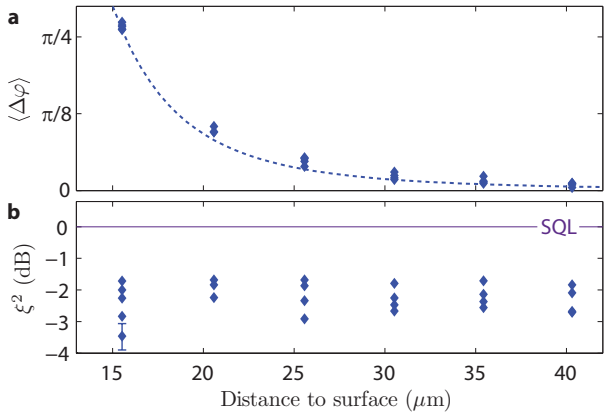

Figure 6.14: Scanning probe interferometer operating below the SQL. a) Measured phase shift $\langle\Delta\varphi\rangle$ induced by a microwave near-field pulse as a function of the atom–surface distance, compared to the simulated potential (dotted line). b) Measured performance of the interferometer, expressed as squeezing factor ξ^2. Each data point (based on 240 measurements) has a statistical uncertainty of ± 0.4 dB, shown as error bar on the lower left point. The experiment was repeated up to 5 times at each position.

Figure 6.13 shows the experimental sequence of our scanning-probe interferometer. First, we create a squeezed input state as before (spheres 1-2). Next, we apply a $-12°$ rotation around the x axis, aligning the anti-squeezed quadrature with the equator (sphere 3). This renders the state minimally sensitive to phase noise during the following 20 ms, in which we transport the atoms to the position where the interferometric measurement is to be made. Finally, we perform a full Ramsey interferometer sequence consisting of a $\pi/2$-pulse around the state's center to make it maximally phase sensitive (sphere 4), an evolution time T_R during which the phase φ_R is accumulated (sphere 5), and a final $\pi/2$-pulse mapping φ_R onto n (sphere 6).

We demonstrate the scanning probe interferometer with spatially resolved measurements of the on-chip microwave near-field at 6.8 GHz. We use $T_R = 100$ µs, during which we pulse on the field for $T_\mathrm{mw} = 80$ µs with the same detuning of $\Delta_0 = 2\pi \times 12$ MHz as used for the state-dependent potential (see section 5.5), but at a lower microwave current of ≈ 5 mA. This results in an additional phase shift $\Delta\varphi = T_\mathrm{mw} V_\mathrm{mw}/\hbar$ where V_mw is the differential ac Zeeman shift of states $|1\rangle$ and $|2\rangle$.

Figure 6.14a shows measurements of $\langle\Delta\varphi\rangle$ at the positions indicated in figure 5.6, between 40 µm and 16 µm from the chip surface. At each position we perform two separate measurements. First, we measure the phase φ_mw which is accumulated with V_mw enabled. We do 60 runs of the experiment with varying offset phase φ_rf, and extract the mean $\langle\varphi_\mathrm{mw}\rangle$ by performing a least-squares fit to the model $n = C\cos(\varphi_\mathrm{rf} - \langle\varphi_\mathrm{mw}\rangle)$ as described in section 5.9.3. Then we repeat the sequence without mw pulse to measure the reference phase $\langle\varphi_\mathrm{ref}\rangle$. The mean

phase shift due to the mw is given by $\langle\Delta\varphi\rangle = \langle\varphi_{\mathrm{mw}}\rangle - \langle\varphi_{\mathrm{ref}}\rangle$.

The measured shape of V_{mw} agrees well with the simulated potential (see section 5.3 and figure 5.6). Since the present measurement is more precise, we use it to calibrate the efficiency of coupling the mw current onto the chip. The resulting global calibration factor agrees well with the measured mw transmission through the chip, if we assume that there are equal losses before and after the experiment region of the co-planar wave guide.

Figure 6.14b shows the performance of our interferometer in terms of the squeezing factor ξ^2. We measure the performance in 240 runs of the experiment, while operating at $\varphi_{\mathrm{rf}} = \langle\varphi_{\mathrm{mw}}\rangle + \pi/2$, such that $\langle n\rangle = 0$. For all positions, our interferometer performs well below the SQL, with an average performance of $\langle\xi^2\rangle = -2.2$ dB corresponding to a single-shot phase sensitivity of $\sigma_{\varphi_{\mathrm{mw}}} = 1.2°$. We attribute the reduction of squeezing compared to the input state to the extra Rabi pulses and extra time needed to transport the atoms.

The strength of V_{mw} is chosen such that the interferometric contrast remains $C \gtrsim 95\%$ at the position closest to the chip surface, $\eta = 0.5$. Even closer to the surface, at $\eta = 0.4$, we observed strongly reduced contrast due to the gradient across the extent of the cloud (see section 4.3). The product $V_{\mathrm{mw}}T_{\mathrm{mw}}$ was therefore approximately optimal for $\eta = 0.5$ for our cloud size. Note, however, that measurements closer to the surface could be performed with lower field amplitude or shorter interrogation time.

6.8 Sensitivity to microwave magnetic fields

Our interferometer is sensitive to a microwave level shift of $V_{\mathrm{mw}}/B_{\mathrm{mw}}^2 = h \times 71\ \mathrm{kHz/G^2}$ for a linearly polarized microwave magnetic field driving π-transitions with a detuning of $\Delta_0 = 2\pi \times 12$ MHz (see section 5.5). For such a field, the measured phase sensitivity $\sigma_{\varphi_{\mathrm{mw}}} = 1.2°$ of our scanning-probe interferometer corresponds to a noise-equivalent microwave field amplitude of $\sigma_{B_{\mathrm{mw}}} = 2.4\ \mu\mathrm{T}$. The sensitivity for small fields can be improved by using a smaller detuning[5] to increase V_{mw}, and by increasing the interrogation time T_{mw}.

The largest level shift V_{mw} is obtained by choosing the microwave frequency close to resonance with a single transition $|1, m_1\rangle \leftrightarrow |2, m_2\rangle$. Close to resonance, the interferometer is also polarization dependent, depending on the chosen transition. Choosing the detuning $\Delta_{1,m_1}^{2,m_2} \approx \Omega_{1,m_1}^{2,m_2}$ such that Rabi rotations are just avoided, the level shift is approximately $V_{\mathrm{mw}} \approx \mu_B B_{\mathrm{mw}}$ up to a factor of order unity depending on the transition matrix element (see equation (2.12)).

To make an estimate of our ultimate sensitivity for weak microwave fields[6],

[5] In this proof-of-principle experiment, it was convenient to use the same detuning Δ during T_S and T_{mw}. However, if an independent microwave field is to be measured the detuning can be chosen close to resonance.

[6] For very weak fields, the field gradient neither significantly perturbs the potentials nor causes inhomogeneous dephasing, and we can choose the longest interrogation time allowed by

we take the best squeezed-state performance of figure 6.12. At $T_R = 10$ ms our measured noise level corresponds to a sensitivity in the ac Zeeman shift of $\sigma_{V_{\mathrm{mw}}} = h \times 0.33$ Hz, or a single shot field sensitivity of $\sigma_{B_{\mathrm{mw}}} \approx 23$ pT. Taking the experimental cycle time of 11 s into account, we obtain a microwave field sensitivity of 77 pT/$\sqrt{\mathrm{Hz}}$. We emphasize that this sensitivity is achieved with a small probe of 20 $\mu\mathrm{m}^3$ in volume. Assuming projection noise scaling and constant density, this corresponds to a volume-normalized sensitivity of 3.5×10^{-10} T$\sqrt{\mu\mathrm{m}^3/\mathrm{Hz}}$, close to that of state-of-the-art DC magnetometers (see section 4.5.3).

An advantage of our technique is that it readily gives an absolute calibration of the measured microwave magnetic field, since the properties of the atomic transition are well known (see section 2.3.3 and reference [52]). The interferometer can be extended to measure magnetic fields at other frequencies. For example, sensitivity to DC fields can be created by moving away from the magic field. Most high-precision measurements discussed in section 4.5.3 are sensitive to fields oscillating at kHz or MHz frequencies; sensitivity to RF fields can be obtained in our interferometer by off-resonantly coupling a two-photon transition with the aid of a known microwave field.

6.9 Data analysis

In this section, I describe the data analysis procedure used for the main results of this chapter, sections 6.6 and 6.7.

The raw data we obtain from the experiment is a set of two absorption images and one reference image for each run of the experiment. To these, we apply the fringe removal algorithm and we count the atom numbers N_1 and N_2 in elliptical regions as described in section 5.9.3.

6.9.1 Density-dependent level shift

We achieve small shot-to-shot fluctuations in total atom number N of typically $\sigma_N \approx 40$, close to the Poissonian noise of $\sigma_N = \sqrt{N}$ expected for a single-particle stochastic process such as evaporative cooling[7]. Nevertheless, our interferometer is sensitive to a density-dependent level shift arising from mean-field interactions. Since our detection noise on N is much smaller than the spread in atom numbers, we can correct for this shift in each shot individually [106].

We measure the density-dependent level shift based on the coherent-state reference data in figure 6.12. For each data point in the figure, consisting of 240 runs of the experiment, we determine the slope dn/dN through least-squares fitting. The fitted slopes are shown in figure 6.15. For an N-dependent level

technical noise.

[7] Note that sub-Poissonian atom number statistics in a BEC have been created with evaporative cooling [141], thanks to the mean-field interaction.

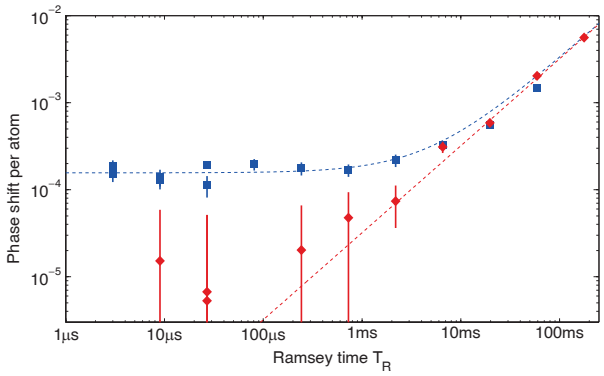

Figure 6.15: Measurement of the density-dependent level shift. The fitted phase shift per atom dn/dN is shown for the same data as in figure 6.12, for the coherent-state reference data (red diamonds) and the squeezed-state interferometer data (blue squares), respectively. Dashed lines show the fitted level shift from the reference data (red line) and predicted shift for the squeezed-state data (blue line).

shift, we expect a linear increase of dn/dN with T_R, plus a constant offset for the squeezed-state interferometer acquired during the splitting time T_S. From a linear fit to the red data points, we find a level shift of (5.1 ± 0.1) mHz/atom. We then correct all data sets for this level shift using the measured total N in each shot.

We emphasize that we use only the reference data to measure this correction factor. For the squeezed-state data we assume the density-dependent shift during T_S to be identical to that measured during T_R. This assumption is in good agreement with measuring dn/dN separately on the squeezed-state data sets, as visible from the blue data in figure 6.15. Finally, if we would not apply the correction at all, the scanning probe interferometer would still perform below the SQL at $\langle \xi^2 \rangle = -1.7$ dB, and our interferometer would remain sub-SQL for 10 ms.

6.10 Noise analysis

In this section, I present a brief analysis of the measured noise levels, and discuss possible causes that limit the observed squeezing and lifetime.

6.10.1 Squeezed input state

The squeezed state presented in section 6.4 shows the best squeezing at turning angles around $\theta = 12° - 14°$. This is consistent with a simulated squeezed state, obtained by evolution of the Hamiltonian $H_{\text{int}} = \chi S_z^2$ for a time T_S such that $\chi T_S = 0.003$ with $N = 1400$. The simulated "ideal" squeezing for this state is $\zeta^2_{\text{sim}} = -12.9$ dB at $\theta = 12.8°$. In the anti-squeezed direction $\zeta^2_{\text{sim}} = +12.9$ dB, indicating the simulated state is still very close to a minimum uncertainty state.

Both the optimal turning angle θ and the anti-squeezed noise are in good agreement with the experimental data in figure 6.8, and thus we assume that the integrated $\int_0^{T_S} \chi \, dt \approx 0.003$ in our experimental sequence.

The best squeezing observed in the experiment is thus limited by other processes. Squeezing may be limited by both fundamental processes, such as collisional losses, and by technical noise sources such as phase and power fluctuations during the Rabi pulses and phase noise during T_S.

Losses

The effect of losses during the creation of spin-squeezing with the one-axis twisting Hamiltonian is studied in references [62, 110, 111]. For multiple loss processes symmetric for both states, the spin squeezing parameter is affected as [110]

$$\xi^2 = \xi_0^2 + \frac{\gamma}{3}, \tag{6.1}$$

where ξ_0 is the squeezing parameter without losses and $\gamma = (1 - N(T_S)/N(0))$ is the fraction of atoms lost during the squeezing. The result assumes a constant loss rate (independent of N), which is valid for $\gamma \ll 1$. Using the loss model of section 4.1.2, we estimate the lost fraction is $\gamma \approx 0.08$ in our experiment after $T_S = 23.4$ ms, and $\gamma/3 \approx -16$ dB. The predicted squeezing in the presence of losses is $\xi^2 = -11$ dB. Therefore, we assume losses have a negligible effect on the preparation of squeezed states in our experiment[8].

Reference [110] also gives an estimate for the best possible squeezing and optimal squeezing time for a given loss rate and value of χ. During T_S we have $\langle\chi\rangle \approx 0.13$ s^{-1} in the experiment, and the initial loss rate is 3.6 s^{-1}. With these numbers, an optimal squeezing of $\xi^2 = -12$ dB at $T_S = 36$ ms is predicted, if no other noise sources would be present.

Phase noise during splitting and recombination

Phase noise σ_φ during T_S deteriorates the squeezing by adding a noise term $\zeta^2_{\text{phase noise}} = \sigma_\varphi \sin\theta$, where θ is the turning angle after squeezing. During free evolution of either a squeezed or coherent state, we observe phase noise consistent with shot-to-shot frequency fluctuations of 150 mHz rms, as shown in figure 6.12. For $T_S = 23.4$ ms and $\theta = 12°$, this corresponds to $\zeta^2_{\text{phase noise}} = -15$ dB, and thus this level of phase noise would not significantly affect our observed squeezing. If the observed squeezing level would be limited by phase noise during T_S, additional shot-to-shot frequency fluctuations of about 450 mHz rms would have to

[8] The theory does not take asymmetric losses (which cause a population difference of $\langle n\rangle \approx 0.05$ after T_S) into account, which may lead to different behavior. However, in reference [62] a numerical simulation with losses in only one state was performed, showing no significant differences in ξ^2 up to the optimal squeezing time.

be present. In this section, I discuss possible sources of extra phase noise during T_S.

In past experiments [12], phase noise was a significant limitation to the observed squeezing. The largest contribution to phase noise was caused by power fluctuations in the on-chip microwave signal, which convert to frequency fluctuations via the microwave level shift V_{mw}. To alleviate these problems, power stabilization of the on-chip microwave signal was implemented prior to the experiments described in this thesis. In addition, we use a lower V_{mw}, which apart from realizing better wave function overlap at the revival time also reduces the effect of power fluctuations. In figure 6.5, a level shift of $V_{\mathrm{mw}} = 415 \pm 2$ Hz is found. From independent measurements, we estimate the relative power stability of the microwave signal to be $\lesssim 10^{-4}$. Thus, we expect the additional frequency fluctuations during T_S to be less than 42 mHz, not significantly deteriorating the squeezing.

Another significant source of phase noise in the previous experiment was a fluctuating trap position due to fluctuating wire currents and bias fields. Due to the strong microwave field gradient, a change in trap position also causes differential level shifts. Since the present experiments operate at lower V_{mw}, the sensitivity to trap position has also been strongly reduced. Furthermore, we now use a second independent current source for B_y during the final stage of the experiment, strongly improving the noise characteristics. With the simulation described in section 5.3, we estimate a differential level shift of 150 mHz/mG in B_y and 120 mHz/mG in B_z. We measure slow drifts of $\lesssim 0.5$ mG in the magnetic fields, and the corresponding level shifts are expected to be at the $\lesssim 100$ mHz level.

We estimate the sensitivity of V_{mw} to changes in the wire current I_L to be 6 mHz/μA, whereas the shot-to-shot fluctuations in the corresponding current source are ≈ 10 μA. Changes in I_D cause level shifts of at most 3 mHz/μA, and the long-term stability of the respective current sources is $\lesssim 2$ μA.

In summary, there is no indication that phase noise during T_S limits the observed squeezing, but the biggest source of phase noise originates from drifts in B_y and B_z. Note that in the main experiments of this chapter, we are only sensitive to drifts of $\lesssim 1$ hour time scale, since we take all shots for a single measurement of ξ^2 consecutively. In ongoing and future measurements of more complicated states, measurement runs spanning several days might be required, and larger drifts may be present on those time scales.

Power and phase fluctuations in Rabi pulses

To estimate the effect of power and phase noise in the pulses, we simulate different types of noise during the experimental sequence. We calculate the effect of the Rabi pulses on the mean spin and calculated the added variance in S_z over an ensemble with noisy parameters included. For pulse noise, we differentiate be-

tween two time scales relevant to our experiment: fast fluctuations which occur within a single Rabi pulse, and shot-to-shot fluctuations on the time scale of the experimental cycle time. On both time scales, fluctuations in power and phase are included in the simulation.

The measurement of figure 6.8 shows increased noise at $\theta = 190°$. This type of noise is well described by fast phase fluctuations. For example, phase fluctuations of $2.5 \times 10^{-4}\text{rad}/\sqrt{\text{Hz}}$ give rise to an *added* noise of $\zeta^2 = -3.8$ dB at $\theta = 192°$. This noise level is consistent with separate characterization measurements, where we use a coherent state and turn for $\theta = 6\pi$. Fast phase noise has negligible effect on the squeezing at $\theta = 12°$. We attribute these fast phase fluctuations to the SRS SG384 signal generator used for the microwave part of the Rabi pulses. After these measurements, we replaced the unit with first a refurbished HP 8340B and later a Rohde & Schwarz SGS100A signal generator. Both devices offer similar phase noise characteristics, considerably better than the SRS unit.

After replacing the microwave generator, we consistently observe squeezing levels around $\zeta^2 = -4.8 \pm 0.5$ dB at $\theta - 12°$ and are able to perform extra Rabi rotations without strongly degrading the squeezing level. Our best squeezing could be limited by shot-to-shot power fluctuations of 1% or by fast power fluctuations with a relative amplitude of $2.5 \times 10^{-4}/\sqrt{\text{Hz}}$. Characterization measurements with long Rabi pulses (6π or more) indicate a shot-to-shot power stability better than 10^{-3}, which is confirmed by direct measurements of the microwave and RF power and insufficient to explain the observed squeezing. However, fast power fluctuations might play a role, and their simulated effect is consistent with our characterization measurements.

Recently, we have implemented several measures to improve the power stability of the Rabi pulses. For the microwave signal, we have set up an active power stabilization loop, which is described in detail in section 5.8. For the radio frequency signal we have mounted the power amplifier and RF switch on a temperature stabilized block. These improvements are most significant for very long-term power drifts which are not limiting the experiments described in this chapter, but the microwave power stabilization circuit should also be beneficial for the short-term power stability. Further investigation of the pulse stability is needed in the future to enable more complex sequences.

6.10.2 Phase noise in Ramsey measurements

In this section, I revisit the frequency noise observed in the squeezed-state lifetime measurement of figure 6.12 (section 6.6). Figure 6.16 shows the same data expressed as phase noise $\sigma_\varphi = \sigma_n/C$. Here, we assume the phase noise is small enough that a linear approximation to the sinusoidal interference fringe is justified, and the shot-to-shot fluctuations do not "wrap around" to the next interference fringe. This assumption is well satisfied for all but the last data point at $T_R = 531$ ms where $\sigma_n/C = (35 \pm 4)°$ and the actual phase noise might be

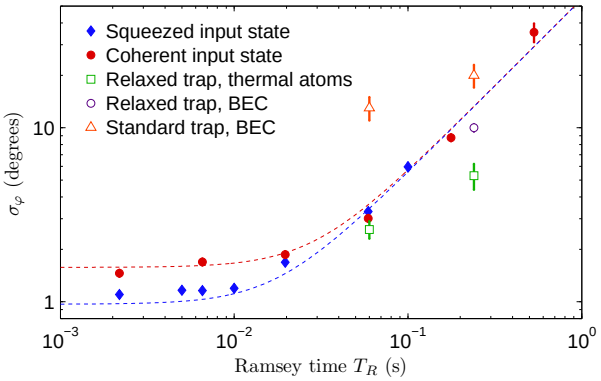

Figure 6.16: Measurement of interferometric phase noise for varying T_R. Closed symbols and dashed lines correspond to the data in figure 6.12. Open symbols correspond to a separate measurement with thermal atoms (green squares) and a BEC (purple circles) in a relaxed trapping potential, as well as a BEC in the standard trap (orange triangles). The open-symbol measurements are described in section 6.10.2.

somewhat higher.

The data is well described by a model that includes the quantum projection noise plus shot-to-shot frequency fluctuations between the reference clock and the atoms, where the two contributions are added in variance. Shot-to-shot frequency fluctuations lead to phase noise that scales as $\sigma_\varphi = \sigma_{\omega_{\text{clock}}} T_R$, and we use $\sigma_{\omega_{\text{clock}}} = 2\pi \times 150$ mHz to model the data. In the following, several potential contributions to these frequency fluctuations are discussed.

Reference clock

Compared to the atomic resonance frequency of 6.8 GHz, $\sigma_{\omega_{\text{clock}}}$ corresponds to a relative frequency stability of 2×10^{-11} on a time scale from 100 ms to the experimental cycle time of $T_{\text{cyle}} = 11$ s. Comparison to figure 5.10 suggests that frequency fluctuations of our reference clock are well below this level[9].

Magnetic field noise

We operate close to the "magic field" of $B = 3.23$ G, where the differential Zeeman shift between $|1\rangle$ and $|2\rangle$ vanishes up to second order, such that influences of magnetic field noise on the atomic phase are minimized. In the measurement of figure 6.12, the magnetic field was 34 mG away from the magic field, and the sensitivity of the atomic level shift to magnetic field was 0.5 Hz/G.

Since the trap is aligned almost exactly with x, the magnetic field sensitivity is dominated by fluctuations in B_x. In the current source responsible for the

[9] Both the Agilent E8257D, used in this measurement, and the Quartzlock E8000-BVA, used in later measurements have at worst the Allan deviation shown by the red line in figure 5.10.

bias field in x-direction, we measure slow drifts corresponding to $\sigma_{B_x} \approx 500$ µG, which causes level shifts of 250 µHz. Short-term fluctuations are much smaller, typically ≈ 3 µG rms.

Noise in the ambient magnetic field in the lab is reduced by the µ-metal shield surrounding the science cell. With a flux-gate sensor, we measure drifts of ≈ 15 µG over several days and short-term noise $\lesssim 5$ µG inside the µ-metal shielding.

In conclusion, magnetic field noise in our experiment has a negligible effect on the phase noise.

One-axis twisting Hamiltonian

As discussed in section 4.4, the one-axis twisting Hamiltonian causes phase noise if there is a significant residual $\chi > 0$ in the non-split trap. The phase noise observed in the measurement of figure 6.12 would be produced by an average $\langle\chi\rangle = 0.025\ s^{-1}$ for a coherent input state. Comparing to calculations in reference [60], this would require a significantly reduced density overlap.However, during the coherent-state measurement, the contrast is $C > 98\%$ for all measurements up to $T_R = 59$ ms, indicating that significant demixing does not take place.

Another clear indication that phase diffusion due to H_{int} does not dominate, is that it would have a much stronger effect for the squeezed-state interferometer, since the anti-squeezed quadrature is aligned with S_z and the initial $\mathrm{var}(S_{z,0})$ is about 12 dB larger than that of a coherent state. In the experiment, we observe equal phase noise for a coherent and squeezed input state.

Finite temperature

As discussed in section 4.4, finite temperature affects the phase coherence of a BEC. In the experiment we use very cold BECs. Figure 6.17 shows absorption images averaged over 3120 runs of the experiment, together with one-dimensional integrated line profiles. No clear sign of a thermal cloud is visible. The fringes visible in part c) and f) of figure 6.17 originate from residual fringes in the probe illumination (see section 5.9).

From the calculation of figure 4.8, even a temperature of $T/T_c = 0.08$ would suffice to explain the observed phase noise, which corresponds to a non-condensed atom number of only $N_{\mathrm{th}} \approx 0.7$ (see equation (2.2)). A thermal fraction this small would indeed not be detectable in figure 6.17, and finite-temperature effects might well have a significant effect on the phase noise. Note, however, that this calculation considers a single-component BEC. Our experiment is sensitive to the *relative* phase noise between the two components of our BEC, and finite-temperature effects might have significantly different effects on the relative phase.

Phase spreading due to finite temperature in a BEC is density dependent, as mentioned already in section 4.4. To see if density-dependent effects limit the

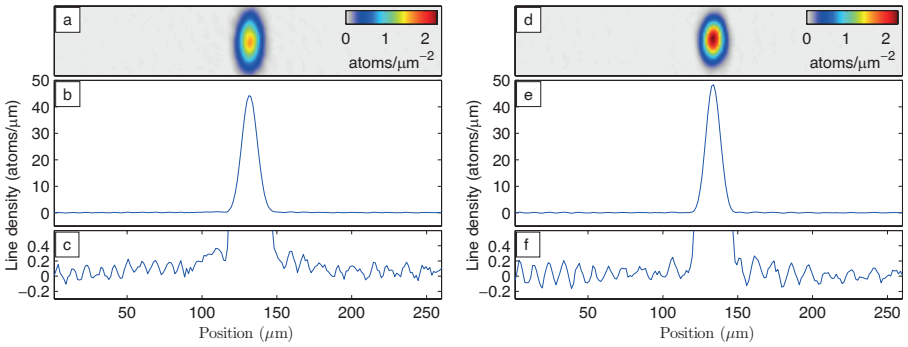

Figure 6.17: Absorption images averaged over 3120 runs of the experiment. Shown are a) average absorption image in $F = 1$; b) and c) line density integrated along z for $F = 1$. d)-f) show the same measurements as a)-c), respectively, but for $F = 2$.

phase noise in our experiment, we performed several Ramsey measurements in a relaxed trap with trap frequencies of $(\omega_l, \omega_\perp) \approx 2\pi \times (130, 260)$ Hz. The phase noise measured in these measurements is shown as open symbols in figure 6.16. This data was taken with a different configuration for the microwave and RF equipment as the main experiment (closed symbols in figure 6.16), and only comparison between the open symbols is meaningful. A BEC in the relaxed trap (purple circle) has significantly lower phase noise than a BEC in the standard experiment trap (orange triangles), indicating that the phase noise is indeed density dependent. A thermal ensemble of 1.6×10^4 atoms in the relaxed trap exhibits even lower phase noise.

In conclusion, finite temperature or other density-dependent effects may well limit the phase coherence in our experiment, and a thorough study of the fundamental limits of phase coherence in a BEC is needed. These effects could be studied with our experiment [115].

7

Conclusions and outlook

7.1 Conclusions

In this thesis, I have experimentally demonstrated a scanning-probe atom interferometer operating below the standard quantum limit, and used it for the measurement of a microwave near-field. This is the first demonstration of entanglement-enhanced atom interferometry with a high spatial resolution scanning probe, and promises further high-resolution sensing and measurement applications such as the investigation of surface effects and the search for fundamental short-range interactions [2]. Quantum metrology is useful in measurements with high spatial resolution, since the atom number in the probe volume is limited by collisional loss.

Our interferometer is realized with $N = 1400$ ^{87}Rb atoms, trapped in a cloud of $1.1 \times 1.1 \times 4.0$ µm radius, corresponding to a spatial resolution of 20 µm^3. We create spin-squeezed states with an interferometrically useful reduction of projection noise by $\xi^2 = -4.3 \pm 0.4$ dB in variance compared to the SQL. We realize a scanning-probe interferometer by transporting the entangled atoms from 40 down to 16 µm from the chip surface, and use it to measure a microwave near-field distribution. The scanning probe interferometer operates at $\xi^2 = -2.2$ dB below the SQL in this measurement. High-resolution microwave field imaging is relevant to fundamental research as well as the design of micro-fabricated microwave circuits which are increasingly important in modern mobile communication technology. Our demonstration measurement operates at higher resolution and better microwave field sensitivity of 2.4 µT compared to existing techniques (see section 4.5.2).

In a measurement at a fixed position, we demonstrate a squeezed-state interferometer operating $\xi^2 \approx -4$ dB below the SQL. The interferometer remains sub-SQL for interrogation times up to $T_R = 10$ ms, significantly longer than previously demonstrated in atom interferometers (see section 3.8). The best sensitivity of our interferometer corresponds to a microwave field sensitivity of 77 pT/$\sqrt{\text{Hz}}$. Taking our small probe size into account, the volume-normalized sensitivity is 3.5×10^{-10} T$\sqrt{\mu\text{m}^3/\text{Hz}}$, on par with state-of-the-art sensors for

static and low-frequency magnetic fields (see section 4.5.3). This demonstrates that atom-chip-based BEC systems are excellent for quantum metrology applications, providing competitive sensitivity at micrometer resolution.

We show that density-dependent losses place a tight limit on the useful number of atoms in a high-spatial-resolution atom interferometer, highlighting the usefulness of quantum metrology in this situation. For our experimental parameters, we predict optimal sensitivity for $N = 750$ and $T_R = 3.5$ s when taking only losses into account, and an optimal interrogation time of $T_R \approx 3$ s when using $N = 1400$ initial atoms. In the experiment, we do not reach this optimum, and T_R is limited to much lower values. The interferometric lifetime of both the squeezed state and a coherent state is limited to ≈ 10 ms due to phase spreading. Initial estimates show that the phase spreading may well be due to fundamental dephasing of a BEC, even at very low temperatures. These finite-temperature effects are also density dependent, indicating that the useful N and T_R in an interferometer are limited even more strictly than predicted by our calculation of atom losses. Further research into the fundamental limits of atom interferometry with high spatial resolution is desirable, both in experimental studies and theoretical predictions that apply to the experimental situation.

In summary, the experiments presented in this thesis demonstrate quantum metrology with high spatial resolution and atom interferometry with state-of-the-art sensitivity, and are a starting point for fundamental studies of decoherence in BECs. In addition, our experimental setup is a promising platform for further studies of entanglement in many-particle systems, as will be discussed in the following section.

7.2 Outlook

In this section, I discuss several measurements that could be implemented with our experimental setup in the near and intermediate future. I briefly present a few initial results of current experimental progress, which is carried out by my colleagues at the time of this writing.

7.2.1 Phase coherence in a BEC

A better understanding of the intrinsic limits to the phase coherence in a BEC is of fundamental interest and particularly relevant for quantum metrology with BECs. Fundamental limits to the temporal coherence of a three-dimensional BEC have not been observed experimentally, and theoretical studies make different predictions depending on how the system is initially prepared [115].

In reference [115], a scheme is proposed to directly measure the phase spreading with a two-component BEC. In the proposal, the phase spreading of e.g. component $|1\rangle$ is measured, using a small population in $|2\rangle$ as a (non-interacting) phase reference. The small population in $|2\rangle$ would be created with a short Rabi

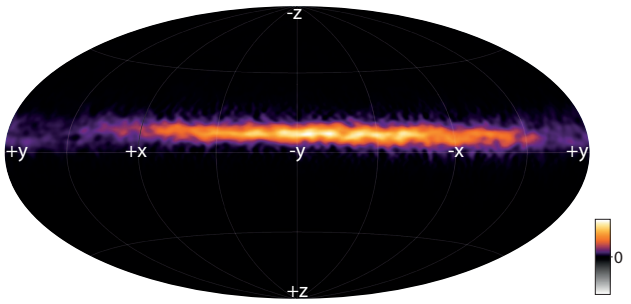

Figure 7.1: Reconstructed spherical Wigner function of an over-squeezed state with $N \approx 450$ atoms. The Bloch sphere is shown in a Hammer projection, with the Cartesian axes indicated by white labels.

pulse, and the components would be split with a state-selective potential to allow independent evolution. Our experimental setup provides all ingredients needed for this type of measurements. The phase decoherence can be measured by monitoring the interferometric contrast, as proposed in reference [115], or alternatively the evolution of phase noise can be measured directly[1]. The temperature dependence of the phase spreading can be investigated by modifying the evaporative cooling sequence to prepare a higher temperature condensate. Such measurements can provide valuable insight in the limits of metrology with BECs, and in addition can give a better understanding of the decoherence observed in our experiment.

7.2.2 Over-squeezed states and quantum Fisher information

In this thesis, we studied mildly squeezed states, which are directly usable in a traditional Ramsey interferometer and are well characterized by the squeezing parameter ξ^2. However, as discussed in section 3.5.2, highly entangled states for which $\xi^2 > 1$ but which are still useful for quantum metrology can be created with the one-axis twisting Hamiltonian H_{int}. For example, increasing χT_S compared to the squeezed-state preparation creates over-squeezed states, which significantly wrap around the Bloch sphere and therefore have reduced interferometric contrast. Experimentally demonstrating that such states are useful for quantum metrology and studying the related entanglement is a challenging goal.

We have made initial measurements of over-squeezed states in our system. We use a similar sequence as for preparing squeezed states in section 6.4. However, instead of a dynamic splitting and recombination scheme, we use a more adiabatic scheme where the state-selective potential is slowly turned on and off. Figure 7.1

[1] For a direct phase measurement, the best sensitivity is obtained with a $\pi/2$-pulse as final pulse, rather than the short pulse in the original proposal. This is very similar to the case of interferometry in the presence of losses presented in section 3.1, and to some extent analogous to homodyne detection in optics.

shows a tomographic reconstruction of the Wigner function of a state created with $N \approx 450$ atoms and a splitting time of $T_S = 100$ ms. Projective measurements were made along 360 different directions of the collective spin[2]. The density matrix was reconstructed from the data with an iterative numerical maximum likelihood optimization ($R\rho R$-iteration) [142]. The resulting Wigner function is shown on the Bloch sphere in a Hammer projection, which maps the entire surface of the sphere to a plane.

Currently, we use tomographic reconstruction algorithms to get a visual description of the state through the spherical Wigner function. However, experimental noise significantly affects the reconstructed state, and attempts to calculate the quantum Fisher information F_Q from the reconstructed states yield results that depend strongly on the details of the reconstruction method. Alternative to determining F_Q directly, measures of statistical distinguishability such as the Hellinger distance can be related to F_Q and may be more easily measured in an experiment [84, 143]. Further research into practical measures of interferometric usefulness and entanglement of strongly squeezed states is needed.

7.2.3 Schrödinger kitten states

Schrödinger cat states are maximally entangled states that are optimal for quantum metrology, and can in principle be created with the one-axis twisting Hamiltonian (see section 3.5.2). A characteristic feature of strong entanglement in an N-atom cat state is a band of N fringes in the Wigner function. However, a cat state is extremely difficult to create, since even changing N by one changes this fringe pattern, requiring both perfect atom number stability and no losses.

It is intriguing to ask if other highly entangled states could be created with less stringent experimental requirements. One candidate is a so-called Schrödinger kitten state, described in section 3.5.2. Using a mean population of only a few atoms in state $|2\rangle$, which is most prone to losses, the total effect of losses is reduced. The losses in $|1\rangle$ can be reduced by using a smaller total atom number. Furthermore, the kitten state has only a few fringes on the Wigner function, and might therefore also be more robust against losses in $|1\rangle$.

In ongoing work, we are investigating the possibility to create Schrödinger kitten states experimentally. Figure 7.2 shows the reconstructed Wigner function of a recent experimentally created state with $N = 150$ atoms. The state was created with a Rabi $\pi/20$-pulse to create a small population in $|2\rangle$, followed by an adiabatic splitting and recombination scheme taking in total $T_S = 170$ ms and a splitting distance of 3 μm. The splitting time was chosen such that the expected $\int_0^{T_S} \chi dt \approx \pi/2$ based on simulated dynamics in a 2D simulation of the two-component GP equations (2.4). For comparison, an ideal kitten state with

[2]The spin projection of $(\hat{S}_z \cos\theta + \hat{S}_y \sin\theta)\sin\phi + \hat{S}_x \cos\phi$ was measured for θ spanning $(0, 2\pi)$ in steps of 2° and $\phi = 0, 35^\circ$. These angles form two rings of axes: a large ring through the poles of the Bloch sphere, and smaller ring rotated by 35° towards x.

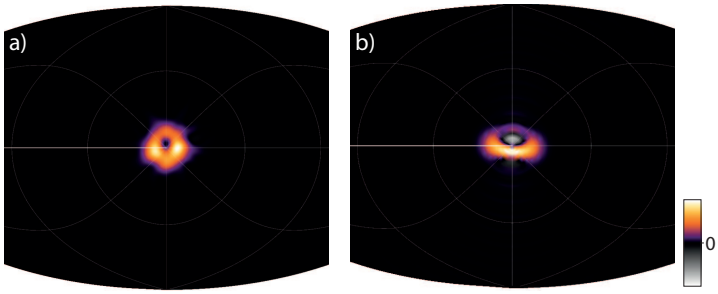

Figure 7.2: Schrödinger kitten states. a) Reconstructed spherical Wigner function of a state with $N \approx 150$ atoms and $\int_0^{T_S} \chi dt \approx \pi/2$. b) Simulated Wigner function of a Schrödinger kitten state with the same parameters. In both panels, part of a Hammer projection is shown, where the $-z$ axis of the Bloch sphere is at the center.

the same parameters is shown.

While the Wigner function of the experimentally measured state shows some structure, it does not show negative regions, nor does it clearly reproduce the shape of the kitten state. For further progress, a better understanding of the role of atom number fluctuations and atom losses for kitten states is needed. Experimentally, further improving the atom number stability will be important for the generation of kitten states. This may be achieved by improving the imaging setup, and in particular optimizing it for small atom numbers, in combination with strict post-selection of the data on total atom number. Detection of small ensembles with a sensitivity close to the single-atom level is feasible with absorption imaging [138, 144], and single-atom sensitivity has been demonstrated with fluorescence imaging [145].

7.2.4 Entanglement between two BECs

In this thesis, we used the one-axis twisting Hamiltonian generated by collisional interactions to create correlations between the spin-states of atoms within the BEC. Alternatively, one could use two initially independent BECs, each with two internal spin states. Collisional interactions between the BECs could be used to create entanglement between the BECs. This type of entanglement generation was one of the initial motivations for the design of our atom chip [57], and an experimental scheme was proposed to create a phase gate for quantum information processing with single atoms [57, 146].

Recently, a very similar experimental scheme to entangle 2 BECs was proposed in reference [147]. The scheme is shown in figure 7.3 and works as follows. Two independent BECs a and b are created in the two wells of a double-well potential, and both are prepared in an equal superposition of components $|1\rangle$ and $|2\rangle$. We denote $|i\rangle_k$ the component $|i\rangle$ of BEC k. Then, an internal-state-dependent potential shifts the components $|2\rangle_a$ and $|2\rangle_b$, but leaves $|1\rangle_a$ and $|1\rangle_b$ in place. This way, $|1\rangle_a$ overlaps with $|2\rangle_b$. During this phase, collisional in-

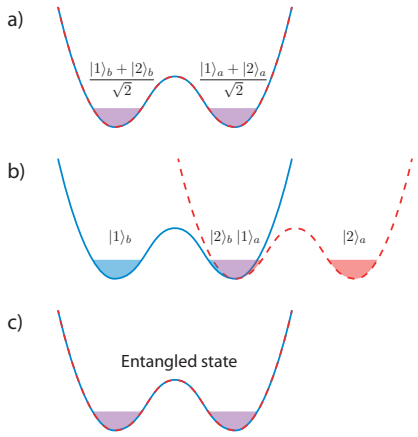

Figure 7.3: Schematic of the experimental scheme proposed in [147]. a) A coherent spin state is prepared in each well. b) The potential for state $|2\rangle$ is shifted spatially such that $|1\rangle_a$ and $|2\rangle_b$ overlap. c) The traps are overlapped again at their initial position. Figure based on [147].

teractions create entanglement between the two BECs. Finally, the BECs are overlapped again, and the spin projection of each BEC is measured.

We denote $\hat{S}^a$ and $\hat{S}^b$ the collective spin operators of BEC a and b, respectively. During the interaction phase, the Hamiltonian has nonlinear terms

$$H = \chi(\hat{S}_z^a)^2 + \chi(\hat{S}_z^b)^2 - \chi_{ab}\hat{S}_z^a\hat{S}_z^b, \tag{7.1}$$

where for simplicity all scattering lengths and mode functions of the BECs have been chosen equal [147]. The first two terms are the one-axis twisting Hamiltonian for each individual BEC, and the third term creates entanglement between the two BECs. Similar to the Schrödinger cat states that are generated by the one-axis twisting Hamiltonian, the Hamiltonian (7.1) generates highly entangled states at special revival times depending on the ratio between χ and χ_{ab}. At short evolution times, which are more accessible experimentally, it generates Einstein-Podolski-Rosen-type entanglement between properly chosen directions of the collective spins $\hat{S}^a$ and $\hat{S}^b$.

The exact scheme depicted in figure 7.3 is not straightforward to realize on our current atom chip[3], but a slightly different alternative scheme proposed in [57] can be implemented. In the alternative scheme, state $|1\rangle$ is left in a double-well potential, whereas state $|2\rangle$ is state-selectively modified from double-well to single-well. As a result, $|2\rangle_a$ and $|2\rangle_b$ collide and interact. This generates the same interaction as equation (7.1), with $\chi_{ab} = \chi/2$ for equal scattering lengths and fully overlapping mode functions [147]. In appendix B an example of suitable

[3] On our atom chip, wires for static magnetic potentials are close to the CPWs used for state-dependent potentials, making it difficult to state-dependently translate a double-well potential along x.

current configurations is given, and the expected technical phase noise between the two wells is analyzed.

Apart from creating double-well potentials in the experiment, a few additional ingredients are needed to create and measure entanglement between two BECs. First, internal-state Rabi rotations in both wells independently are desirable, such that different combinations of spin quadratures can be measured. The gradients in Rabi frequency observed in section 6.1 may be used to our benefit by creating a different Rabi frequency in each well. This effect can be enhanced by using on-chip microwaves for Rabi pulses, which have very strong but reproducible gradients. A tailored pulse sequence could be used to get the desired end result in each well. For read-out, state-selective imaging of both wells independently is straight-forward to implement, since the trap separation is well resolved by our imaging system. Finally, simulations and experimental work are needed to determine whether the components $|2\rangle_a$ and $|2\rangle_b$ can be cleanly separated and re-captured after colliding. Alternatively, a next-generation atom chip can be designed to directly implement the scheme of figure 7.3.

Appendix A

Atom chip layout

Figure A.1 shows the wire pattern of the base chip. The base chip has a "double H"-structure, accentuated in a darker color. The other wire structures are lead wires to the science chip. The contacts (marked as gray circles) are labeled according to the system used in the experiment. The ground contacts G1-G4 of the microwave connectors are coupled to the corresponding DC wire with surface-mount capacitors, forming the on-chip bias-Ts. For example, G1 is capacitively coupled to M2 and M5.

Figure A.2 shows the layout of the science chip. The lower gold layer is shown orange (labels starting with D and U). The wires of the upper gold layer are shown in bright yellow (labels starting with M, and MW1-MW4 for the central microwave conductors).

In the main experiment trap (see section 5.4) the current $I_L = 130$ mA runs from U3 to U10. There are three dimple currents of $I_D = 2$ mA each running from M16→M6, MW3→MW2 and M17←M9, respectively. The effective dimple current is thus 2 mA in $-y$-direction.

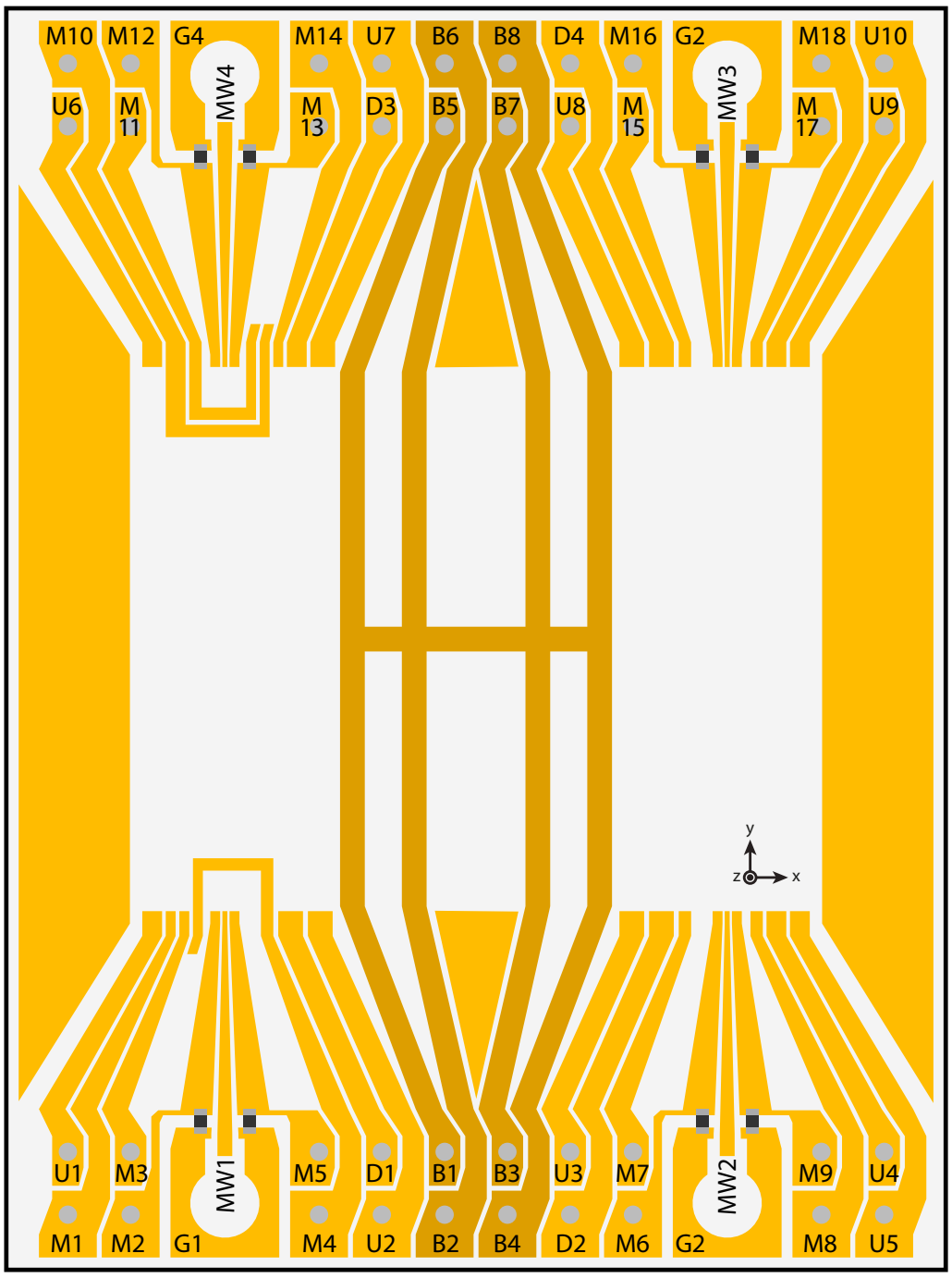

Figure A.1: Base chip layout

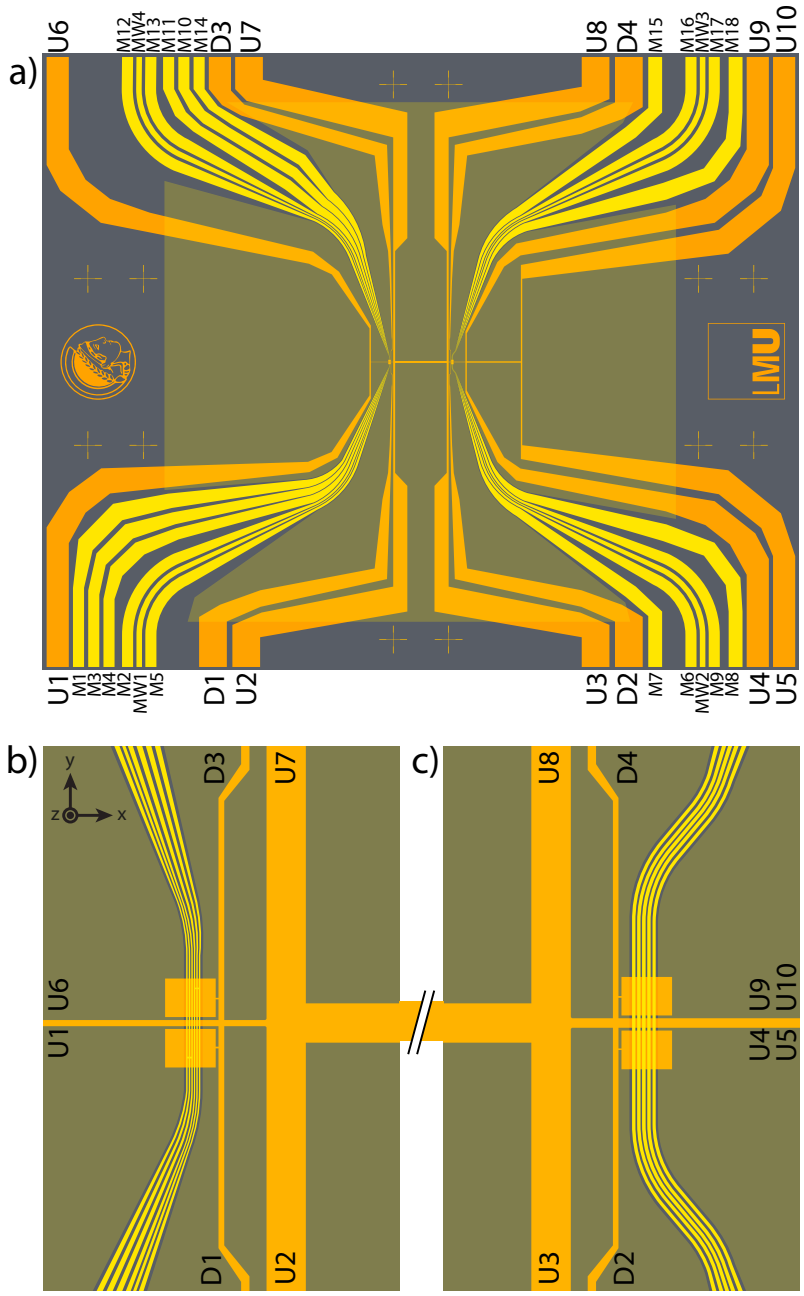

Figure A.2: Science chip layout, showing a) complete science chip, b) 6-wire structure, c) 5-wire structure.

Appendix B

State-selective double-well potential

In this appendix, I present a possible current configuration to generate both state-dependent and state-independent double-well potentials on our atom chip.

Figure B.1 shows the proposed current configuration, using the five-wire structure of the atom chip. The trap is based on a dimple trap. Transverse confinement is given by a wire along x carrying $I_L = 70$ mA and a static field $B_y = 4.0$ G. Longitudinal confinement and static double-well splitting are provided by all five dimple wires in the y-direction. The central wire (core of the CPW) carries a variable current I_{D1}, the two surrounding wires (ground wires of the CPW) carry $I_{D2} = -2$ mA each and the two outer wires (auxiliary DC wires) carry $(I_{D3} = -4 \text{ mA}) \pm I_c$ each, where I_c is a small compensation current, which can be used to tune the energy difference between the left and right well of a double-well potential. A variable microwave current I_{mw} is used in the CPW.

We consider three different configurations listed in table B.1. Configuration a) is a single-well potential for both states, realized with I_{D1} in the $-y$ direction. Configuration b) is a state-independent double well, realized with I_{D1} along $+y$.

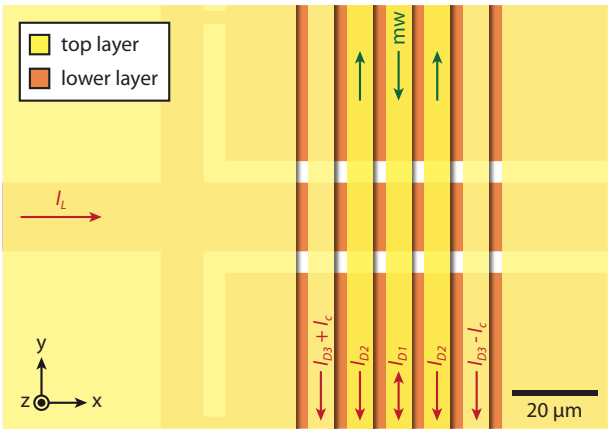

Figure B.1: Current configuration for double-well traps. The central wire current I_{D1} can be chosen in either direction depending on the desired trap (see text).

	a)	b)	c) $\|1\rangle$	c) $\|2\rangle$	
I_{D1}	-1.10	+1.40	+1.06		mA
I_c	0	-4.1	15.7		µA
I_{mw}	0	0	82.5		mA
z_0	23.6	24.2	24.4	23.7	µm
B_0	2.73	2.92	2.90	2.90	G
$\omega_l/(2\pi)$	167	171	169	169	Hz
$\omega_{\perp 1}/(2\pi)$	667	629	627	644	Hz
$\omega_{\perp 2}/(2\pi)$	751	683	695	676	Hz
d	–	17.6	17.9	–	µm
$\Delta V/h$	–	33.9	-14.3	–	Hz
Barrier	–	2.6	2.6	–	Hz

Table B.1: Current configurations and simulated trap geometry, for a) single well, b) double well and c) state-dependent double well potentials. For the state-dependent potential, states $|1\rangle$ and $|2\rangle$ are listed separately. The bottom section lists the splitting distance d, the energy difference ΔV and the energy barrier between the two wells in the case of double-well potentials. The trap frequencies in the left and right wells are equal within 4 Hz.

Both configuration a) and b) use no microwave potentials. Configuration c) is a state-dependent double well: it is a double well for state $|1\rangle$, but a single well for state $|2\rangle$. It is realized by a combination of I_{D1} along $+y$ and the state-dependent microwave potential.

Figure B.2 shows potential traces along x for the three trap configurations. The traces are taken along the trap minimum in the y- and z-directions. All traps have very similar trap frequencies, listed in table B.1. All traps are approximately $z_0 \approx 24$ µm away from the surface. The magnetic field B_0 in the trap center ranges from 2.7 G to 2.9 G.

For both double-well configurations, the differential energy ΔV between the left and right well have been set close to 0 by tuning I_c. Using $I_c = 0$ yields similar trap configurations, but with $\Delta V = -h \times 156$ Hz in configuration b) and $\Delta V = h \times 718$ Hz for state $|1\rangle$ in configuration c). This differential energy arises from the asymmetric lead wires in configuration b), and in addition from the asymmetry in the microwave potential in configuration c). Note that the lead wires are only approximately implemented in the trap simulation, and the actual energy difference may be different in the experiment. The energy barrier between the two wells is $h \times 2.6$ kHz. For comparison, a small BEC with 500 atoms in a single well has a chemical potential of $\mu \approx h \times 1.2$ kHz.

The trap can be smoothly changed between all three configurations by linearly ramping the static currents and the microwave power $P_{\mathrm{mw}} \propto I_{\mathrm{mw}}^2$ from the initial to the final value[1]. For example, a smooth ramp from from configuration a) to b)

[1] If a constant ΔV is desired during the ramp, a nonlinear ramp for I_c may be needed.

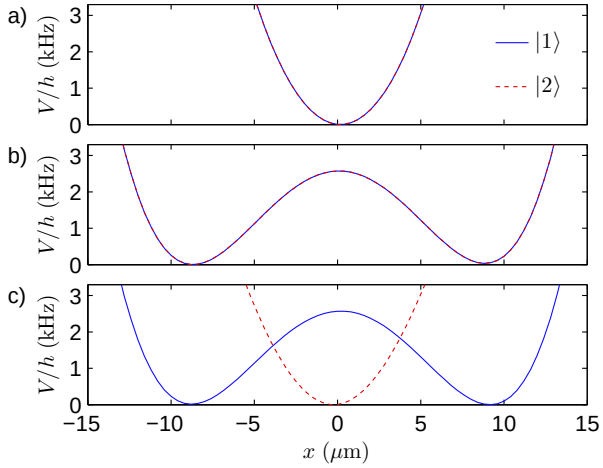

Figure B.2: Trapping potentials as function of x. Panels a)-c) correspond to the configurations a)-c), respectively. For each x, the potential is minimized along y and z.

Parameter	Sensitivity	Stability	$\sigma_{\Delta V}$
I_c	47 Hz/μA	–	–
I_{D3}	0.3 Hz/μA	$\lesssim$ 2 μA	$\lesssim$ 0.6 Hz
I_{D2}	0.1 Hz/μA	$\lesssim$ 2 μA	$\lesssim$ 0.2 Hz
I_{D1}	0.2 Hz/μA	$\lesssim$ 2 μA	$\lesssim$ 0.4 Hz
I_L	11 Hz/mA	$\approx$ 10 μA	$\approx$ 0.1 Hz
B_x	0.1 Hz/mG	$\lesssim$ 0.5 mG	$\lesssim$ 0.05 Hz
B_y	0.1 Hz/mG	$\lesssim$ 0.5 mG	$\lesssim$ 0.05 Hz
B_z	5.5 Hz/mG	$\lesssim$ 0.5 mG	$\lesssim$ 2.3 Hz
I_{mw}	19 Hz/mA	$\lesssim$ 4 μA	$\lesssim$ 0.07 Hz

Table B.2: Sensitivity of the differential double well energy in configuration c) to various parameters. Stability estimates for our current experimental equipment are listed, as well as the resulting estimates of the differential energy fluctuations $\sigma_{\Delta V}$.

can be used to coherently split a single BEC. An abrupt change from configuration b) to c) can be used to create correlations between the atoms in the left and the right well: while state $|1\rangle$ would stay split, the two clouds in state $|2\rangle$ would make one oscillation in opposing directions, and interact in the process. The atoms could be re-captured in configuration b) at the end of one oscillation.

For coherence in a double well potential, stability of the energy difference ΔV is crucial. Table B.2 lists the sensitivity of $\Delta V/h$ to changes in the wire currents and magnetic fields, calculated for the state-selective double well. Stability estimates for the current sources used in the present experiment are also listed. These are estimates for long-term drifts, short-term stability is usually much better. For all currents except I_c, using the current sources of our current

experiment would suffice to obtain a a stability on the order of 1 Hz. Here it is assumed that both wires carrying I_{D3} are connected in series to the same current source, and similar for I_{D2}, such that differential current noise is not present. Special attention should be paid to the current supplying B_z. However, no field in z-direction is needed in the proposed trap configuration, and the current source could be completely disconnected during a double-well experiment, or replaced by a much lower output current source if a small offset field is desired.

The compensation current I_c is designed to adjust ΔV, and ΔV is naturally very sensitive to fluctuations of I_c. To implement I_c, a very low-current source could be designed which superimposes a current of $2 \times I_c$ onto one of the outer wires that carry I_{D3}. It would have to supply only about 40 µA, but with $\approx$ 10 nA stability. While the required relative stability is less stringent than what is realized in our larger current sources, it may be difficult to achieve at such small currents, and it might not be feasible to couple it to the same wire as I_{D3}. Another way to obtain tunability of ΔV would be to use a chip wire along y that is far away from the trapping region. Then, a larger current can be supplied with an existing current source, generating only a small field gradient at the trap position. Finally, I_c could be omitted completely, if a nonzero ΔV is not problematic for a given experiment.

Bibliography

[1] L. de Broglie, *Recherches sur la théorie des quanta*, Annales de Physique **10^{e} série**, t. III (1925).

[2] A. D. Cronin, J. Schmiedmayer, and D. E. Pritchard, *Optics and interferometry with atoms and molecules*, Rev. Mod. Phys. **81**, 1051 (2009).

[3] J. Kitching, S. Knappe, and E. A. Donley, *Atomic sensors - a review*, IEEE Sensors Journal **11**, 1749 (2011).

[4] R. Wynands and S. Weyers, *Atomic fountain clocks*, Metrologia **42**, S64 (2005).

[5] W. M. Itano, J. C. Bergquist, J. J. Bollinger, J. M. Gilligan, D. J. Heinzen, F. L. Moore, M. G. Raizen, and D. J. Wineland, *Quantum projection noise: Population fluctuations in two-level systems*, Phys. Rev. A **47**, 3554 (1993).

[6] V. Giovannetti, S. Lloyd, and L. Maccone, *Advances in quantum metrology*, Nature Photon. **5**, 222 (2011).

[7] P. Hyllus, L. Pezzé, and A. Smerzi, *Entanglement and sensitivity in precision measurements with states of a fluctuating number of particles*, Phys. Rev. Lett. **105**, 120501 (2010).

[8] J. Estève, C. Gross, A. Weller, S. Giovanazzi, and M. K. Oberthaler, *Squeezing and entanglement in a Bose-Einstein condensate*, Nature **455**, 1216 (2008).

[9] J. Appel, P. J. Windpassinger, D. Oblak, U. B. Hoff, N. Kjaergaard, and E. S. Polzik, *Mesoscopic atomic entanglement for precision measurements beyond the standard quantum limit*, Proc. Natl. Acad. Sci. U.S.A. **106**, 10960 (2009).

[10] M. H. Schleier-Smith, I. D. Leroux, and V. Vuletić, *States of an ensemble of two-level atoms with reduced quantum uncertainty*, Phys. Rev. Lett. **104**, 073604 (2010).

[11] I. D. Leroux, M. H. Schleier-Smith, and V. Vuletić, *Implementation of cavity squeezing of a collective atomic spin*, Phys. Rev. Lett. **104**, 073602 (2010).

[12] M. F. Riedel, P. Böhi, Y. Li, T. W. Hänsch, A. Sinatra, and P. Treutlein, *Atom-chip-based generation of entanglement for quantum metrology*, Nature **464**, 1170 (2010).

[13] R. Bücker, J. Grond, S. Manz, T. Berrada, T. Betz, C. Koller, U. Hohenester, T. Schumm, A. Perrin, and J. Schmiedmayer, *Twin-atom beams*, Nature Physics **7**, 608 (2011).

[14] B. Lücke, M. Scherer, J. Kruse, L. Pezze, F. Deuretzbacher, P. Hyllus, O. Topic, J. Peise, W. Ertmer, J. Arlt, L. Santos, A. Smerzi, and C. Klempt, *Twin matter waves for interferometry beyond the classical limit*, Science **334**, 773 (2011).

[15] C. Gross, H. Strobel, E. Nicklas, T. Zibold, N. Bar-Gill, G. Kurizki, and M. K. Oberthaler, *Atomic homodyne detection of continuous-variable entangled twin-atom states*, Nature **480**, 219 (2011).

[16] E. M. Bookjans, C. D. Hamley, and M. S. Chapman, *Strong quantum spin correlations observed in atomic spin mixing*, Phys. Rev. Lett. **107**, 210406 (2011).

[17] C. D. Hamley, C. S. Gerving, T. M. Hoang, E. M. Bookjans, and M. S. Chapman, *Spin-nematic squeezed vacuum in a quantum gas*, Nature Phys. **8**, 305 (2012).

[18] J. G. Bohnet, K. C. Cox, M. A. Norcia, J. M. Weiner, Z. Chen, and J. K. Thompson, *Reduced back-action for phase sensitivity 10 times beyond the standard quantum limit*, arXiv:1310.3177 (2013).

[19] N. Behbood, F. M. Ciurana, G. Colangelo, M. Napolitano, G. Toth, R. J. Sewell, and M. W. Mitchell, *Generation of macroscopic singlet states in a cold atomic ensemble*, arXiv:1403.1964v2 (2014).

[20] C. Gross, T. Zibold, E. Nicklas, J. Estève, and M. K. Oberthaler, *Nonlinear atom interferometer surpasses classical precision limit*, Nature **464**, 1165 (2010).

[21] A. Louchet-Chauvet, J. Appel, J. J. Renema, D. Oblak, N. Kjaergaard, and E. S. Polzik, *Entanglement-assisted atomic clock beyond the projection noise limit*, New J. Phys. **12**, 065032 (2010).

[22] I. Leroux, M. Schleier-Smith, and V. Vuletić, *Orientation-dependent entanglement lifetime in a squeezed atomic clock*, Phys. Rev. Lett. **104**, 250801 (2010).

[23] W. Wasilewski, K. Jensen, H. Krauter, J. J. Renema, M. V. Balabas, and E. S. Polzik, *Quantum noise limited and entanglement-assisted magnetometry*, Phys. Rev. Lett. **104**, 133601 (2010).

[24] R. J. Sewell, M. Koschorreck, M. Napolitano, B. Dubost, N. Behbood, and M. W. Mitchell, *Magnetic sensitivity beyond the projection noise limit by spin squeezing*, Phys. Rev. Lett. **109**, 253605 (2012).

[25] R. Folman, P. Krüger, J. Schmiedmayer, J. Denschlag, and C. Henkel, *Microscopic atom optics: From wires to an atom chip*, Advances in Atomic Molecular and Optical Physics **48**, 263 (2002).

[26] J. Fortágh and C. Zimmermann, *Magnetic microtraps for ultracold atoms*, Rev. Mod. Phys. **79**, 235 (2007).

[27] J. Reichel and V. Vuletić (editors), *Atom chips*, (Wiley-VCH, Weinheim, Germany) (2011).

[28] Y. Lin, I. Teper, C. Chin, and V. Vuletić, *Impact of the Casimir-Polder potential and Johnson noise on Bose-Einstein condensate stability near surfaces*, Phys. Rev. Lett. **92**, 050404 (2004).

[29] S. Wildermuth, S. Hofferberth, I. Lesanovsky, S. Groth, P. Krüger, J. Schmiedmayer, and I. Bar-Joseph, *Sensing electric and magnetic fields with Bose-Einstein condensates*, Appl. Phys. Lett. **88**, 264103 (2006).

[30] J. M. Obrecht, R. J. Wild, and E. A. Cornell, *Measuring electric fields from surface contaminants with neutral atoms*, Phys. Rev. A **75**, 062903 (2007).

[31] S. Aigner, L. Pietra, Y. Japha, O. Entin-Wohlman, T. David, R. Salem, R. Folman, and J. Schmiedmayer, *Long-range order in electronic transport through disordered metal films*, Science **319**, 1226 (2008).

[32] D. Hunger, S. Camerer, T. W. Hänsch, D. König, J. P. Kotthaus, J. Reichel, and P. Treutlein, *Resonant coupling of a Bose-Einstein condensate to a micromechanical oscillator*, Phys. Rev. Lett. **104**, 143002 (2010).

[33] M. Gierling, P. Schneeweiss, G. Visanescu, P. Federsel, M. Häffner, D. P. Kern, T. E. Judd, A. Günther, and J. Fortagh, *Cold-atom scanning probe microscopy*, Nature Nanotechn. **6**, 446 (2011).

[34] P. Treutlein, P. Hommelhoff, T. Steinmetz, T. W. Hänsch, and J. Reichel, *Coherence in microchip traps*, Phys. Rev. Lett. **92**, 203005 (2004).

[35] T. Schumm, S. Hofferberth, L. M. Andersson, S. Wildermuth, S. Groth, I. Bar-Joseph, J. Schmiedmayer, and P. Krüger, *Matter-wave interferometry in a double well on an atom chip*, Nature Phys. **1**, 57 (2005).

[36] P. Böhi, M. F. Riedel, J. Hoffrogge, J. Reichel, T. W. Hänsch, and P. Treutlein, *Coherent manipulation of Bose-Einstein condensates with state-dependent microwave potentials on an atom chip*, Nature Phys. **5**, 592 (2009).

[37] C. F. Ockeloen, R. Schmied, M. F. Riedel, and P. Treutlein, *Quantum metrology with a scanning probe atom interferometer*, Phys. Rev. Lett. **111**, 143001 (2013).

[38] L. Essen and J. V. L. Parry, *The caesium resonator as a standard of frequency and time*, Royal Society of London Philosophical Transactions Series A **250**, 45 (1957).

[39] H. J. Metcalf and P. van der Straten, *Laser Cooling And Trapping*, (Springer-Verlag Berlin Heidelberg New York), 1st edition (1999).

[40] H. J. Metcalf and P. van der Straten, *Laser cooling and trapping of atoms*, Journal of the Optical Society of America B Optical Physics **20**, 887 (2003).

[41] W. Ketterle and N. J. V. Druten, *Evaporative cooling of trapped atoms*, Advances in Atomic Molecular and Optical Physics **37**, 181 (1996).

[42] M. H. Anderson, J. R. Ensher, M. R. Matthews, C. E. Wieman, and E. A. Cornell, *Observation of Bose-Einstein condensation in a dilute atomic vapor*, Science **269**, 198 (1995).

[43] C. C. Bradley, C. A. Sackett, J. J. Tollett, and R. G. Hulet, *Evidence of Bose-Einstein condensation in an atomic gas with attractive interactions*, Phys. Rev. Lett. **75**, 1687 (1995).

[44] K. B. Davis, M.-O. Mewes, M. R. Andrews, N. J. van Druten, D. S. Durfee, D. M. Kurn, and W. Ketterle, *Bose-Einstein condensation in a gas of sodium atoms*, Phys. Rev. Lett. **75**, 3969 (1995).

[45] A. Einstein, *Quantentheorie des einatomigen idealen Gases. Zweite Abhandlung*, Sitzung der physikalisch-mathematischen Klasse vom 8. Januar 1925 (1925).

[46] W. Ketterle and N. J. van Druten, *Bose-Einstein condensation of a finite number of particles trapped in one or three dimensions*, Phys. Rev. A **54**, 656 (1996).

[47] F. Dalfovo, S. Giorgini, L. P. Pitaevskii, and S. Stringari, *Theory of Bose-Einstein condensation in trapped gases*, Rev. Mod. Phys. **71**, 463 (1999).

[48] A. J. Leggett, *Bose-Einstein condensation in the alkali gases: Some fundamental concepts*, Rev. Mod. Phys. **73**, 307 (2001).

[49] A. M. Mateo and V. Delgado, *Ground-state properties of trapped Bose-Einstein condensates: Extension of the Thomas-Fermi approximation*, Phys. Rev. A **75**, 063610 (2007).

[50] A. S. Sørensen, *Bogoliubov theory of entanglement in a Bose-Einstein condensate*, Phys. Rev. A **65**, 043610 (2002).

[51] P. Treutlein, *Coherent manipulation of ultracold atoms on an atom chip*, Ph.D. thesis, Ludwigs-Maximilians-Universität, München (2008).

[52] D. A. Steck, *Rubidium 87 D line data*, available online at `http://steck.us/alkalidata` (revision 2.1.4, 23 December 2010).

[53] G. Breit and I. I. Rabi, *Measurement of nuclear spin*, Physical Review **38**, 2082 (1931).

[54] D. M. Harber, H. J. Lewandowski, J. M. McGuirk, and E. A. Cornell, *Effect of cold collisions on spin coherence and resonance shifts in a magnetically trapped ultracold gas*, Phys. Rev. A **66**, 053616 (2002).

[55] C. Deutsch, F. Ramirez-Martinez, C. Lacroûte, F. Reinhard, T. Schneider, J. Fuchs, F. Piéchon, F. Laloë, J. Reichel, and P. Rosenbusch, *Spin self-rephasing and very long coherence times in a trapped atomic ensemble*, Phys. Rev. Lett. **105**, 020401 (2010).

[56] R. J. C. Spreeuw, C. Gerz, L. S. Goldner, W. D. Phillips, S. L. Rolston, C. I. Westbrook, M. W. Reynolds, and I. F. Silvera, *Demonstration of neutral atom trapping with microwaves*, Phys. Rev. Lett. **72**, 3162 (1994).

[57] P. Treutlein, T. W. Hänsch, J. Reichel, A. Negretti, M. A. Cirone, and T. Calarco, *Microwave potentials and optimal control for robust quantum gates on an atom chip*, Phys. Rev. A **74**, 022312 (2006).

[58] R. Anderson, *Nonequilibrium dynamics and relative phase evolution of two-component Bose-Einstein condensates*, Ph.D. thesis, Swinburne University, Melbourne (2010).

[59] K. Moler, D. S. Weiss, M. Kasevich, and S. Chu, *Theoretical analysis of velocity-selective Raman transitions*, Phys. Rev. A **45**, 342 (1992).

[60] M. F. Riedel, *Multi-particle entanglement on an atom chip*, Ph.D. thesis, Ludwig-Maximilians-Universität, München (2010).

[61] S. Raghavan, H. Pu, P. Meystre, and N. P. Bigelow, *Generation of arbitrary Dicke states in spinor Bose-Einstein condensates*, Optics Communications **188**, 149 (2001).

[62] Y. Li, P. Treutlein, J. Reichel, and A. Sinatra, *Spin squeezing in a bimodal condensate: spatial dynamics and particle losses*, European Physical Journal B **68**, 365 (2009).

[63] K. M. Mertes, J. W. Merrill, R. Carretero-González, D. J. Frantzeskakis, P. G. Kevrekidis, and D. S. Hall, *Nonequilibrium dynamics and superfluid ring excitations in binary Bose-Einstein condensates*, Phys. Rev. Lett. **99**, 190402 (2007).

[64] M. Egorov, B. Opanchuk, P. Drummond, B. V. Hall, P. Hannaford, and A. I. Sidorov, *Measurement of s-wave scattering lengths in a two-component Bose-Einstein condensate*, Phys. Rev. A **87**, 053614 (2013).

[65] J. P. Dowling, G. S. Agarwal, and W. P. Schleich, *Wigner distribution of a general angular-momentum state: Applications to a collection of two-level atoms*, Phys. Rev. A **49**, 4101 (1994).

[66] R. Schmied and P. Treutlein, *Tomographic reconstruction of the Wigner function on the Bloch sphere*, New J. Phys. **13**, 065019 (2011).

[67] L. Pezzé and A. Smerzi, *Entanglement, nonlinear dynamics, and the Heisenberg limit*, Phys. Rev. Lett. **102**, 100401 (2009).

[68] I. Lesanovsky, T. Schumm, S. Hofferberth, L. M. Andersson, P. Krüger, and J. Schmiedmayer, *Adiabatic radio-frequency potentials for the coherent manipulation of matter waves*, Phys. Rev. A **73**, 033619 (2006).

[69] J. J. P. van Es, S. Whitlock, T. Fernholz, A. H. van Amerongen, and N. J. van Druten, *Longitudinal character of atom-chip-based rf-dressed potentials*, Phys. Rev. A **77**, 063623 (2008).

[70] A. Shevchenko, M. Heiliö, T. Lindvall, A. Jaakkola, I. Tittonen, M. Kaivola, and T. Pfau, *Trapping atoms on a transparent permanent-magnet atom chip*, Phys. Rev. A **73**, 051401 (2006).

[71] R. Gerritsma, S. Whitlock, T. Fernholz, H. Schlatter, J. A. Luigjes, J.-U. Thiele, J. B. Goedkoop, and R. J. C. Spreeuw, *Lattice of microtraps for ultracold atoms based on patterned magnetic films*, Phys. Rev. A **76**, 033408 (2007).

[72] V. Leung, A. Tauschinsky, N. Druten, and R. Spreeuw, *Microtrap arrays on magnetic film atom chips for quantum information science*, Quantum Information Processing **10**, 955 (2011).

[73] X. Liu, K.-H. Brenner, M. Wilzbach, M. Schwarz, T. Fernholz, and J. Schmiedmayer, *Fabrication of alignment structures for a fiber resonator by use of deep-ultraviolet lithography*, Applied Optics **44**, 6857 (2005).

[74] T. P. Purdy and D. M. Stamper-Kurn, *Integrating cavity quantum electrodynamics and ultracold-atom chips with on-chip dielectric mirrors and temperature stabilization*, Appl. Phys. B **90**, 401 (2008).

[75] Y. Colombe, T. Steinmetz, G. Dubois, F. Linke, D. Hunger, and J. Reichel, *Strong atom-field coupling for Bose-Einstein condensates in an optical cavity on a chip*, Nature **450**, 272 (2007).

[76] J. Reichel, W. Hänsel, P. Hommelhoff, and T. W. Hänsch, *Applications of integrated magnetic microtraps*, Applied Physics B: Lasers and Optics **72**, 81 (2001).

[77] J. Reichel, *Microchip traps and Bose-Einstein condensation*, Applied Physics B: Lasers and Optics **74**, 469 (2002).

[78] T. Kwaaitaal, B. J. Luymes, and G. A. van der Pijll, *Noise limitations of Michelson laser interferometers*, Journal of Physics D Applied Physics **13**, 1005 (1980).

[79] M. Napolitano, M. Koschorreck, B. Dubost, N. Behbood, R. J. Sewell, and M. W. Mitchell, *Interaction-based quantum metrology showing scaling beyond the Heisenberg limit*, Nature **471**, 486 (2011).

[80] M. Zwierz, C. A. Pérez-Delgado, and P. Kok, *General optimality of the Heisenberg limit for quantum metrology*, Phys. Rev. Lett. **105**, 180402 (2010).

[81] V. Giovannetti, S. Lloyd, and L. Maccone, *Quantum metrology*, Phys. Rev. Lett. **96**, 010401 (2006).

[82] B. Yurke, S. L. McCall, and J. R. Klauder, *SU(2) and SU(1,1) interferometers*, Phys. Rev. A **33**, 4033 (1986).

[83] P. Hyllus, O. Gühne, and A. Smerzi, *Not all pure entangled states are useful for sub-shot-noise interferometry*, Phys. Rev. A **82**, 012337 (2010).

[84] A. Smerzi, *Quantum interferometry*, Lecture at *Advances in quantum technology: From quantum information to quantum devices*, Federal University of Rio Grande do Norte, Brazil, available online at `http://www.iip.ufrn.br/media/pdf/lecture_2.pdf` (August 2012).

[85] M. Kitagawa and M. Ueda, *Squeezed spin states*, Phys. Rev. A **47**, 5138 (1993).

[86] D. J. Wineland, J. J. Bollinger, W. M. Itano, and D. J. Heinzen, *Squeezed atomic states and projection noise in spectroscopy*, Phys. Rev. A **50**, 67 (1994).

[87] A. Sørensen, L.-M. Duan, J. I. Cirac, and P. Zoller, *Many-particle entanglement with Bose-Einstein condensates*, Nature **409**, 63 (2001).

[88] S. Chaudhury, S. Merkel, T. Herr, A. Silberfarb, I. H. Deutsch, and P. S. Jessen, *Quantum control of the hyperfine spin of a Cs atom ensemble*, Phys. Rev. Lett. **99**, 163002 (2007).

[89] Y. Castin and J. Dalibard, *Relative phase of two Bose-Einstein condensates*, Phys. Rev. A **55**, 4330 (1997).

[90] J. Schlienz and G. Mahler, *The maximal entangled three-particle state is unique*, Physics Letters A **224**, 39 (1996).

[91] V. Giovannetti, S. Lloyd, and L. Maccone, *Quantum-enhanced measurements: Beating the standard quantum limit*, Science **306**, 1330 (2004).

[92] S. M. Kay, *Fundamentals of statistical signal processing: estimation theory* (Prentice-Hall, Upper Saddle River, NJ) (1993).

[93] L. Pezzé, A. Smerzi, G. Khoury, J. F. Hodelin, and D. Bouwmeester, *Phase detection at the quantum limit with multiphoton Mach-Zehnder interferometry*, Phys. Rev. Lett. **99**, 223602 (2007).

[94] D. W. Berry and H. M. Wiseman, *Optimal states and almost optimal adaptive measurements for quantum interferometry*, Phys. Rev. Lett. **85**, 5098 (2000).

[95] A. V. Lebedev, P. Treutlein, and G. Blatter, *Sequential quantum-enhanced measurement with an atomic ensemble*, Phys. Rev. A **89**, 012118 (2014).

[96] P. Hyllus, W. Laskowski, R. Krischek, C. Schwemmer, W. Wieczorek, H. Weinfurter, L. Pezzé, and A. Smerzi, *Fisher information and multiparticle entanglement*, Phys. Rev. A **85**, 022321 (2012).

[97] A. S. Sørensen and K. Mølmer, *Entanglement and extreme spin squeezing*, Phys. Rev. Lett. **86**, 4431 (2001).

[98] P. Hyllus, L. Pezzé, A. Smerzi, and G. Tóth, *Entanglement and extreme spin squeezing for a fluctuating number of indistinguishable particles*, Phys. Rev. A **86**, 012337 (2012).

[99] F. Benatti, R. Floreanini, and U. Marzolino, *Sub-shot-noise quantum metrology with entangled identical particles*, Annals of Physics **325**, 924 (2010).

[100] F. Benatti, R. Floreanini, and K. Titimbo, *Entanglement of identical particles*, Open Syst. Inf. Dyn **21**, 1440003 (2014).

[101] N. Killoran, M. Cramer, and M. B. Plenio, *Extracting entanglement from identical particles*, arXiv:1312.4311 (2013).

[102] F. Benatti and D. Braun, *Sub-shot-noise sensitivities without entanglement*, Phys. Rev. A **87**, 012340 (2013).

[103] C. M. Caves, *Quantum-mechanical radiation-pressure fluctuations in an interferometer*, Phys. Rev. Lett. **45**, 75 (1980).

[104] C. M. Caves, *Quantum-mechanical noise in an interferometer*, Phys. Rev. D **23**, 1693 (1981).

[105] The LIGO Scientific Collaboration, *A gravitational wave observatory operating beyond the quantum shot-noise limit*, Nature Phys. **7**, 962 (2011).

[106] P. Rosenbusch, *Magnetically trapped atoms for compact atomic clocks*, Appl. Phys. B **95**, 227 (2009).

[107] S. Whitlock, C. F. Ockeloen, and R. J. C. Spreeuw, *Sub-Poissonian atom-number fluctuations by three-body loss in mesoscopic ensembles*, Phys. Rev. Lett. **104**, 120402 (2010).

[108] E. A. Burt, R. W. Ghrist, C. J. Myatt, M. J. Holland, E. A. Cornell, and C. E. Wieman, *Coherence, correlations, and collisions: What one learns about Bose-Einstein condensates from their decay*, Phys. Rev. Lett. **79**, 337 (1997).

[109] J. Söding, D. Guéry-Odelin, P. Desbiolles, F. Chevy, H. Inamori, and J. Dalibard, *Three-body decay of a rubidium Bose-Einstein condensate*, Appl. Phys. B **69**, 257 (1999).

[110] Y. Li, Y. Castin, and A. Sinatra, *Optimum spin squeezing in Bose-Einstein condensates with particle losses*, Phys. Rev. Lett. **100**, 210401 (2008).

[111] Y. Li, *Spin squeezing in Bose-Einstein condensates*, Ph.D. thesis, Ecole Normale Supérieure de Paris (2010).

[112] M. Egorov, R. Anderson, V. Ivannikov, B. Opanchuk, P. Drummond, B. Hall, and A. Sidorov, *Long-lived periodic revivals of coherence in an interacting Bose-Einstein condensate*, Phys. Rev. A **84**, 021605 (2011).

[113] M. Gustavsson, E. Haller, M. J. Mark, J. G. Danzl, G. Rojas-Kopeinig, and H.-C. Nägerl, *Control of interaction-induced dephasing of Bloch oscillations*, Phys. Rev. Lett. **100**, 080404 (2008).

[114] M. Lewenstein and L. You, *Quantum phase diffusion of a Bose-Einstein condensate*, Phys. Rev. Lett. **77**, 3489 (1996).

[115] Y. Castin and A. Sinatra, *Spatial and temporal coherence of a Bose-condensed gas*, in *New trends and hot topics in atomic and polariton condensates*, edited by A. Bramati and M. Modugno (Springer-Verlag Berlin Heidelberg, 2013).

[116] A. Sinatra, Y. Castin, and E. Witkowska, *Nondiffusive phase spreading of a Bose-Einstein condensate at finite temperature*, Phys. Rev. A **75**, 033616 (2007).

[117] S. D. Hogan, J. A. Agner, F. Merkt, T. Thiele, S. Filipp, and A. Wallraff, *Driving Rydberg-Rydberg transitions from a coplanar microwave waveguide*, Phys. Rev. Lett. **108**, 063004 (2012).

[118] V. Vlaminck, H. Schultheiss, J. E. Pearson, F. Y. Fradin, S. D. Bader, and A. Hoffmann, *Mapping microwave field distributions via the spin Hall effect*, Appl. Phys. Lett. **101**, 252406 (2012).

[119] S. Sayil, D. Kerns, and S. Kerns, *Comparison of contactless measurement and testing techniques to a new all-silicon optical test and characterization method*, IEEE Trans. Instrum. Meas. **54**, 2082 (2005).

[120] J. A. Sedlacek, A. Schwettmann, H. Kübler, R. Löw, T. Pfau, and J. P. Shaffer, *Microwave electrometry with Rydberg atoms in a vapour cell using bright atomic resonances*, Nature Phys. **8**, 819 (2012).

[121] P. Böhi, M. F. Riedel, T. W. Hänsch, and P. Treutlein, *Imaging of microwave fields using ultracold atoms*, Appl. Phys. Lett. **97**, 051101 (2010).

[122] P. Böhi and P. Treutlein, *Simple microwave field imaging technique using hot atomic vapor cells*, Appl. Phys. Lett. **101**, 181107 (2012).

[123] A. Horsley, G.-X. Du, M. Pellaton, C. Affolderbach, G. Mileti, and P. Treutlein, *Imaging of relaxation times and microwave field strength in a microfabricated vapor cell*, Phys. Rev. A **88**, 063407 (2013).

[124] I. K. Kominis, T. W. Kornack, J. C. Allred, and M. V. Romalis, *A subfemtotesla multichannel atomic magnetometer*, Nature **422**, 596 (2003).

[125] D. Budker and M. Romalis, *Optical magnetometry*, Nature Phys. **3**, 227 (2007).

[126] R. Mhaskar, S. Knappe, and J. Kitching, *A low-power, high-sensitivity micromachined optical magnetometer*, Appl. Phys. Lett. **101**, 241105 (2012).

[127] M. Vengalattore, J. M. Higbie, S. R. Leslie, J. Guzman, L. E. Sadler, and D. M. Stamper-Kurn, *High-resolution magnetometry with a spinor Bose-Einstein condensate*, Phys. Rev. Lett. **98**, 200801 (2007).

[128] P. Maletinsky, S. Hong, M. S. Grinolds, B. Hausmann, M. D. Lukin, R. L. Walsworth, M. Loncar, and A. Yacoby, *A robust scanning diamond sensor for nanoscale imaging with single nitrogen-vacancy centres*, Nature Nanotechn. **7**, 320 (2012).

[129] S. Steinert, F. Dolde, P. Neumann, A. Aird, B. Naydenov, G. Balasubramanian, F. Jelezko, and J. Wrachtrup, *High sensitivity magnetic imaging using an array of spins in diamond*, Rev. Sci. Instrum. **81**, 043705 (2010).

[130] P. A. Böhi, *Coherent manipulation of ultracold atoms with microwave near-fields*, Ph.D. thesis, Ludwig-Maximilians-Universität, München (2010).

[131] J. Reichel, W. Hänsel, and T. W. Hänsch, *Atomic micromanipulation with magnetic surface traps*, Phys. Rev. Lett. **83**, 3398 (1999).

[132] L. Ricci, M. Weidemüller, T. Esslinger, A. Hemmerich, C. Zimmermann, V. Vuletic, W. König, and T. W. Hänsch, *A compact grating-stabilized diode laser system for atomic physics*, Optics Communications **117**, 541 (1995).

[133] T. W. Hänsch, M. D. Levenson, and A. L. Schawlow, *Complete hyperfine structure of a molecular iodine line*, Phys. Rev. Lett. **26**, 946 (1971).

[134] J. Hoffrogge, *Mikrowellen-Nahfelder auf Atomchips*, Master's thesis, Ludwig-Maximilians-Universität, München (2007).

[135] D. Allan, *Statistics of atomic frequency standards*, Proceedings of the IEEE **54**, 221 (1966).

[136] G. Reinaudi, T. Lahaye, Z. Wang, and D. Guéry-Odelin, *Strong saturation absorption imaging of dense clouds of ultracold atoms*, Opt. Lett. **32**, 3143 (2007).

[137] C. F. Ockeloen, *Probing fluctuations in a lattice of mesoscopic atomic ensembles*, Master's thesis, University of Amsterdam (2010).

[138] C. F. Ockeloen, A. F. Tauschinsky, R. J. C. Spreeuw, and S. Whitlock, *Detection of small atom numbers through image processing*, Phys. Rev. A **82**, 061606 (2010).

[139] S. A. Haine, J. Lau, R. P. Anderson, and M. T. Johnsson, *Self-induced spatial dynamics to enhance spin-squeezing via one-axis twisting in a two-component Bose-Einstein condensate*, arXiv:1402.0307 (2014).

[140] O. V. Sinkin, R. Holzlöhner, J. Zweck, and C. R. Menyuk, *Optimization of the split-step Fourier method in modeling optical-fiber communications systems*, Journal of Lightwave Technology **21**, 61 (2003).

[141] C.-S. Chuu, F. Schreck, T. P. Meyrath, J. L. Hanssen, G. N. Price, and M. G. Raizen, *Direct observation of sub-Poissonian number statistics in a degenerate Bose gas*, Phys. Rev. Lett. **95**, 260403 (2005).

[142] Z. Hradil, J. Řeháček, J. Fiurášek, and M. Ježek, *Maximum-likelihood methods in quantum mechanics*, in *Quantum state estimation*, edited by M. Paris and J. Řeháček (Springer-Verlag Berlin Heidelberg, 2004).

[143] M. K. Oberthaler and A. Smerzi, private communication.

[144] W. Muessel, H. Strobel, M. Joos, E. Nicklas, I. Stroescu, J. Tomkovič, D. B. Hume, and M. K. Oberthaler, *Optimized absorption imaging of mesoscopic atomic clouds*, Applied Physics B: Lasers and Optics **113**, 69 (2013).

[145] D. B. Hume, I. Stroescu, M. Joos, W. Muessel, H. Strobel, and M. K. Oberthaler, *Accurate atom counting in mesoscopic ensembles*, Phys. Rev. Lett. **111**, 253001 (2013).

[146] H.-J. Briegel, T. Calarco, D. Jaksch, J. I. Cirac, and P. Zoller, *Quantum computing with neutral atoms*, Journal of Modern Optics **47**, 415 (2000).

[147] H. Kurkjian, K. Pawłowski, A. Sinatra, and P. Treutlein, *Spin squeezing and Einstein-Podolsky-Rosen entanglement of two bimodal condensates in state-dependent potentials*, Phys. Rev. A **88**, 043605 (2013).

Acknowledgments

The results presented in this thesis are the fruits of team work, building upon previous work done by my former and present colleagues. In this section, I would like to express my gratitude towards all the people who contributed to the realization of these experiments.

My supervisor, Prof. Philipp Treutlein, has given valuable guidance and support throughout the project, and initiated the research in the labs of Prof. T. W. Hänsch in Munich. Pascal Böhi and Max Riedel have built the experiment in those labs, and I very much enjoyed working with them in my first year in Basel. Roman Schmied has provided countless insights in theoretical and experimental physics, as well as metaphysics, both to my confusion and enlightenment. During the last year, the experiment has been in the hands of Baptiste Allard, who is an outstanding experimental physicist. I am excited that Matteo Fadel joined the project; I am confident the experiment will be in good hands during the coming years.

The electronic and mechanical workshops have provided valuable help and components for the experiment. I thank the university administration, and in particular Germaine Weaver for providing help with many practical questions. I would like to thank the other group members for creating the good atmosphere in the office: Andrew Horsley, Guan-Xiang Du, Maria Korppi, Andreas Jöckel, Matthew Rakher, Aline Faber, Thomas Lauber, Tobias Kampschulte, and Lucas Beguin.

Finally I want to thank my family and friends for the love and support that I everyday enjoy for granted. I want to especially thank Andrin Tomaschett, Sebastian Schweizer, Petra Meyer and Leon Heinz for warmly welcoming me into this new city, and David Jansen for the many exhausting but rewarding cycling trips around it. My dearest gratitude goes towards Maria Korppi, whose love, support and inspiration is a guidance in my life.